國立臺灣大學電機資訊學院光電工程研究所

博士論文

Graduate Institute of Photonics and Optoelectronics
College of Electrical Engineering and Computer Science
National Taiwan University

Doctoral Dissertation

具奈米結構之氧化鋅光電元件特性分析

Characterizations of ZnO Nanostructure Based Optoelectronic Devices

陳正彬

Cheng-Pin Chen

指導教授：黃建璋 博士

Advisor: JianJang Huang, Ph.D.

中華民國 99 年 1 月

January, 2010

國立臺灣大學光電工程研究所 博士論文 具奈米結構之氧化鋅光電元件特性分析 陳正彬 撰 99.1

國立臺灣大學博士學位論文
口試委員會審定書

具奈米結構之氧化鋅光電元件特性分析
Characterizations of ZnO Nanostructure Based Optoelectronic Devices

本論文係陳正彬君（學號 D94941001）在國立臺灣大學光電工程學研究所完成之博士學位論文，於民國 99 年 1 月 21 日承下列考試委員審查通過及口試及格，特此證明

口試委員：黃建璋（指導教授）

夏瑰周　楊志忠

蔡振瀛　彭隆瀚

李清庭　洪瑞華

所長 黃升諒

誌謝

時光荏苒，匆匆四年半的博士生涯即將進入尾聲，即將面對的將是下一段人生的挑戰。然而，學如逆水行舟，唯有不斷的努力及默默耕耘才能換得最甜美的果實。一路走來，我相當幸運的得到許多人的幫助與陪伴，才能使這部論文完整的呈現。因此要感謝的人很多，我謹以此文誠摯的表達我最衷心的謝意。

首先要感謝我的指導教授黃建璋博士，感謝他給我機會讓我進入實驗室學習，無論是研究上創新想法的激發、對實驗應有的積極態度以及進度的掌控及規劃能力、為人處事的方法以及實驗資源的全力支持，並以其專業的學養和細心的指導，讓我可以心無旁騖的專注在自己的學術研究上並獲益良多。同時，在老師嚴格督促之下，我更有信心及把握能獨自面對往後的未知挑戰。儘管，我無法預知困難有多大，但是在這四年半的學習中，我相信我已具備面對以及處理問題的能力。然而每當看到老師在面對眾多雜務以及忙得天昏地暗時，還能細心的幫我訂正論文以及修改錯誤，心中有許多的感謝，著實也讓老師失去許多陪伴家人的寶貴時間，真的感到相當感動。老師也常常與我們分享自己的人生歷程，無論是在學術研究、工作職場甚至是待人接物上，透過老師寶貴的人生經驗讓我能以更宏觀的眼光去規劃未來的人生道路。我也期許有一天能夠有機會幫忙老師。

其次，我想要感謝口試委員在百忙之餘還能撥冗批閱論文初稿，並在口試過程中給予精闢與寶貴的意見以及指導，並透過討論提出一些新的觀點，讓我的論文架構可以更加完整且充實。楊志忠教授對於奈米結構元件的看法以及英文撰寫上的訂正、彭隆瀚教授對於理論模型的使用時機、綦振瀛教授對於載子傳輸時間以及太陽能電池效率影響因子分析的指導、李清庭教授在論文品質以及材料吸收光譜的指正、洪瑞華教授在論文英文寫作的指導以及細節訂正、夏興國博士對光電產業的宏觀視野以及業界經驗分享，都讓我受益良多，也著實讓我體驗到一流學者的風範以及需具備的學養，相當感謝您們。

在台大的四年半中，認識到許多優秀的師長，新世紀光電的李允立博士在與韓國首爾大學學術交流活動上的照顧及關懷、人生經驗以及想法上的開導跟未來方向的建議，都給我相當大的幫助，也讓我順利的度過一些人生關卡，謝謝您。楊志忠教授總是能以幽默詼諧的話語來軟化尷尬的氣氛，而楊教授也以其深厚的物理觀念來告訴我們實驗的結果應該要有一套理論分析來解釋並合理化，讓我在論文報告的準備上總是能以更戰戰兢兢的態度去面對，並期許自己做的更好。彭隆瀚教授對於研究的堅持以及態度，讓我看到一位堅持自己價值觀的勇者，且彭教授總是以恨鐵不成鋼的心情來告誡我們，我們需要一直持續的努力才是真正的尊重自己。

接著我想要感謝曾經在研究以及生活上幫助過我的學長姐。林政宏學長，如果沒有你的全力支持，我沒有辦法有那麼好的研究成果，也感謝您總是在百忙之餘還抽空協助我進行量測，也希望在往後的日子裡我可以有機會幫忙到你，也祝福你跟學嫂早日結婚，謝謝您。巫漢敏學長，感謝您在我研究遇到挫折甚至是心

情沮喪的時候，找我去喝杯咖啡並藉此開導我，告訴我凡事都應該想開一點，也因為您開朗的人生觀帶給我對事物的另一種看法。陳永彬學長，感謝您在我需要幫忙的時候，總是幫我安排時段協助我量測，也因為有您的協助，讓我在研究上有更多資料可以分析，在此深深的感謝您也祝您事事順心。廖洺漢學長，您具備成功人士所應有的謙卑，總是在我感謝您對我的幫助之後，告訴我“這一切都是你自己努力所得到的成果，我並沒有幫助你，反而從你身上學到很多。”我想，你這一句話將會是我往後的座右銘，感謝您的協助。呂志鋒學長，您對於研究成果的堅持總是讓我在每次與您討論之後收穫良多，也深深覺得自己有很多不足的地方。也由於與您在一些生活方面相當契合，一起衝浪、唱歌、嘴砲等等，總是讓我體驗到博士生活應該要有較為輕鬆的面向，也讓我在每次與您輕鬆完之後，做研究更能專心投入(罪惡感很深)，也希望在不久的將來可以親臨海王子的故鄉與您一起聊天。沈坤慶學長，您總是在我操作實驗儀器發生問題時，適時的給予建議及排解狀況，感謝您的幫忙。最後感謝曾經與我參與韓國行的學長姐(正言、皓武、亮吟、美杏、永亭)，感謝您們的陪伴，讓我學到相當多，感謝您們。

林士弘、游政衛、王菘豐以及陳政營同學，感謝您們在我實驗遇到問題的時候，無私的提供我需要的協助以及建議，讓我可以用更全面的想法去思考解決方法。葉伯淳、吳志凌以及林奇鋒學弟，感謝您們在研究上所提供的建議以及協助，讓我可以更加順利的進行實驗，我相信在不久的將來，你們也一定可以成功的完成博士學位。柯董，同窗四年半，我們一起分享研究心得也互相支持鼓勵，希望你未來的道路可以更加順利。下巴與兩儀，你們將是往後實驗室的重要台柱，也相信在你們的努力之下，實驗室會變得更加茁壯，有任何需要幫助也請讓我知道。

我想要感謝佩璇，你是實驗室第一個女生，也因為學妹的加入讓實驗室有更多女生加入，造福了其他學弟，實在是功德無量也讓實驗室活潑不少。然而有幸在這兩年與你一起做實驗、處理問題以及面對老師，幫學長處理很多事情，相當感謝，我相信你也一定可以在未來的道路上走得相當成功。彥任以及紹舜，以後你們要獨自面對研究上的挑戰，我相信你們一定可以，如果需要我的協助也請你們告訴我。我也要感謝已畢業的學弟子揚、易成、志豪、建安、旻諺、建承、逸銘、育昇、子樸、弘憲、孟倫、振印、原禎、世驊、光中、宏禮以及昆懋，感謝您們的幫助。以及，鈺軒、亮宇、姿君、英原、勝傑、欣穎、思婕以及鈞翔，你們的努力會讓實驗室更加茁壯。

最後我想要感謝默默支持與陪伴我的父母與家人，在我求學的這一段時間，默默的支持我且在我心情低落的時候給予我適時的關懷並讓我能夠順利的度過難關，感謝你們。在這本誌謝的最後，我僅以最深的愛獻給我的老婆；雅莉，從交往到結婚我們已經走過了十個年頭,在這段時間裡我很感謝你對我的包容與體諒，謝謝你!!以及我最愛的兒子；湧銘，因為有你們的陪伴讓我能夠順利的完成我的博士學位，在此獻上我對妳們最深的愛!

陳正彬

2010/2/7

摘要

自從 1970 年代發生能源危機以及現今環保意識的抬頭，可回收再利用的能源越來越受重視，其中以太陽能電池的應用最為廣泛。在太陽能電池方面目前有幾個問題有待被解決其中包含:界面反射率、寬廣化的吸收頻譜、入射光的接收角以及元件內載子復合等等所造成的問題。

過去幾十年內，為了提高矽基(Si)為主太陽能電池的效率，發展出一套利用化學濕蝕刻的方式，在太陽能電池的表面製造出具有週期性的粗糙化結構、倒金字塔結構以及蜂窩狀結構，使得太陽能電池表面材料的折射係數形成漸進式的變化以及造成入射光有效的被元件捕捉，進而降低表面的反射率。然而由於化學濕蝕刻容易受到濕度和溫度的影響，所以很難利用化學濕蝕刻成功的製作出具奈米結構的光電元件。

在太陽能電池轉換效率方面，目前以利用多層接面結構的砷化鎵(GaAs)為主的太陽能電池效率最高，但由於其製作步驟繁複且材料成本昂貴，所以在應用上還是以矽基(Si)為主要的太陽能電池材料。而在太陽能電池的光接收角改善方面，目前技術上是利用太陽光追蹤系統來控制入射光保持在接近垂直入射以達到吸收能圓的最大化,但是太陽光追蹤系統卻需要消耗額外的能源進而導致能源的浪費。至於在元件內的載子復合問題，主要是藉由材料品質的改善以及材料與金屬接面的材料重參雜來增加載子的生命周期。然而，傳輸路徑的過長也會使得載子在傳遞到金屬的過程中被缺陷復合的機率提高。

基於以上的問題，我們提出利用結合寬能隙材料氧化鋅(ZnO)以及矽基(Si)，製作出具有寬廣且平坦吸收頻譜的光電元件，接著再利用最佳化的奈米小球鋪排技術，使光電元件的光響應和接收角都有大幅的提升。

同時，我們還利用鋪排奈米小球的技術以及蝕刻製程，製作出在材料接面上具備奈米結構的 n-GZO/a-Si(i)/p^+-Si 異質結構光偵測器，由於奈米結構可以有效的

降低表面反射率以及表面型態較接近圓柱狀，所以此元件具有較高的光響應以及廣接收角的特性。除此之外，我們還發現在奈米結構的元件中其載子傳輸時間較短，而較短的載子傳輸時間可以降低載子在元件內被復合的機率，進而有機會造成較高的光響應。最後，具備奈米結構的光電元件擁有較高的光響應、寬廣的接收角以及較快的載子傳輸時間，其在太陽能電池的應用上具有相當大的潛力。

關鍵字: 太陽能電池，光伏打效應，奈米小球，奈米結構之二極體，光偵測器，布拉格繞射，接收角以及傳輸時間

Preface

Over the recent decades, the photovoltaic cells have emerged to become an important role on energy generation and have attracted lots attentions by scientists and researchers. The purpose of this dissertation is to provide the concepts related to how to achieve the broad band absorption spectrum by utilizing the combination of semiconductor material with different energy band. However, several semiconductors, Si, GaAs, a-Si and GaN, were used to fabricate the photovoltaics. Easy fabrication process and high material quantity are the main key roles for mass production in the industry. From this viewpoint, we utilized the ZnO material to fabricate photodiodes due to its easy fabrication process by RF magnetic sputtering and simplicity on wet etching process. The technique of nanosphere spraying is used to improve the acceptance angle of photodiodes for more stable photocurrent generation when the incident light is tilted. Nanostructure device possessed the better optical response due to its low reflectivity and shorter transit time due to shorter transit paths.

Chapter 1 introduces the history and the encountered difficulty related to the photovoltaics. The dissertation overview is also listed in this chapter. Chapter 2 investigates the potential applications of n-ZnO/p-Si photodiodes on the broad band absorption spectrum and the advantage of nanosphere on the application of wide acceptance angle for the application of photovoltacics. The mechanism of enhanced

acceptance angle was realized by Bragg diffraction, Littrow configuration. Furthermore, chapter 3 mainly focuses on the characterization and fabrication of nanostructure n-GZO/a-Si(i)/p^+-Si p-i-n heterojunction photodiodes. The discussions of transit time on photodiodes with and without nanopatterns were given in this chapter. Finally, chapter 4 summaries the results in this dissertation and the future works are still listed in the last chapter.

Appendix 1 describes the characteristics of ZnO based light emitting diodes (LEDs) by evaporating the n-GZO on the top of p-GaN heterojunction light emitting diodes (LEDs). By inserting the SiO_2 thin layer for current blocking, we could observe the 394nm near UV emission which is due to the recombination between the interfaces of n-GZO/SiO_2 and SiO_2/p-GaN. Appendix 2 describes the optical characteristics of n-GZO/p-GaN heterojunction photodetector. The obvious UV absorption peak was observed at 370nm.

I would foremost like to thank my advisor, Professor JianJang Huang, for his consummate intellect in academic and philosophical matters. His knowledge, experience, dedication, vision and most importantly passion have stimulated my enthusiasm for pushing the forefront of research. Furthermore, his patience and faith in my abilities have inspired me on countless occasions. Without his guidance and mentorship, this work would not have come to fruition. In addition, I would like to

thank my parents, S-L Chen and S-M Wu Chen for their selfless love and support.

Finally!

Thank to my wife, Sharon Y-L Chen, and my son.

Aylwin C-P Chen

2010/2/7

Abstract

Renewable energy was attracted more attentions due to the energy crisis in 1970 and environmental issue in the world. There are several critical problems on high conversion efficiency solar cell manufacturing, low reflectivity, multiple band absorption, wide acceptance angle and low carrier recombination, et al. For the past decades, photovoltaic scientists developed the high conversion efficiency crystalline Si based solar cells by manufacturing the periodic rough structures, pyramid, inverted pyramid and honeycomb, et al., using wet etching on the solar cell surface. And, the reflectance could be drastic decreased due to the gradual refractive index in the surface textured devices. However, the wet etching process is hard to control due to the humidity and temperature in the clean room. Another, the size of textured structure is hard to control at the nanoscale. Furthermore, multiple junction solar cells could produce the higher conversion efficiency compared to the single junction solar cells due to the broad band absorption spectrum. The highest solar cell conversion efficiency was observed in the GaAs based semiconductor. The cost and difficult process result in the smaller market sharing than Si based solar cells. The acceptance angle of incident light for solar cells is another important issue for absorbing maximum light intensity by daytime. Although solar tracking system could provide the solution for this issue, it will cause the extra energy consumption. Another key issue for high

conversion efficiency is carrier recombination. More carriers which were recombined in the devices will reduce the conversion efficiency. However, shortening the carrier transit paths could possibly decrease the probability of recombination when carrier transported to the contact electrodes.

From the above mentions, we proposed another approach to manufacture the high conversion efficiency solar cells by combining the material of GZO and Si. By the overlapping of band gaps, the characteristic of broad band absorption ranged from 400nm to 800nm is realized in the n-GZO/p-Si heterojunction photodiodes. By the simple and novel technique of silica nanosphere spraying, the enhanced responsivity and wide acceptance angle could be achieved in the nanoparticle coated devices. The wide acceptance angle in n-GZO/p-Si photodiodes is due to the Bragg diffraction effect, Litterow configuration. This work could have the potential application to solar cells.

Furthermore, we investigate the nanostructure n-GZO/a-Si(i)/p^+-Si heterojunction photodiodes by using the self-masked nanosphere lithography. The characteristics of high responsivity and wide acceptance angle are achieved in the nanostructure photodiodes which is due to reducing surface reflectivity and nanostructure morphology. Moreover, nanostructure photodiodes have shorter transit time compared to planar photodiodes which is due to the shorter and more transit paths in the nanostructure devices. Nanostructure photodiodes possess the higher photoresponsivity compared to

planar one which is possible due to the lower reflectance and shorter transit time. The n-GZO/a-Si(i)/nanopatterned p^+-Si heterojunction photodiodes has the shortest transit time compared to planar n-GZO/a-Si(i)/p^+-Si and n-GZO/nanopatterned a-Si(i)/p^+-Si heterojunction photodiodes.

Finally, self-masked nanosphere lithography and nanopatterned photodiodes possessed the enhanced photoresponsivity, wider acceptance angle and shorter transit time compared to the planar photodiodes. They have the potential applications to solar cells.

Key words: solar cells, photovoltaics, nanosphere, nanostructure photodiodes, photodetectors, Bragg diffraction, acceptance angle and transit time

Contents

口試委員審定書

誌謝…… I

中文摘要…… III

Preface…….... V

Abstract…….. VIII

Chapter 1 Introduction……... 1

1-1 Historical reviews of solar cells…….. 1

1-1-1 Energy shortage…….. 1

1-1-2 Solar cells progress……. 3

1-1-3 Bottlenecks of solar cells…… 6

A. Broad band absorption…… 7

B. Wide acceptance angle……... 9

C. Low reflectance on solar cells…… 11

D. Carrier recombinations……... 13

1-2 Historical review of ZnO based heterojunction optoelectronic devices…. 14

1-2-1 ZnO based Heterojunction Light Emitting Diodes (LEDs)…… 15

1-2-2 ZnO based Heterojunction Photodetectors (PDs)……... 16

1-2-3 Nanostructure optoelectronic devices progress on solar cell applications……... 17

1-3 Dissertation overviews…… 19

Chapter 2 Nanoparticle coated n-GZO/p-Si hotodiodes with improved photoresponsivities and acceptance angles for potential solar cell applications…….. 21

2-1 Motivations…… 23

2-2 Device fabrications……. 23

2-2-1 Process flows…….. 23

2-2-2 Photos of scanning electronic microscope (SEM)…….. 25

2-2-3 Photos of atomic force microscope (AFM)…… 25

2-2-4 Contact characteristics between Ni/Au and p-Si…… 27

2-3 Characterizations of n-GZO/p-Si photodiodes…… 30

2-3-1 Electrical properties…… 30

2-3-2 Optical properties of n-GZO/p-Si photodiodes…….. 30

A. Photoresponsivity of n-GZO/p-Si photodiodes with flat band absorption…… 30

B. Enhanced photoresponsivity in SiO2 nanoparticle coated photodiodes 34

C. Wide acceptance angle…… 36

D. Theoretical calculations using diffraction theory - Littrow configuration…….. 39

2-4 Conclusions……. 44

Chapter 3 Investigations of light absorption properties and acceptance angles of nanopatterned n-GZO/a-Si(i)/ p^+-Si photodiodes……... 46

3-1 Motivations……. 48

3-2 Device fabrications……. 48

3-2-1 Fabrications of nanopatterned structure……... 48

A. Etching morphology on different nanosphere concentrations…… 48

B. Etching morphology on different etching receipts of nanopatterned structure…….. 51

C. Morphology of nanopatterned p+-Si before and after a-Si(i) deposition 51

D. Morphology of nanopatterned a-Si before and after RIE dry etching… 54

3-2-2 Fabrication process…….. 56

A. Process flows…….. 56

B. SEM photos of nanopatterned p+-Si before and after deposition of a-Si layer……. 58

C. Characterizations of metal contact……. 58

3-3 Characterizations of photodiodes…… 62

3-3-1 Electrical properties……. 62

3-3-2 Optical characterizations of n-GZO/a-Si(i)/p+-Si heterojunction photodiodes…….. 64

A. Photoresponsivity…… 64

B. Reflectance of nanostructure…….. 67

C. Discussions on peak shift of photoresponsivity……. 69

D. Wide acceptance angle……... 72

E. The mechanism of improved acceptance angle…….. 75

3-3-3 Investigations on transit time of nanostructure photodiodes…….. 75

A. Experimental setup……. 75

B. Results and discussions on transit time…….. 77

B-1 Constant incident light intensity……. 77

B-1-1 Comparisons on different devices……... 77

B-1-2 Relations between wavelength and transit time…….. 82

B-2 Constant photocurrents…… 83

B-2-1 Comparisons on different devices…… 83

B-2-2 Relations between wavelength and transit time…….. 85

3-4 Conclusions……. 88

Chapter 4 Conclusions…… 90

Appendix 1 394nm EL emission in n-ZnO/p-GaN LEDs with effective silica current blocking layer…….. 92

A1-1 Motivations……. 93

A1-2 The material analysis of ZnO……. 93

A1-2-1 Preparation of ZnO thin film…… 93

A1-2-2 Photoluminescence (PL) of ZnO……. 94

A1-2-3 X-ray diffraction (XRD) of ZnO……. 96

A1-3 Device fabrication…… 98

A1-4 Characteristics of n-ZnO/p-GaN LEDs…… 99

A1-4-1 Photoluminescence (PL)……... 99

A1-4-2 Electrical characteristics (I-V)…….. 99

A1-4-3 Electroluminescence (EL) of light emitting diodes (LEDs)……. 101

A. The effect of rapid temperature anneal (RTA) process for the n-ZnO/ p-GaN heterojunction LEDs…… 101

B. Electroluminescence (EL) of n-ZnO/p-GaN LEDs with and without SiO_2 current blocking layer…… 104

C. Discussion of band diagram on the mechanism of carrier recombination……. 105

D. Electrical luminescence of device with different thickness of SiO_2 current blocking layer……. 105

A1-5 Conclusions…….. 108

Appendix 2 Photoresponse of heterojunction photo-detectors by RF sputtering n-ZnO on p-GaN/sapphire….. 110

A2-1 Motivations…….. 111

A2-2 Device fabrication…… 111

A2-3 Characteristics of n-ZnO/p-GaN photodetectors……. 112

A. Electrical characteristics (I-V)…….. 112

B. Analysis of X-ray diffraction (XRD)……... 114

C. Photocurrent under different power of incident light…… 114

D. The photoresponsivity of n-ZnO/p-GaN photodiodes…….. 116

E. Discussion on the band diagram of n-ZnO/p-GaN photodiodes…….. 118

A2-4 Conclusions…….. 119

Reference…….... 120

Related Publications and Honor……... 133

List of Figures

Fig. 1-1: International Energy Outlook 2009: World marketed energy consumption is projected to rise by 44 percent from 2006 to 2030.	2
Fig. 1-2: The researched solar cell efficiency progresses from 1975 to 2008.	2
Fig. 1-3: The sketched diagram of PERL (Passivated Emitter Rear Locally) diffused solar cells. (Proposed by Green et al.) [1]	5
Fig. 1-4: The schematic diagram of GaAs based solar cells with the 26.1% conversion efficiency. (Proposed by Bauhuis et al.) [2]	5
Fig. 1-5: The schematic diagram of InGaP/GaAs tandem junction solar cells. (proposed by Takamoto et. al.)	8
Fig. 1-6: The diagram of solar cell spectral intensity for different photovoltaic cells (a-Si:H solar cells and c-Si solar cells).	8
Fig. 1-7: The diagram of solar tracking system.	10
Fig. 1-8: (a, c, e) SEM images in a large area of a monolayer of silica nanoparticles, a-Si:H NC arrays, and a-Si:H NW arrays, respectively. (b, d, f) zoom-in SEM images of silica nanoparticles, a-Si:H NCs, and a-Si:H NWs, respectively. [3]	10
Fig. 1-9: Nanodome a-Si:H solar cell structure. SEM images taken at 45° on (a) nanocone quartz substrate and (b) a-Si:H nanodome solar cells after deposition of multilayers of materials on nanocones. (Proposed by Zhu et al.) Scale bar 500 nm. (c) schematic showing the cross-sectional structure of nanodome solar cells. [23]	12
Fig. 1-10: The sketched diagram of refractive index between two non-absorbed material with different refractive index. The refractive index of material in sample (b) with refractive index, n_2, possessed the higher reflectance than sample (a). (The relationship of refractive index in sample (a) and (b) is$1 < n_1 < n_2$.)	12
Fig. 2-1: (a)The device structure of the n-GZO/p-Si heterojunction photodiode with silica nanoparticles coated on the light illuminating surface (b) Top view of the device.	24
Fig. 2-1: (c) Plane view of SEM image for the monolayer silica nanoparticles on the n-GZO surface (10,000 X). (d) dense arrangement of silica nanoparticle on the n-GZO surface (55,000 X).	26
Fig. 2-2: AFM diagrams of the surface profiles for the conventional (a) and nanoparticle coated (b) n-GZO/p-Si photodiodes.	28

Fig. 2-3: Current-voltage curve of Ni/Au on p-Si with the different annealing conditions.	29
Fig. 2-4: The current-voltage curve of the n-GZO/p-Si photodiode (a). The semi-log current-voltage curve of photodiode with and without SiO_2 nanoparticles (b).	31
Fig. 2-5: The current-voltage curve of Ni/Au on p-Si (c) and Ti/Au on n-GZO (d). They both showed the characteristics of ohmic contact under optimum annealing condition.	32
Fig. 2-6: Experimental setup for the optical response measurement of photodiodes.	33
Fig. 2-7: Spectral photoresponsivities of the conventional (solid line) and nanoparticle coated (dashed line) n-GZO/p-Si photodiodes.	33
Fig. 2-8: The sketched diagram of refractive index issue between n-GZO/p-Si photodiode with (a) and without (b) SiO_2 nanoparticle coated photodiodes at the wavelength of 600nm.	35
Fig. 2-9: The sketched diagram of light trapping in the interface of SiO_2 nanoparticle and air.	35
Fig. 2-10: Normalized photocurrents of both conventional and nanoparticle coated photodiodes under different incident angles at the wavelength of 500nm(a), 550nm(b). The photocurrents are normalized to the photocurrent of the conventional photodiode at 0^o.	37
Fig. 2-10: Normalized photocurrents of both conventional and nanoparticle coated photodiodes under different incident angles at the wavelength of 600nm(c) and 700nm(d). The photocurrents are normalized to the photocurrent of the conventional photodiode at 0^o.	38
Fig. 2-11: Difference of normalized photocurrents between the nanoparticle coated and conventional photodiodes at the wavelength 500nm(a), 550nm(b).	40
Fig. 2-11: Difference of normalized photocurrents between the nanoparticle coated and conventional photodiodes at the wavelength 600nm(c) and 700nm(d).	41
Fig. 2-12: The possible morphology of silica nanoparticle arrangement. (a) square and (b) hexagonal arrangement.	43
Fig. 3-1: The plane-view SEM diagram of silica nanosphere with 100nm diameter spraying on the p^+-Si substrate.	49
Fig. 3-2: The plane-view SEM images (20,000X) showed the dense arrangement of surface morphology on the p^+-Si substrate after RIE dry etching.	49
Fig. 3-3: The plane-view SEM images (20,000X) showed the sparse arrangement of surface morphology on the p^+-Si substrate after RIE dry etching.	50

Fig. 3-4: The cross-section SEM diagram showed the nano-pyramid surface morphology under the receipt A in Table 3-1 for RIE dry etching.	52
Fig. 3-5: The cross-section SEM diagram showed the nanorod surface morphology under the receipt B in Table 3-1 for RIE dry etching.	52
Fig. 3-6: The plane-view SEM images (60,000X) showed the surface morphology of nanopatterned p^+-Si substrate before a-Si(i) thin film deposition on nanopatterned p^+-Si substrate.	53
Fig. 3-7: The plane-view SEM images (60,000X) showed the surface morphology of nanopatterned p^+-Si substrate after a-Si(i) thin film deposition on nanopatterned p^+-Si substrate.	53
Fig. 3-8: The cross-section diagram of SEM showed the nanocone morphology in the nanopatterned p^+-Si after the a-Si(i) deposition by HDP-CVD. The a-Si(i) thin film showed the uniform surface morphology.	55
Fig. 3-9: The plane-view diagram of SEM showed the uniform arrangement of nanopatterned a-Si(i) with 100nm diameter after RIE dry etching.	55
Fig. 3-10: The cross-section SEM diagram of nanorod a-Si(i) with 50nm height. The thickness of un-etching a-Si thin film is around 70nm.	57
Fig. 3-11: Device structures of (a) planar n-GZO/p^+-Si (device A), (b) planar n-GZO/a-Si(i)/p^+-Si (device B), (c) n-GZO/nanopatterned a-Si(i)/p^+-Si (device C) and (d) n-GZO/a-Si(i)/nanopatterned p^+-Si (device D).	59
Fig. 3-12: The cross-section view of SEM diagrams of a nanopatterned p^+-Si substrate (a) and a-Si(i) thin film on nanopatterned p^+-Si substrate (b).	60
Fig. 3-13: The current-voltage curve showed the contact characteristics of Al/p^+-Si under 350^{o}C post annealing temperature for 1, 3 and 5 mins (a) and 400^{o}C post annealing temperature for 1, 3 and 5mins (b), respectively.	61
Fig. 3-14: The current-voltage curves of Ti/Au on n-GZO under different activation condition (300^{o}C and 400^{o}C) annealing time, 5min (a) and 10min (b), under 400^{o}C annealing temperature.	63
Fig. 3-15: I-V curves of the photodiodes under comparison (Bottom : (left) The I-V curve of the Al contact on p^+-Si; (right) The I-V curve of the Au/Ti contact on n-ZnO. Both curves show good ohmic contact.	66
Fig. 3-16: Photoresponsivity curves of the device A, B, C, and D.	68
Fig. 3-17: The schematic diagram of reflectance measuring instrument. The measured sample was tiled 5^o angle embedded into the integrating sphere. The detector could measure the total reflectance (specular and diffused reflectance). The light source was combined of deuterium and halogen lamp with wavelength	68

300nm to 800nm.	
Fig. 3-18: The comparisons of the reflectivity between planar and nanopatterned p^+-Si surfaces. Black solid and red dashed line indicated the reflectivity of planar p^+-Si and nanopatterned p^+-Si substrate, respectively.	71
Fig. 3-19: The reflectivity between planar a-Si and nanopatterned a-Si layers on planar p^+-Si substrates. Black solid and red dashed lines indicated the planar a-Si (i) thin film/p+-Si and nanopatterened a-Si (i)/p^+-Si devices, respectively.	71
Fig. 3-20: Comparisons of the acceptance angles of device B, C, and D at the wavelength 450nm. The photocurrents are normalized to the photocurrent of the conventional photodiode at 0^o.	73
Fig. 3-21: Comparisons of the acceptance angles of device B, C, and D at the wavelength 550nm(b). The photocurrents are normalized to the photocurrent of the conventional photodiode at 0^o.	73
Fig. 3-22: Comparisons of the acceptance angles of device B, C, and D at the wavelength of 650nm. The photocurrents are normalized to the photocurrent of the conventional photodiode at 0^o.	74
Fig. 3-23: Comparisons of the acceptance angles of device B, C, and D at the wavelength of 650nm(c) and 750nm (d). The photocurrents are normalized to the photocurrent of the conventional photodiode at 0^o.	74
Fig. 3-24: Experimental setup for transit time measurement of heterojunction photodiodes.	76
Fig. 3-25: EL (Electroluminescence) spectra of different wavelength LEDs.	76
Fig. 3-26: The curve of transit time under constant incident light intensity on device B, C and D at the wavelength of 633.3nm.	78
Fig. 3-27: The rising time of device B, C and D under constant incident light intensity.	80
Fig. 3-28: The falling time of device B, C and D under constant incident light intensity.	81
Fig. 3-29: The sketched diagram showed the mechanism of carrier transportation between planar and nanopatterend photodiodes. The nanostructure could offer the shorter transit paths in the device.	81
Fig. 3-30: The curve of transit time under constant photocurrents for device B, C and D at the wavelength of 591.4nm.	84
Fig. 3-31: The rising time of device B, C and D under constant photocurrents.	86

Fig. 3-32: The falling time of device B, C and D under constant photocurrents.	86
Fig. 3-33: The sketched diagram showed the mechanism of carrier transportation between planar and nanopatterned photodiodes.	87
Fig. A1-1: The PL diagram of n-ZnO after post annealing. The device under 550^{o}C 30min post annealing could possess the better photoluminescence characteristics and have the peak wavelength at 380nm.	95
Fig. A1-2: The diagram of transition mechanism of defects in ZnO.	95
Fig. A1-3: The XRD indicated the high c-axis orientation (0002) was observed under the anneal condition, 550^{o}C and 30mins.	97
Fig. A1-4: Schematic diagram of n-ZnO/p-GaN (a) and n-ZnO/SiO_2 (3nm)/ p-GaN (b) LEDs, respectively.	97
Fig. A1-5: PL spectra of RF sputtered n-ZnO (dashed line) and MOCVD grown p-GaN (solid line)	100
Fig. A1-6: I-V curves of a n-ZnO/p-GaN LED (solid line) and a n-ZnO/SiO_2 (3nm)/p-GaN LED (dashed line).	100
Fig. A1-7: The current voltage curve of Ni/Au on p-GaN (a) and Ti/Au on n-ZnO (b) were indicated the ohmic-like behavior under optimum post anneal condition.	102
Fig. A1-8: EL spectrum of n-ZnO/SiO_2/p-GaN LEDs before (black solid rectangular) and after (red hollow circle) rapid temperature annealing (RTA).	103
Fig. A1-9: (a) EL spectra of a n-ZnO/p-GaN LED. The bias current ranges from 5mA to 30mA at a step 5mA.	103
Fig. A1-9: (b) EL spectra of and a n-ZnO/SiO_2(3nm)/p-GaN LED. The bias current ranges from 5mA to 30mA at a step 5mA.	106
Fig. A1-10: Bandgap diagram of the n-ZnO/SiO_2/p-GaN structure.	106
Fig. A1-11: EL spectra of n-ZnO/SiO_2/p-GaN LEDs with different SiO_2 thicknesses. The bias current is 20mA.	107
Fig. A2-1: Dark (black solid line) and UV-illuminated (red dashed line) I-V curves of the n-ZnO/p-GaN photodiode (a), the current voltage diagrams of Ni/Au on p-GaN (b) and Ti/Au on n-ZnO (c).	113
Fig. A2-2: Room temperature XRD spectra of sample A (n-ZnO on p-GaN) and sample B (n-ZnO on p-Si) under the same activated condition, 550^{o}C for 30mins.	115
Fig. A2-3: The current-voltage curve of n-ZnO/p-GaN photodetector under differentoptical powers at 375nm.	115

Fig. A2-4: Measured spectral responsivity of n-ZnO/p-GaN photodiodes. The device is biased at -5V.	117
Fig. A2-5: Bandgap diagram of the n-ZnO/p-GaN heterostructure.	117

List of Tables

Table 1-1: Confirmed terrestrial cell and sub module efficiencies measured under the global AM1.5 spectrum (1000W/m2) at 25^{o}C (IEC 60904-3: 2008, STM G-173-03 global). This table is come from Solar Cell Efficiency Tables (Version 33), Prog. Photovolt: Res. Appl. 2009 **17** : 85–94. [4]	4
Table 3-1: The table listed the detail information of RIE dry etching receipt for nanopatterned fabrication on devices.	50
Table 3-2: The nanopatterned size of p^{+}-Si and a-Si(i) after reactive ion etching (RIE) dry etching and the a-Si(i) thin film deposited by High Density Plasma Chemical Vapor Deposition (HDP-CVD) The RIE process was performed by Samco RIE-10NR.	57
Table 3-3: The name lists of heterojunction photodiodes A, B, C and D	60
Table 3-4: The lists of metal contact test were recorded in this table. From the above table, we could perform the one step annealing process of metal contact to prevent from the second thermal annealing damages.	65
Table 3-5: The speculations of LED emission peak wavelength and FWHM (Full Width Half Maximum).	78
Table 3-6: The transit time of device B, C and D under constant incident light intensity with different wavelength.	80
Table 3-7: The transit time of device B, C and D under constant photocurrents.	84
Table A1-1: The table showed the PL emission information under different activation temperature and annealing conditions.	102

Chapter 1

Introductions

1-1 Historical reviews of solar cells

1-1-1 Energy shortage

Solar cells have attracted more attentions for recently decades due to the energy shortage and environmental issue. There are many advantages on solar cells such as clean, renewable and no toxic, et.al. The International Energy Outlook 2009, shown in Fig. 1-1, indicated that world marketed energy consumption is projected to rise by 44 percent from 2006 to 2030. Total energy demand in the non-OECD (Organization for Economic Co-operation and Development) countries increases by 73 percent, compared with an increase of 15 percent in the OECD* countries. Unconventional sources including biofuels could provide nearly half of the growth in global liquid fuel supplies during 2006-30 and global emissions of the main greenhouse gas carbon dioxide will jump more than 39 percent by 2030, without new policies and binding pacts to cut global warming pollution. The issue of energy requirement in the world becomes more and more serious. For the serious issue on the shortage of oil, gas and other non-renewable energy resources, we must do more efforts as soon as possible on researches of renewable energy such as, photovoltaics, winds and biomass energy.

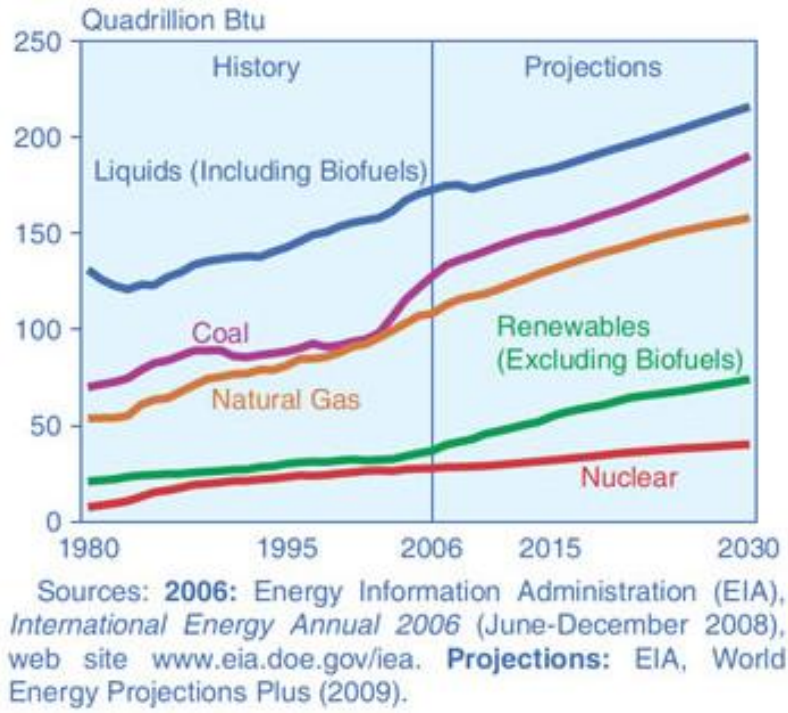

Fig. 1-1: International Energy Outlook 2009: World marketed energy consumption is projected to rise by 44 percent from 2006 to 2030.

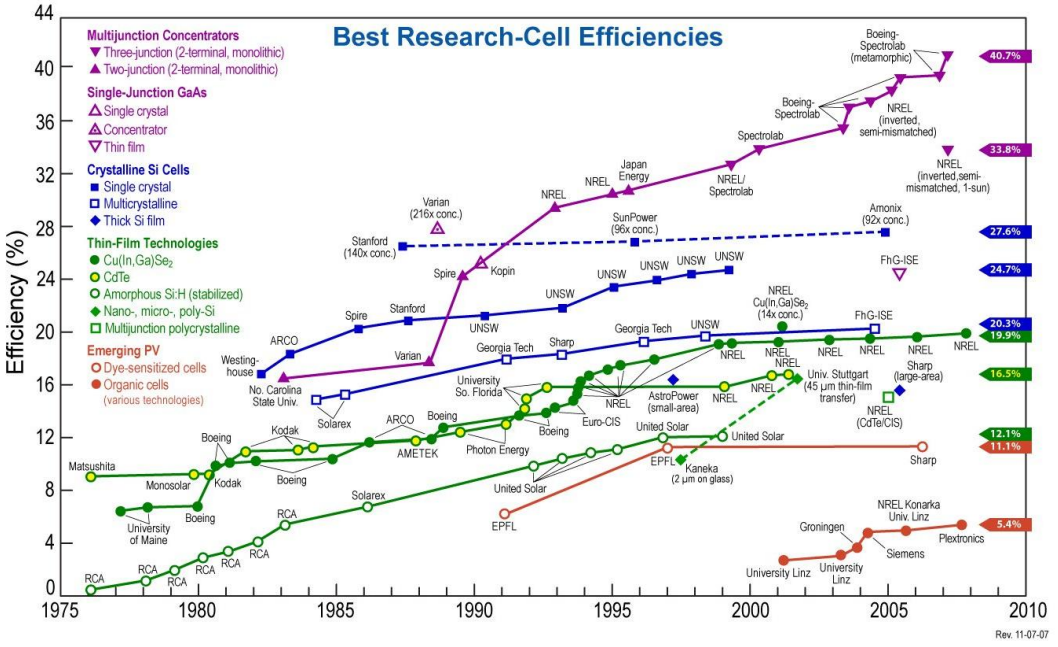

Fig. 1-2: The researched solar cell efficiency progresses from 1975 to 2008.

1-1-2 Solar cells progress

After 1980s, photovoltaics became a popular power source for consumer electronic devices, including calculators, watches, radios and other small battery-charging applications. Following the energy crisis of the 1970s, significant efforts also began to develop PV power systems for residential and commercial uses, both for stand-alone, remote power as well as for utility-connected applications.

The classifications of solar cells are separated according to material and structure, single crystalline Si, polycrystalline Si, amorphous Si thin film, III-V, multiple junction and other solar cells. The world records of solar cells are listed in Table 1-1 which adapted from the reference [4] . And the solar cell best research-efficiencies are plotted in Fig. 1-2. After 2000, the conversion efficiency of Si based solar cell has the drastic growth due to the successful fabrication of periodic textured surface and back surface field on solar cells. Green et al. addressed the 25% conversion efficiency PERL (Passivated Emitter Rear Locally) diffused solar cells [1], shown in Fig. 1-3. Periodic surface textured structure is fabricated to trap more incident lights and localized back surface field is fabricated to increase carrier life time. However, the complicate device fabricating process will cause the large cost on mass production in the industry. However, crystalline GaAs based solar cells possessed the 26.1% conversion efficiency and was proven by Bauhuis et al. in 2004 [2], shown in Fig. 1-4. It's hard to mass

Classification	Effic. (%)	Area (cm^2)	V_{oc} (V)	J_{sc} (mA/cm^2)	FF (%)	Test centre (and date)	Description
Silicon Based							
Si (crystalline)	25	4.0	0.705	42.7	82.8	Sandia (3/99)	UNSW PERL
Si (multicrystalline)	20.4	1.002	0.664	38.0	80.9	NREL (5/04)	FhG-ISE
Si (thin film transfer)	16.7	4.017	0.645	33.0	78.2	FhG-ISE (7/01)	U. Stuttgart (45mm thick)
Si (thin film submodule)	10.5	94	0.492	29.7	72.1	FhG-ISE (8/07)	CSG Solar (1-2mm on glass; 20 cells)
III-V Semiconductor							
GaAs (crystalline)	26.1	0.998	1.038	29.7	84.7	FhG-ISE (12/07)	Radboud U. Nijmegen
GaAs (thin film)	26.1	1.001	1.045	29.5	84.6	FhG-ISE (07/08)	Radboud U. Nijmegen
GaAs (multicrystalline)	18.4	4.011	0.994	23.2	79.7	NREL (11/95)	RTI, Ge substrate
InP (crystalline)	22.1	4.02	0.878	29.5	85.4	NREL (4/90)	Spire, epitaxial
Amorphous/Nanocrystalline Si							
Si (amorphous)	9.5	1.070	0.859	17.5	63.0	NREL (4/03)	U. Neuchatel
Si (nanocrystalline)	10.1	1.199	0.539	24.4	76.6	JQA (12/97)	Kaneka (2mm on glass)
Multiple Junction Solar Cells							
GaInP/GaAs/Ge	32	3.989	2.622	14.37	85.0	NREL (1/03)	Spectrolab (monolithic)
GaInP/GaAs	30.3	4	2.488	14.22	85.6	JQA (4/96)	Japan Energy (monolithic)
GaAs/CIS (thin film)	25.8	4				NREL (11/89)	Kopin/Boeing (4 terminal)
a-Si/mc-Si (thin submodule)	11.7	14.23	5.462	2.99	71.3	AIST (9/04)	Kaneka (thin film)

Table 1-1: Confirmed terrestrial cell and sub module efficiencies measured under the global AM1.5 spectrum (1000W/m2) at 25°C (IEC 60904-3: 2008, STM G-173-03 global). This table is come from Solar Cell Efficiency Tables (Version 33), Prog. Photovolt: Res. Appl. 2009 **17** : 85–94. [4]

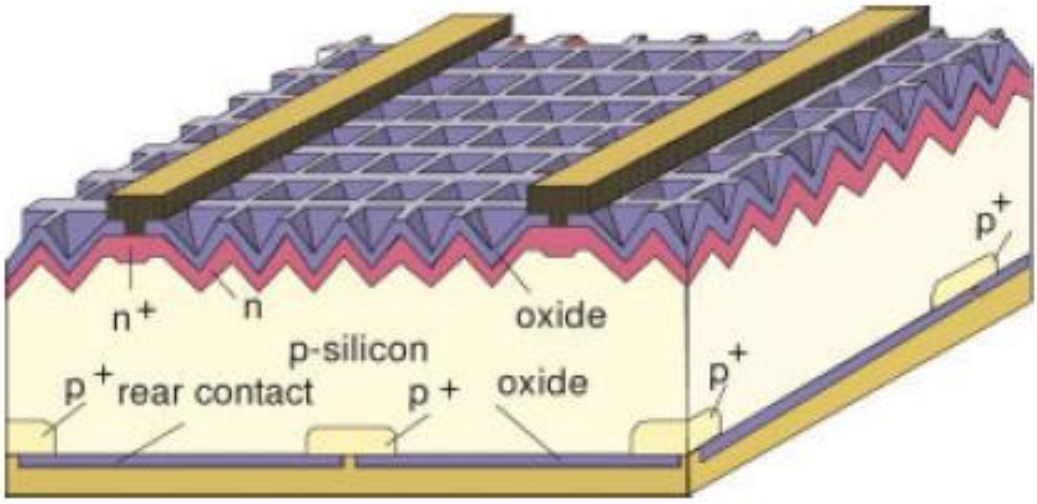

Fig. 1-3: The sketched diagram of PERL (Passivated Emitter Rear Locally) diffused solar cells. (Proposed by Green et al.) [1]

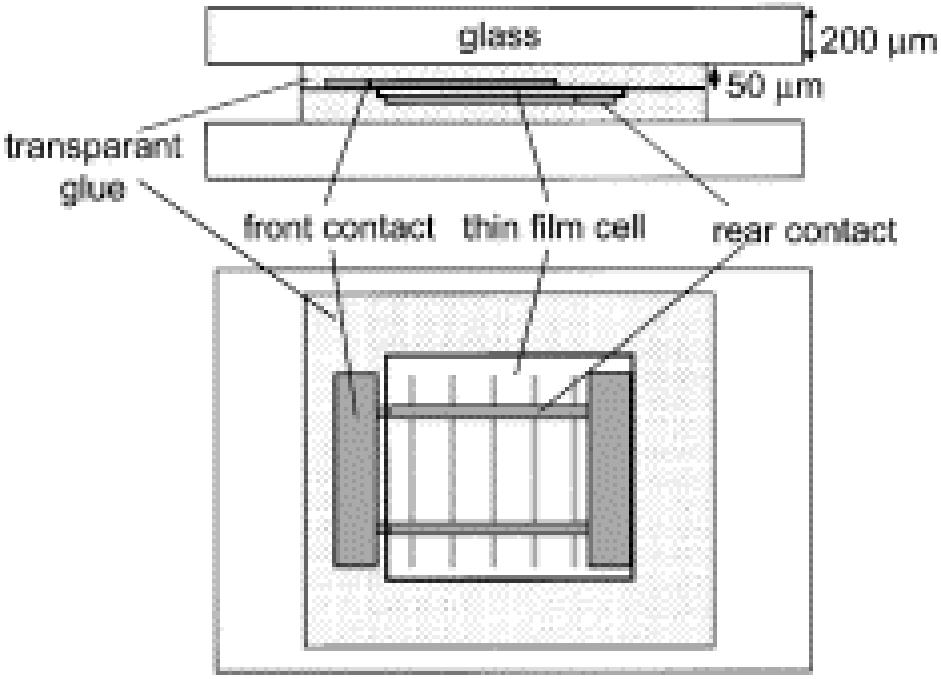

Fig. 1-4: The schematic diagram of GaAs based solar cells with the 26.1% conversion efficiency. (Proposed by Bauhuis et al.) [2]

produce the GaAs based solar cells which is due to the cost of material and complicate device fabricating process compared to crystalline Si based solar cells. Although GaAs based solar cells have the higher conversion efficiency compared to crystalline Si based solar cells, it just could be used in space applications. In order to match the solar spectrum on light absorption, the concept of multiple junction solar cells are proposed and the world record conversion efficiency is 30.3% which is fabricated by Takamoto et al., in 1997 [5]. Due to the considerations of low cost and easy device fabrications, a-Si thin film solar cells are successfully fabricated and the world record conversion efficiency is 9.5% by Meier et al. in 2004 [6]. However, the third generation solar cells are also attracted lots of attentions due to its' easy fabricating process and low material cost. However, the material choices of third generation solar cells mainly focus on non-Si based materials. Furthermore, organic based and dye sensitized solar cells have the potential improvements by optimizing the material and interface qualities.

1-1-3 Bottlenecks of solar cells

Generally speaking, solar cell conversion efficiency is mainly limited by below factors, more light absorptions, broad absorption band, wide acceptance angle and low carrier recombination in devices. We will introduce these factors on the impacts for solar cell conversion efficiency and try to provide the possible solutions on the

improvements of solar cell conversion efficiency.

A. Broad band absorption

The choice of material used in the photovoltaic cell plays an important key role on high conversion efficiency. The diagram of solar cell spectral intensity was shown in Fig. 1-6. Crystalline silicon based solar cells are dominated the absorption band spectrum between 800nm to 1000nm [7]. However, a-Si:H solar cells are dominated the absorption band spectrum between 500nm to 700nm [8]. It's few to discuss the materials with absorption band spectrum below 500nm for solar cell applications. From this viewpoint, it's important to enhance the conversion efficiency by combining the semiconductor materials with different band gap to fabricate the multiple junctions such as tandem solar cells [5, 9-21], et al. However, tandem solar cells have higher conversion efficiency compared to single junction solar cells which is due to multiple absorption bands. However, from the numerical calculations, we also observed the same phenomena that conversion efficiency of triple junctions will be higher than it in double junctions. It indicated that broad band absorption on solar cells will result in the high conversion efficiency. However, the critical issue is series resistance exited in the boundary of junctions will decrease the short circuit currents and result in the low conversion efficiency. Past works spent lots of efforts on the discussion of boundary

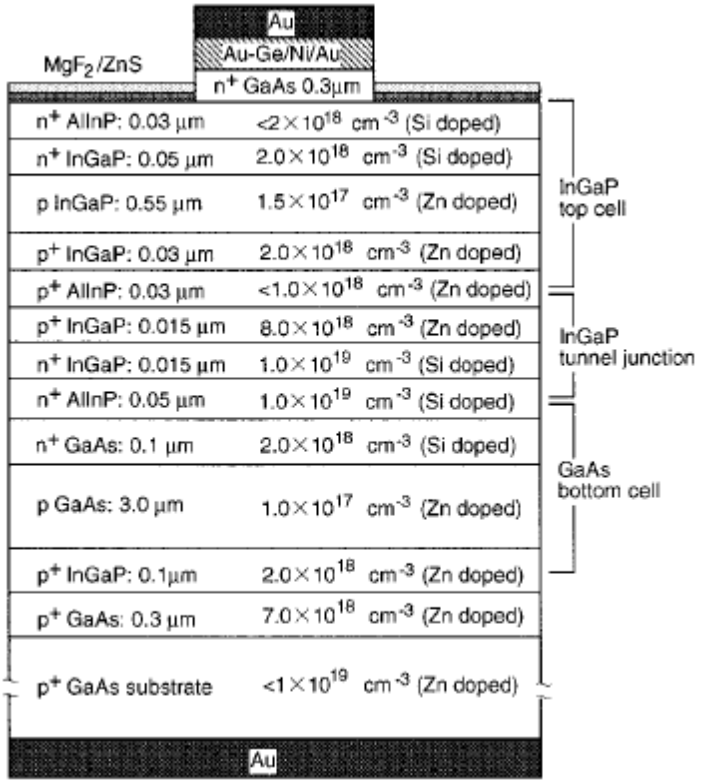

Fig. 1-5: The schematic diagram of InGaP/GaAs tandem junction solar cells. (proposed by Takamoto et. al.)

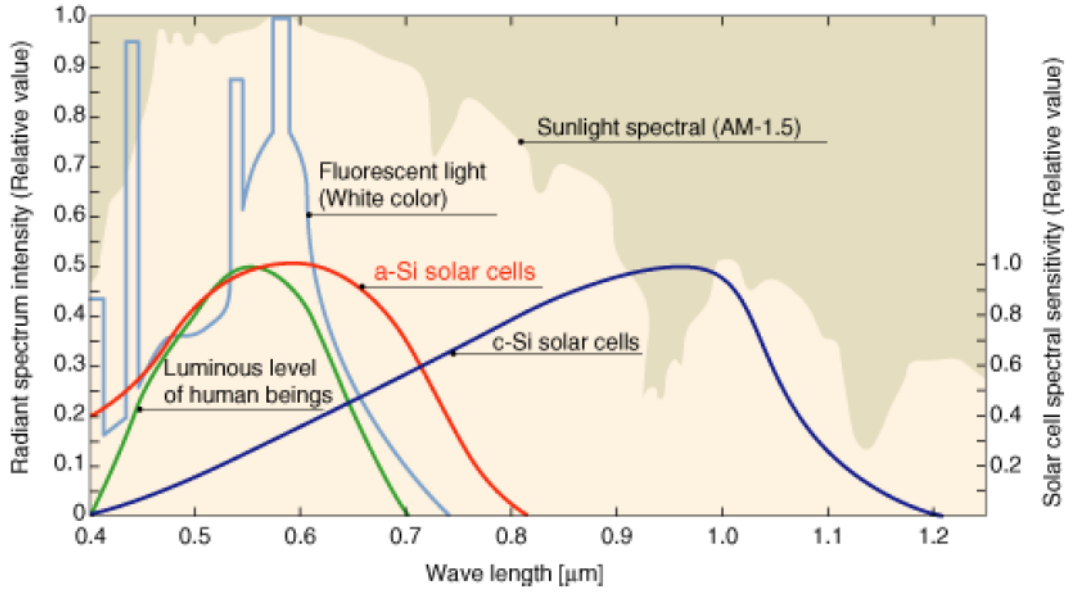

Fig. 1-6: The diagram of solar cell spectral intensity for different photovoltaic cells (a-Si:H solar cells and c-Si solar cells).

effect of tandem solar cells . However, the critical issue is still serious when the numbers of junction more than four. In this dissertation, we designed the heterojunction photodiode by combining the high and low energy band gap to investigate the broad band absorption characteristics. And it will has the potential applications to solar cells.

B. Wide acceptance angle

In the daytime, the angle of incident light is varied and the effective power of incident light on solar panel is also different. However, for typical photodiodes or solar cells the efficiency has the maximum value under normal incidence and decreases continuously as the incident light with a fixed light intensity is tilted further from the vertical direction. Therefore, the solar panels are usually installed at an angle that maximizes average light absorption during the daytime. Acceptance angle is defined as the 90% incident power compared to 0^o incident (normal to incident surface). Another approach to improve light absorption efficiency is by setting up a tracking system, shown in Fig. 1-7, to maintain normal incidence of solar light for most of the incident angles, which has the disadvantages of additional power consumption and complication of system design [22]. The discussions on angle-dependent absorption for solar cell applications are also few to respect. From recently paper, Zhu et al. [3], on discussion of nanowire optical characteristic, angle-dependent reflectance measurement

Fig. 1-7: The diagram of solar tracking system.
http://thefraserdomain.typepad.com/energy/solarthermal/

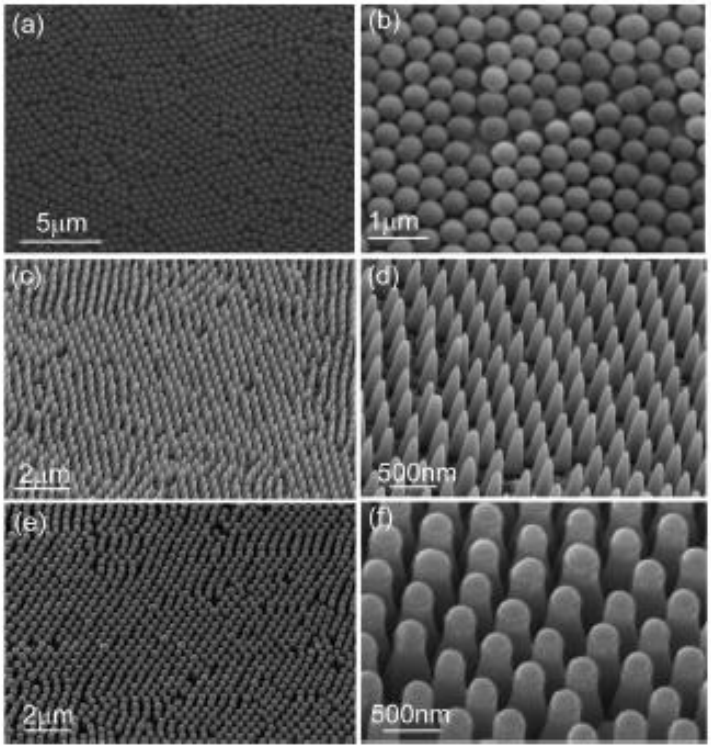

Fig. 1-8: (a, c, e) SEM images in a large area of a monolayer of silica nanoparticles, a-Si:H NC arrays, and a-Si:H NW arrays, respectively. (b, d, f) Zoom-in SEM images of silica nanoparticles, a-Si:H NCs, and a-Si:H NWs, respectively. [3]

showed the wide absorption angle could be achieved in nanowire devices. Nnaocone structure devices which are fabricated by using an easily scalable process could have the wide absorption angle and the SEM diagrams of devices are shown in Fig. 1-8. Nanodome solar cells which is fabricated by using Langmuir-Blodgett assembly of close packed monodisperse SiO_2 nanoparticles has been proposed to enhanced conversion efficiency on a-Si:H solar cells, the device structure was shown in Fig. 1-9. The enhancement of conversion efficiency is due to the hydrogenated amorphous silicon (a-Si:H) layer can absorb 94% of the light with wavelengths of 400-800 nm, significantly higher than the 65% absorption of flat film [23]. The characteristic of acceptance angle on nanostructure photodiodes is still not investigated deeply [24]. However, it's important to improve the acceptance angle on the stable power output of solar cells in daytimes.

C. Low reflectance on solar cells

High reflectance of device surface will cause the inefficient absorption and lower conversion efficiency for solar cells. Past researches tried to decrease the reflectance by fabricating the rough surface [25-26], periodic textured surface [27-34] or textured substrate [35-37] to trap more incident light and decrease the difference of refractive index between air and semiconductor. On the other hand, periodic textured surface,

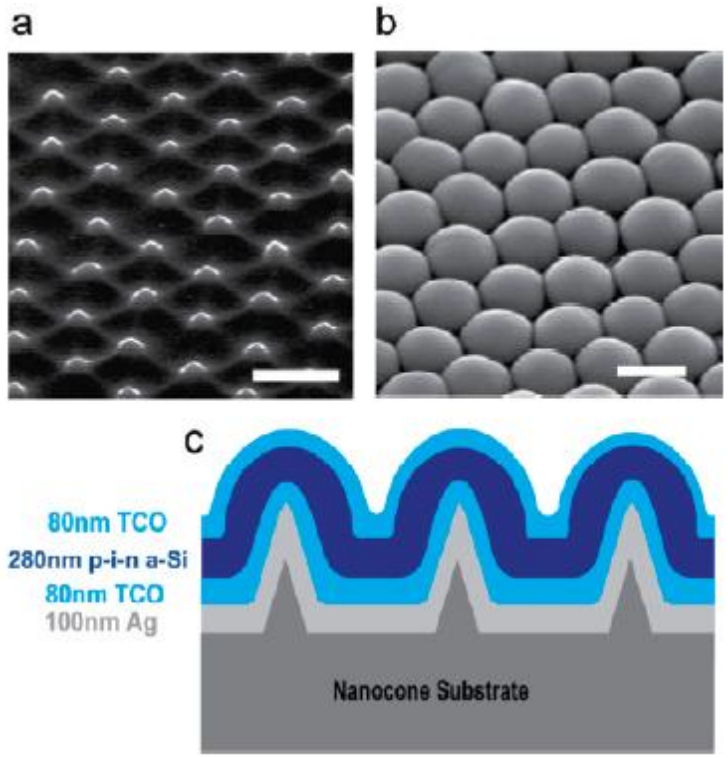

Fig. 1-9: Nanodome a-Si:H solar cell structure. SEM images taken at 45° on (a) nanocone quartz substrate and (b) a-Si:H nanodome solar cells after deposition of multilayers of materials on nanocones. (Proposed by Zhu et al.) Scale bar 500 nm. (c) Schematic showing the cross-sectional structure of nanodome solar cells. [23]

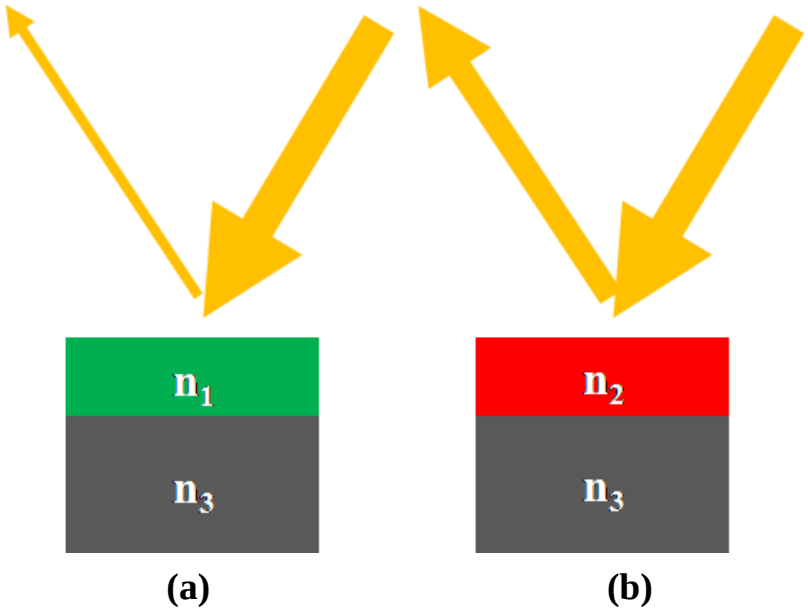

Fig. 1-10: The sketched diagram of refractive index between two non-absorbed material with different refractive index. The refractive index of material in sample (b) with refractive index, n_2, possessed the higher reflectance than sample (a). (The relationship of refractive index in sample (a) and (b) is$1 < n_1 < n_2$.)

transparent conductive oxide (TCO) coating [38-42], nanowires [43-48] and the design of surface plasmon [49-55] have also been reported to reduce the surface reflectivity of the device so that more photons can be trapped in the devices. The main issue on the reflectance is due to the mismatch between two non-absorbed materials and could be realized in Fig. 1-8. The reflectance R at normal incidence at the interface between two non-absorbing media of refractive index n_0 and n_1 is given by below equation and the sketched diagram was shown in Fig. 1-8 for the comparison on refractive index.

$$R = [(n_0 - n_1)/(n_0 + n_1)]^2$$

From the above mentions, the refractive index could be effective decreasing by fabricating the nanostructure on solar cells and it's possible to enhance the conversion efficiency.

D. Carrier recombinations

Another issue on solar cell conversion efficiency is carrier recombination in device. Hydrogenated amorphous Si (a-Si:H) thin film solar cells has lower conversion efficiency compared to crystalline Si solar cells which is due to the worse material and junction boundary quality. Vukadinovic et al. [56] indicated the degradation of intrinsic (undoped) a-Si:H layer of a p-i-n solar cells under illumination, the Staebler-Wronski effect, could be reduced by stacking two or three p-i-n cells with thin

intrinsic layers. The insertion of intrinsic layer will result in the longer carrier transit path. The design on the thickness of intrinsic layer needs to be optimized. From the past works, it is attracted more attentions on how to improve the material and junction boundary quality . However, another approach is how to effectively decrease the transit path without destroying the device quality and it is possible to fabricate high conversion efficiency solar cells. In this dissertation, we fabricate the nanostructure photodiodes to investigate the characteristics of short transit time which could provide the shorter transit path to contact electrodes for carriers compared to the conventional devices.

1-2 Historical review of ZnO based heterojunction optoelectronic devices

ZnO, with the band gap of 3.37eV, was one potential material to fabricate the UV light emitting diodes (LEDs), laser diodes (LDs) and photodetectors (PDs). It possessed the unique characteristics such as the larger excition binding energy of 60meV (versus 26meV for GaN) [57], easy fabricating process due to amenability to conventional chemical wet etching, and the possibility of low-temperature growth by RF sputtering. In this chapter, we introduced the characterisitics of ZnO based optoelectronic devices in light emitting diodes, photodetectors and nanostructure optoelectronic devices, respectively.

1-2-1 ZnO based Heterojunction Light Emitting Diodes (LEDs)

Due to the difficulty of p-ZnO growth [58-64] , many papers were focused on the fabrication of n-ZnO and other p-type semiconductor substrate such as p-GaN [65-75] , SiC [76-81] and Si [24, 82-88], etc. From the past reports, several different emission wavelengths of ZnO heterostructure LEDs have been presented, ranging from UV emission at 375–389 nm to wide band spectra violet-white to blue-white. For example, Ataev et al. [74] compared growth of n-ZnO:Ga by chemical vapor deposition CVD on both p-GaN:Mg/c-Al_2O_3 and p-$Al_{0.12}Ga_{0.88}N$:Mg/6H-SiC structures. The wavelength maximum is 430 nm for ZnO/GaN LEDs and 389 nm for ZnO/AlGaN devices. It was inferred that electron injection from the n-ZnO into the p-GaN should be more energetically favorable than hole injection from the p-GaN into n-ZnO, while hole injection from p-AlGaN into n-ZnO will be more favorable than electron injection from n-ZnO into p-AlGaN. Furthermore, Jiao et al. fabricated n-ZnO/p-GaN diodes with a MgO thin film for electron blocking layer [89]. The result showed an EL emission peak wavelength at 380 nm. From the result in the paper of Jiao et al. [89], the current blocking layer could be one candidate for the fabrication of ZnO based UV emission light emitting diodes (LEDs). Recently, Ke et al. successfully control the ZnO based LED's EL emission at 377nm by using the sandwich structure.

1-2-2 ZnO based Heterojunction Photodetectors (PDs)

The ZnO-based photodetector has superior resistance to ionizing radiation and high energy particles, and does not require an antireflection layer. Therefore, the high UV-to-visible wavelength rejection ratio ZnO detectors can be applied to space communications, ozone layer monitoring and flame detection. In the past several years, ZnO Schottky diodes and metal-semiconductor-metal (MSM) photodiodes have been successfully demonstrated [90-93]. Despite excellent performance of ZnO Schottky diodes, the development of ZnO based p-n homojunction detectors is, however, relatively slow since a reproducible high-quality p-type ZnO is very difficult to grow. The alternative approach for fabricating ZnO p-n photodiodes is to grow n-type ZnO on other mature p-type semiconductors. So far, p-n heterojunctions which combine ZnO as the n-type layer and Si [24, 82-88], SiC [76-81], or NiO [94-97] as the p-type material have been reported. In most cases, the performance of ZnO p-n heterojunction photodiodes is inferior to Schottky or MSM diodes due to the lattice mismatch between p-type and n-type layers, resulting in a large number of junction defects and leakage currents. In addition, the ultraviolet (UV)-to-visible photoresponse rejection ratios of devices using p-Si or p-SiC are limited by the intrinsic properties of visible wavelength absorption. Another, among those ZnO heterojuntion diodes, the n-ZnO/p-Si structure is also of particular interest. Previous reports indicated a relative flat spectral responsivity

around 0.1~0.3 (A/W) in the wavelength range between 400 and 800nm for n-ZnO/p-Si photodiodes, as compared with the decrease of the spectral response toward shorter wavelength from the Si band edge for typical Si detectors [24, 82-83, 88, 98-102]. As a result, the ZnO/Si heterostructure has the advantage of improving light absorption in the visible wavelength and thus possesses the potential of solar cell applications.

1-2-3 Nanostructure optoelectronic devices progress on solar cell applications

Many semiconductors materials have the potentials to fabricate as nanostructure by the top-down or bottom-up processes. Top-down process on nanostructure optoelectronic device fabrications, such as LEDs etc., has drastic progress due to the stable and easy fabricating processes of nanosphere lithography. However, bottom-up process such as VLS (Vapor Liquid Solid), MBE (Molecular Beam Epitaxial) and MOCVD (Metal Organic Chemical Vapor Deposition) for nanostructure device fabrications are still limited by the complicated process and high cost on material deposition. On the application of solar cells, nanostructure played an important role on light absorption due to its low surface reflectance. Zhu et al. [3] indicated the nanocone structure have the wider incident angle of absorbance than the nanorod structure which nanostructure was fabricated by nanosphere lithography. Zhu et al. [23]proposed the nanodome solar cells using the Langmuir-Blodgett assembly of close packed

monodisperse SiO_2 nanoparticles and 5.9% conversion efficiency was achieve in a-Si:H solar cells with the 25% enhancement compared to the flat film control sample. Generally speaking, when the incident light is tilted, photons have more chances to fall within the angle of internal reflection for the nanocone structure and thus the acceptance angle is increased. Huang et al. [103] also reported the dark 6 inch Si substrate by applying the technique of self-masked dry etching to fabricate the SiNT (Silicon Nano Tube). The above reports just focus on the high absorption of nanostructure materials in the discussion of optical characteristics. Discussions on devices are still few due to the difficult device fabricating processes. Krunks et al. [104] applied ZnO nanorods on the applications of solar cells and successfully improved the conversion efficiency. The improvement of conversion efficiency is still due to the much more incident light absorbed by trapping effect on nanostructure. However, despite excellent performance from those reports, sub-wavelength textured morphology in the intrinsic light absorption layer was ever reported [105]. The nanoscale patterns in the light absorbing intrinsic layer have several advantages. In addition to a more efficient light interaction with the textured layer, the sub-wavelength periodicity has a similar size to the intrinsic layer thickness; which reduces the transit time for generated carriers transporting to the contact electrodes. It indicated that advantages of nanostructure on solar cells are not just reduced surface reflectivity but also shortened the carrier transit path. It's possible

to reduce the possibility of carrier recombination by shortening the transit path.

1-3 Dissertation overviews

As a potential answer to the challenge motioned above, this dissertation presents a ZnO based optoelectronic devices included with light emitting diodes (LEDs) utilizing the SiO_2 thin layer to well confine the emission wavelength at 394nm for the n-ZnO/p-GaN light emitting diodes (LEDs) and photodetectors (PDs) utilizing the technique of nanosphere spyaying to fabricate the nanostructure photodiodes by the combination of n-GZO/a-Si(i)/p-GaN. Due to the completeness of dissertation, the above discussions are presented in appendix 1 and 2.

Chapter 2 investigates the potential application of n-ZnO/p-Si photodiodes on the broad band absorption of broad band spectrum and the advantage of nanosphere on the application of wide acceptance angle on photovoltatic cells. The mechanism of enhanced acceptance angle was realized by Bragg diffraction. Following, chapter 3 focus on the characterization and fabrication of nanostructure n-GZO/a-Si/p^+-Si p-i-n photodiodes. The discussion was mainly focus on the transit time of photodiodes with and without nanopatterns. Furthermore, the relationships between photoresponsivity, characterization of nanostructure and transit time was demonstrated in this chapter. The nanostructure photodiodes possessed the higher photoresponsivity and shorter transit

time which is mainly due to the contributions of nanostructure. Finally, chapter 4 summaries the results of this dissertation.

Appendix 1 describes the ZnO based light emitting diodes by evaporating the n-ZnO on the top of p-GaN heterojunction LEDs (Light Emitting Diodes). By inserting the SiO_2 thin layer for current blocking, we could observe the 394nm near UV emission which is due to the recombination between the interfaces of n-ZnO/SiO_2 and SiO_2/p-GaN. Such simple fabrication drastically reduces the fabrication time and has the potential to manufacture the ZnO based UV emission LEDs with the low cost. Appendix 2 describes the optical characteristics of n-ZnO/p-GaN heterojunction photodetector. The obvious UV absorption peak was observed at 370nm.

*The 30 member countries of OECD are: Australia, Austria, Belgium, Canada, Czech Republic, Denmark, Finland, France, Germany, Greece, Hungary, Iceland, Ireland, Italy, Japan, Korea, Luxembourg, Mexico, the Netherlands, New Zealand, Norway, Poland, Portugal, Slovak Republic, Spain, Sweden, Switzerland, Turkey, United Kingdom, United States.

Chapter 2

Nanoparticle coated n-GZO/p-Si photodiodes with improved photoresponsivities and acceptance angles for potential solar cell applications

Si based solar cells was been demonstrated for several decades. The theoretical calculating conversion efficiency of crystalline Si solar cells is around 29% which is due to the single band absorption of crystalline Si, 1.12eV. It's possible to improve the efficiency of solar cells by enlarging the effective absorption band gap. However, we ever investigated the characterization of n-GZO/p-GaN photodetector for the application of UV detection in appendix 2. Although the lattice mismatch between GZO and Si is more serious than GaN. It is still interesting to investigate the combination of GZO and Si due to the high and low band gaps and the easy fabricating process of GZO. By depositing n-GZO on the top of p^+-Si substrate, we successfully observe the broader response spectrum than in n-GZO/p-GaN heterojunction photodiodes. We believed that device possessed broad band absorption spectrum could probably result in high solar cell conversion efficiency and will be the potential application on solar cells. Following, we sprayed the monolayer and dense arranged silica nanospheres on the surface of n-GZO/p-Si heterojunction photodiodes. By this low-cost technique, we observed the

enhanced photoresponsivity between 400 and 650nm, 17.6%, and wider acceptance angle for the devices with nanocoated silica nanospheres. The monolayer silica nanospheres played the role of 2-D grating and we utilized the diffraction theory, Littrow configuration, to explain the mechanism of wider acceptance angle in SiO_2 nanocoated photodiodes.

2-1 Motivations

In this work, n-GZO/p-Si heterojunction photodiodes are fabricated and characterized to explore the potential application to solar cells. With the availability of such heterojunction photodiodes, we coated a monolayer of silica nanoparticles on top of the device surface. The photoresponsivities of the conventional and nanoparticle coated n-GZO/p-Si heterojunction photodiodes were measured and characterized under various incident angles and wavelengths. And the increase of acceptance angle on SiO_2 nanoparticles coated devices is explained by using the diffraction theory.

2-2 Device fabrications

2-2-1 Process flows

The device structure is shown in Fig. 2-1 (a). A 300nm thick n-type GZO with a light absorption area $200\times200\mu m^2$ was patterned on top of the p-type Si (with a resistivity around $2\Omega \cdot cm$) substrate by RF magnetron sputtering at a chamber temperature 100 ^oC and oxygen pressure 15mTorr. The GZO sputter target is doped with 0.5wt% Ga, resulting in an effective n-type carrier concentration $2x10^{18}cm^{-3}$ after 550^oC 30 minutes post deposition annealing. Next, Ni/Au(12nm/120nm) and Ti/Au(12nm/ 120nm) were evaporated as the p-type and n-type contact electrodes, respectively, and were separately alloyed to achieve optimum contact conditions. The device is defined as

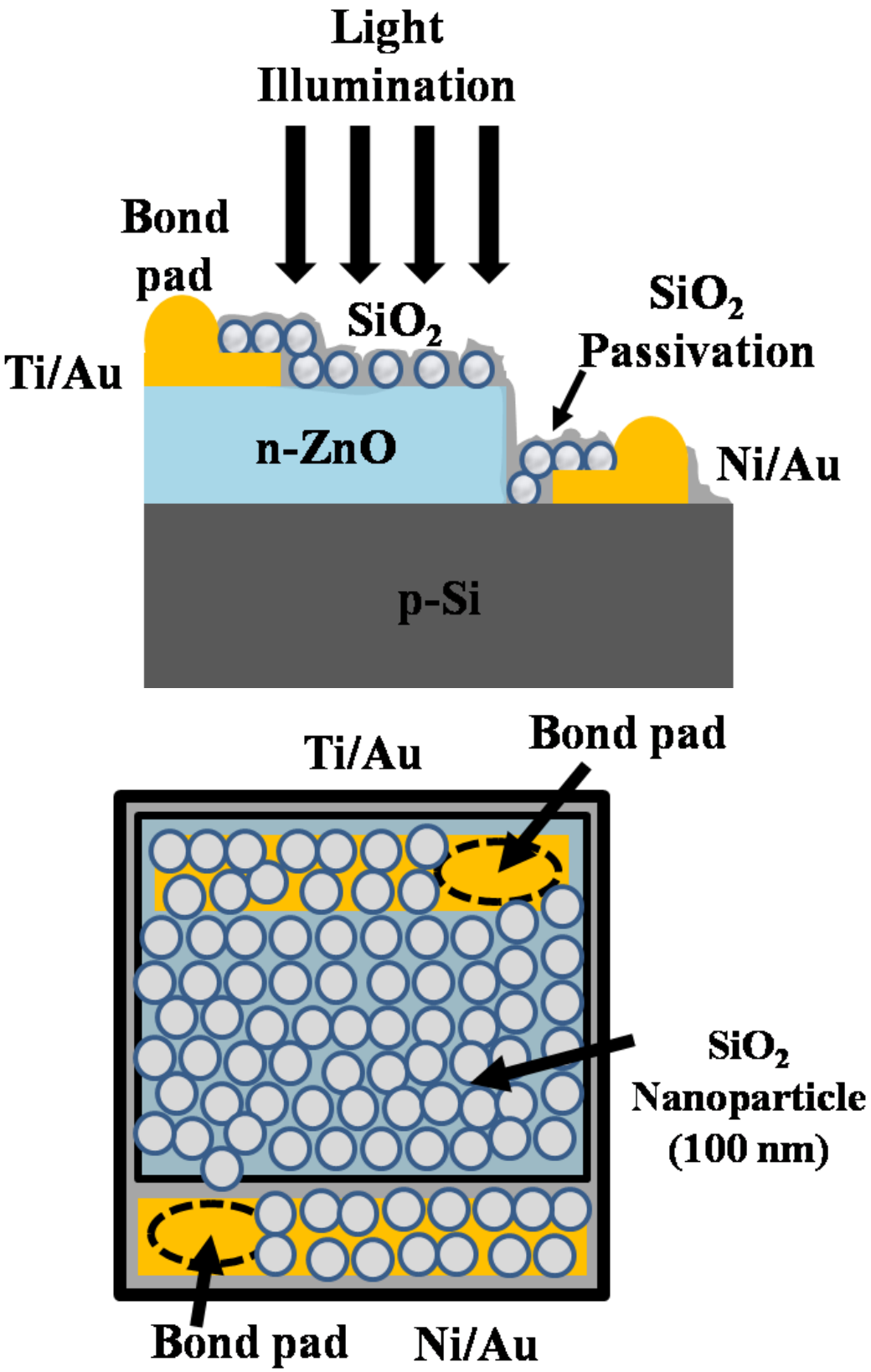

Fig. 2-1: (a)The device structure of the n-GZO/p-Si heterojunction photodiode with silica nanoparticles coated on the light illuminating surface (b) Top view of the device.

the conventional photodiode after we deposited Ti(10nm)/Au(500nm) bond pads on top of both n-type and p-type electrodes. In the following step, the solution of 100nm-diameter silica nanoparticles in IPA (Isopropyl alcohol) was spin-coated on the entire sample surface. Finally, the monolayer-nanoparticles were then sealed with a 30nm-thick SiO_2 layer using PECVD (Plasma Enhanced Chemical Vapor Deposition) with via holes open on bonding pads.

2-2-2 Photos of scanning electronic microscope (SEM)

We try to observe the morphology of device coated with SiO_2 nanoparticle from SEM photos. And, the SEM (scanning electronic microscopic) images in Fig. 2-1(c), (d) indicated that silica nanoparticle are uniform arranged on the n-ZnO layer and bonded to each other on the sample surface by the Van der Waals force [106] when the spin-speed and the solution of silica nanoparticles in IPA are properly adjusted. The uniform arranged nanoparticle could be probably applied to fabricate the 2-D grating structure on the top of device.

2-2-3 Photos of atomic force microscope (AFM)

Furthermore, we try to observe the images of atomic force microscope (AFM) to realize the information about the surface of SiO_2 nanoparticle coated device. By

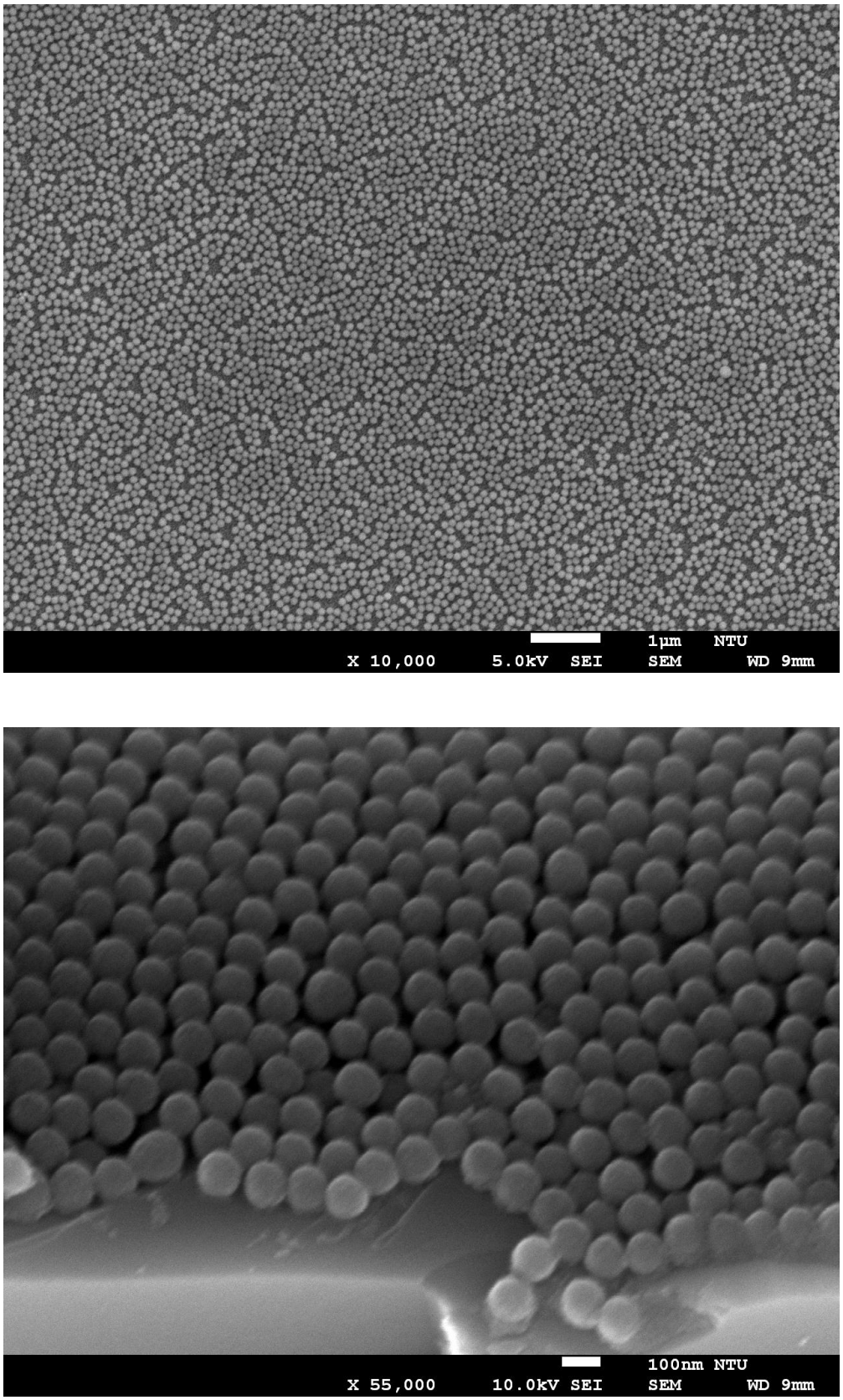

Fig. 2-1: (c) Plane view of SEM image for the monolayer silica nanoparticles on the n-GZO surface (10,000 X). (d) dense arrangement of silica nanoparticle on the n-GZO surface (55,000 X).

scanning the sample surfaces using atomic force microscopy (AFM) (see Fig. 2-2), the root-mean square (RMS) surface roughness is increased from 4.6nm of the conventional device to 8.8nm of the nanoparticle coated one. And the average peak-to-peak variation of surface profile is 31.6nm and 62.4nm for a conventional and a nanoparticle coated device, respectively. It could be expected to have better light absorption in SiO_2 nanocoated device compared to device without SiO_2 nanoparticle. However, if grating effect was existed in the SiO_2 nanoparticle coated photodiode, the device will probably possess the enhanced peak of photocurrent under certain incident angle and wavelength. The detail will be discussed in the results and discussions.

2-2-4 Contact characteristics between Ni/Au and p-Si

We evaporated the Ni/Au with the thickness of 12nm/120nm on the top of p-Si by E-beam evaporation. Following, sample was annealed under the N_2 ambient environment using rapid thermal annealing (RTA). The current-voltage diagram of Ni/Au on p-Si showed the ohmic-like behavior under the optimum annealing conditions. We could observe the lower resistivity in the annealing condition, 500^{o}C for 4mins, shown in Fig. 2-3.

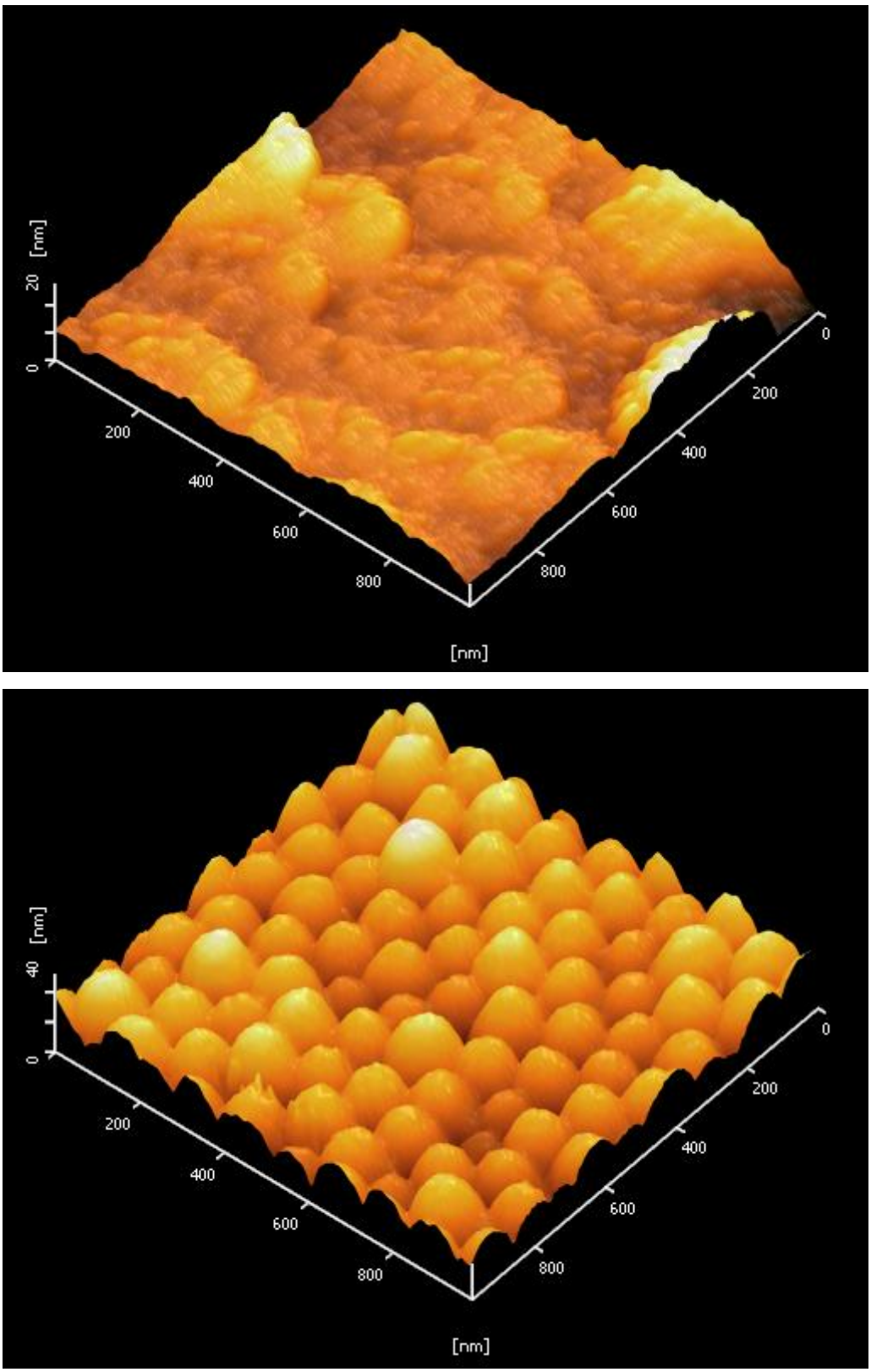

Fig. 2-2: AFM diagrams of the surface profiles for the conventional (a) and nanoparticle coated (b) n-GZO/p-Si photodiodes.

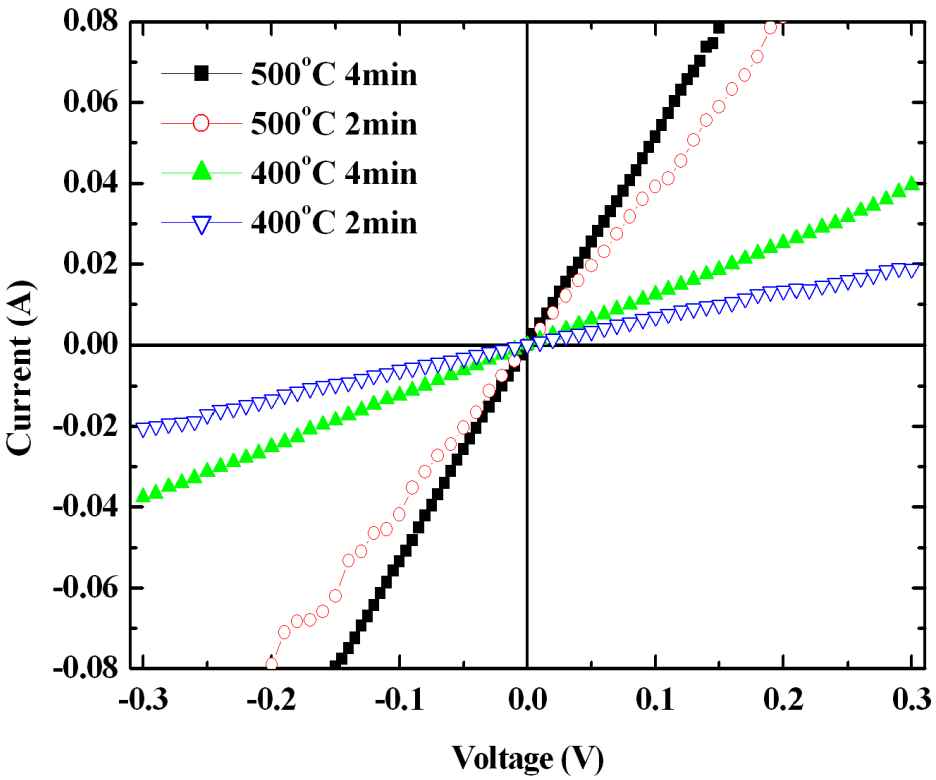

Fig. 2-3: Current-voltage curve of Ni/Au on p-Si with the different annealing conditions.

2-3 Characterizations of n-GZO/p-Si photodiodes

2-3-1 Electrical properties

The electrical properties of a conventional n-GZO/p-Si photodiode (without spraying the silica nanoparticle) are characterized using an Agilent 4155C semiconductor parameter analyzer. As shown in the insert of Fig. 2-5, the I-V curves are linear for Ti/Au contacts on n-GZO (right) and Ni/Au on p-Si (left), respectively, indicating the formation of ohmic contacts on both n- and p- layers. And from Fig. 2-4 (a), the dark current-voltage (I-V) curves indicated a nonlinear rectifying behavior with a forward/reverse current ratio 25.0 at $\pm$4V. Also, the leakage current at a bias voltage of -3V is 1.4nA (A/cm^2). In Fig. 2-4 (b), the similar reverse bias characteristic was observed and pointed out the non-damage electrical property in the silica nanoparticle coated photodiode after silica nanoparticle spraying.

2-3-2 Optical properties of n-GZO/p-Si photodiodes

A. Photoresponsivity of n-GZO/p-Si photodiodes with flat band absorption

The optical response of n-GZO/p-Si photodiodes was measured by illuminating the sample with monochromatic light from a Xenon lamp (see the setup in Fig. 2-6). The photoresponsivities of both the conventional and nanoparticle coated photodiodes were obtained by illuminating on the n-GZO side from the vertical direction. As

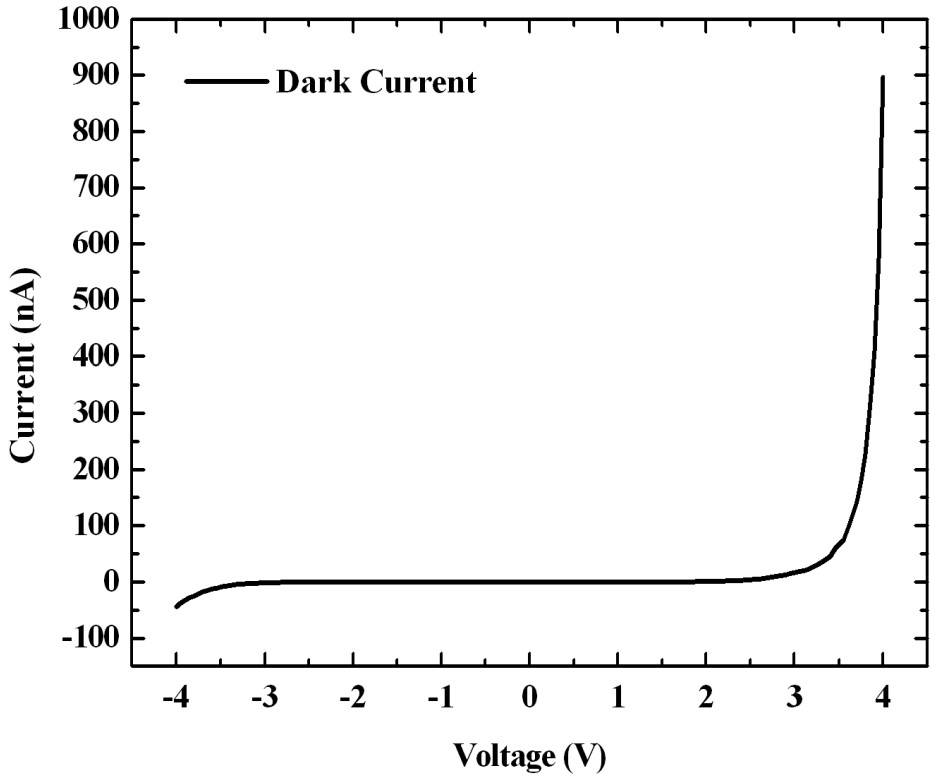

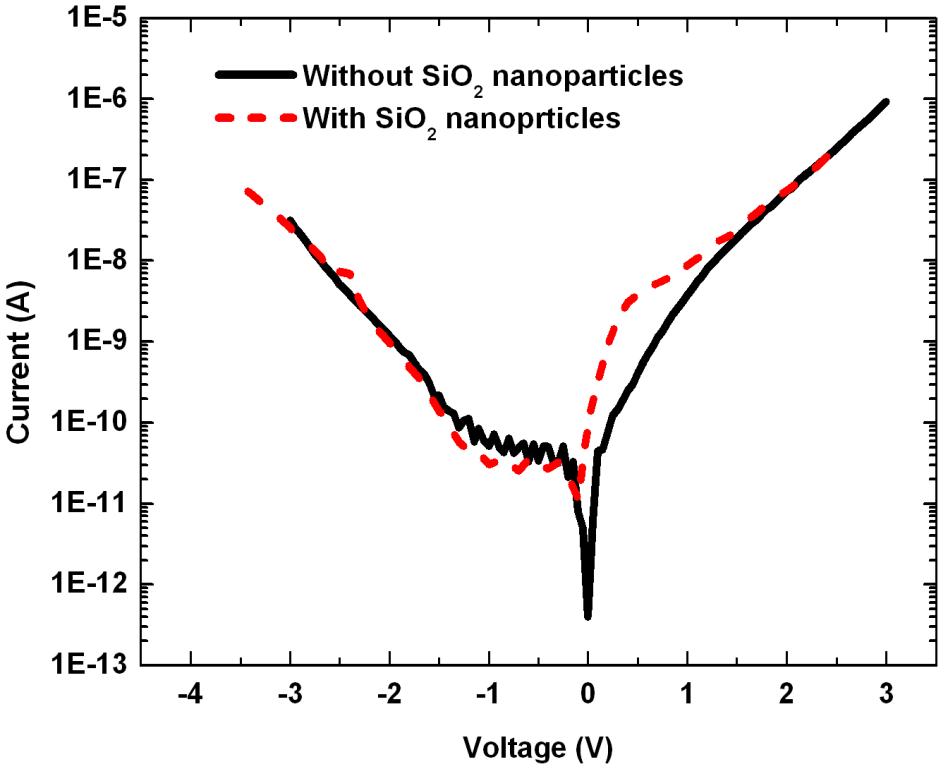

Fig. 2-4: The current-voltage curve of the n-GZO/p-Si photodiode (a). The semi-log current-voltage curve of photodiode with and without SiO_2 nanoparticles (b).

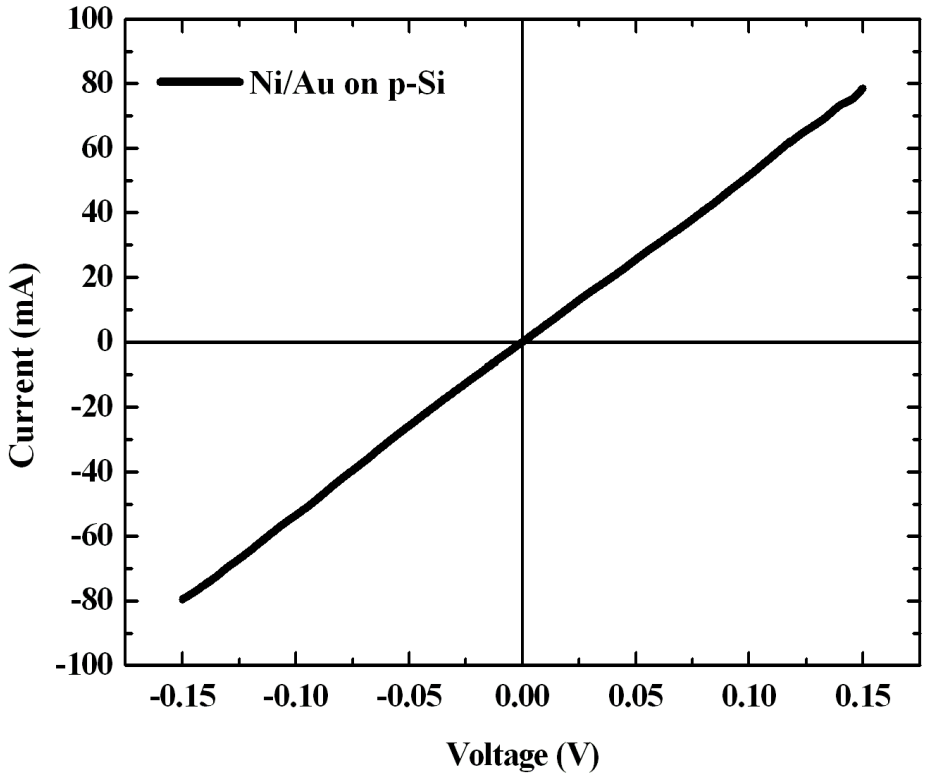

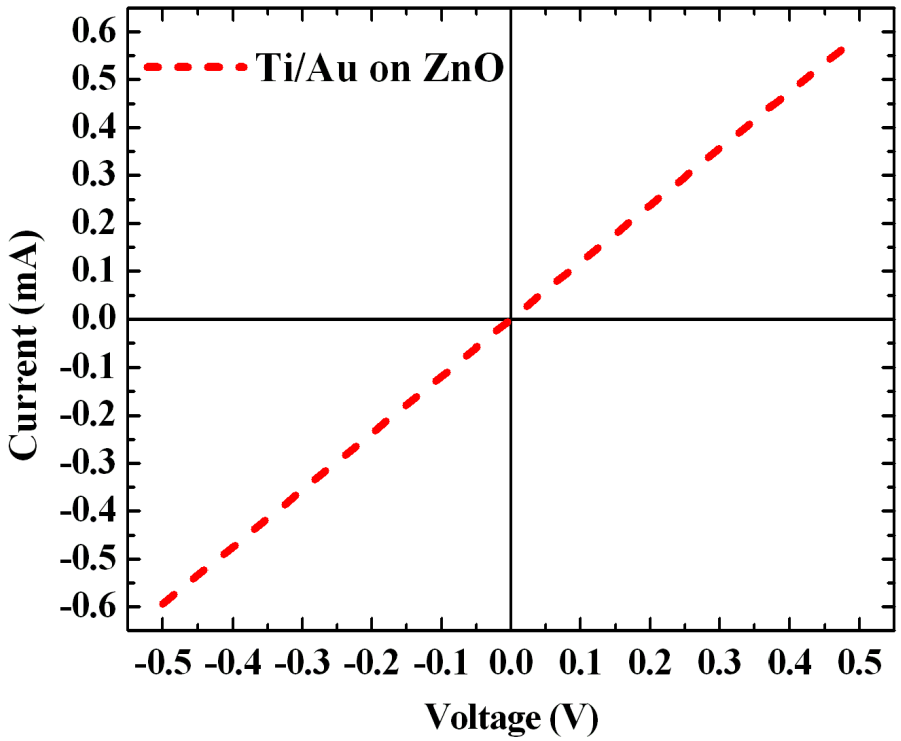

Fig. 2-5: The current-voltage curve of Ni/Au on p-Si (c) and Ti/Au on n-GZO (d). They both showed the characteristics of ohmic contact under optimum annealing condition.

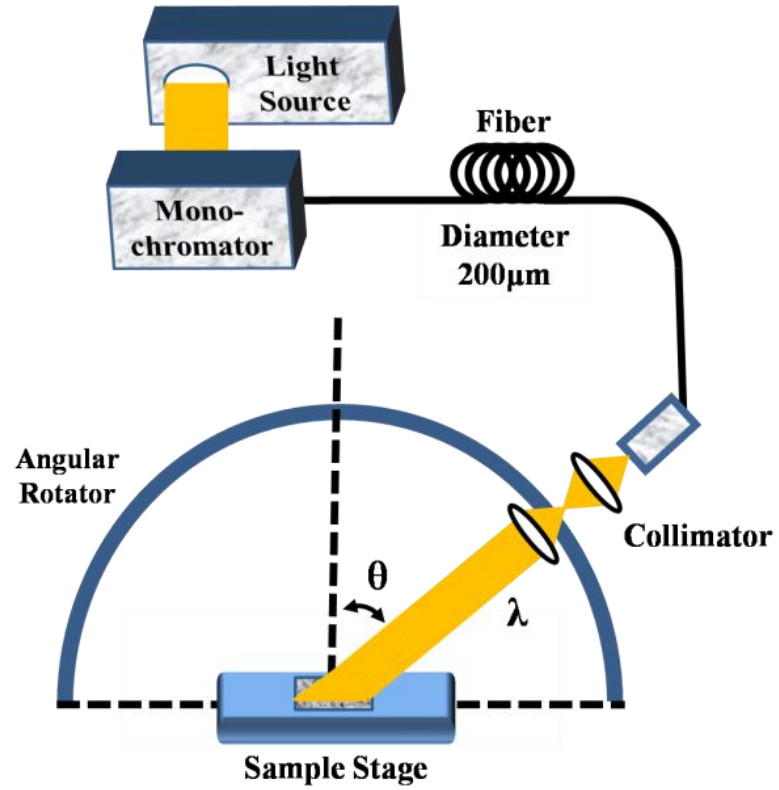

Fig. 2-6: Experimental setup for the optical response measurement of photodiodes.

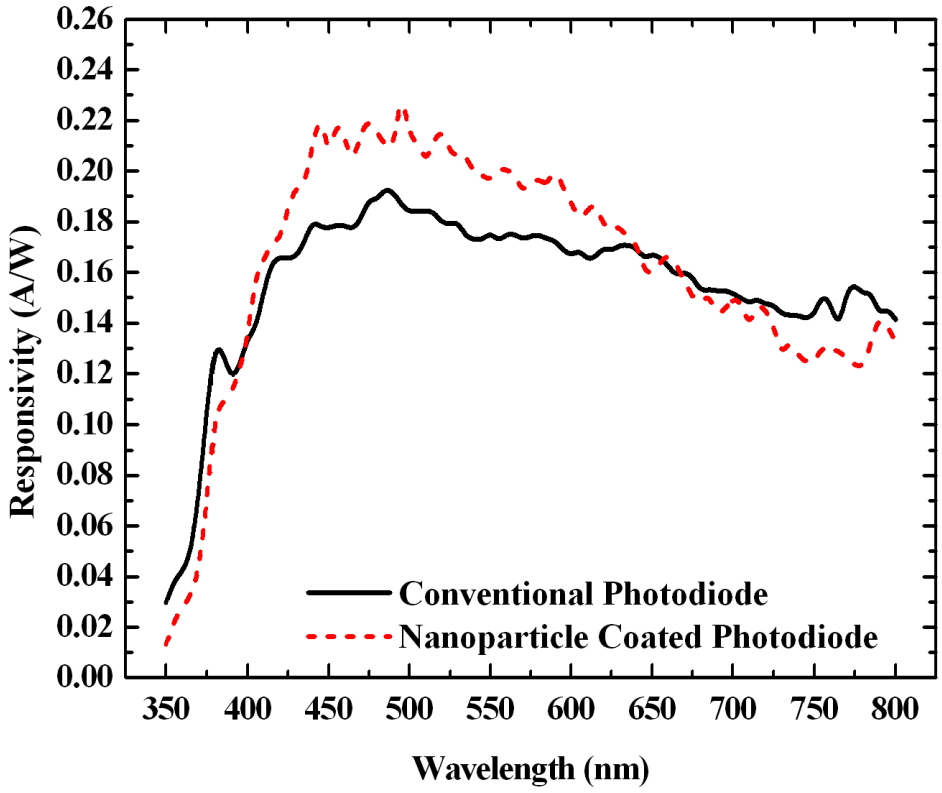

Fig. 2-7: Spectral photoresponsivities of the conventional (solid line) and nanoparticle coated (dashed line) n-GZO/p-Si photodiodes.

demonstrated in Fig. 2-7, in contrast to the decrease of spectral responsivity in typical Si photodetectors as the wavelength is shorter than 800nm [7], a relatively flat band is observed at the wavelength between 400 and 800nm with an average 0.17A/W at -3V for the conventional photodiode. The relatively flat absorption spectrum indicates a more efficient utilization of solar energy in the visible wavelength region for the n-GZO/p-Si heterojunction photodiode than that for the typical single crystal Si solar cells. The relatively flat absorption spectrum is related to the optical absorption in the n-GZO layer, as well as in the band edge between n-GZO and p-Si.

B. Enhanced photoresponsivity in SiO_2 nanoparticle coated photodiodes

As for the nanoparticle coated photodiodes, the photoresponsivity is enhanced by an average of 17.6% between 400 and 650nm. The improvement could probably be attributed to the following factors. First, the refractive index of silica nanoparticles (=1.54 at the wavelength 600nm) is in between those of n-GZO(=2.0 at the wavelength 600nm) and air, which results in the increase of light transmission toward the p-n junction. The diagram related to refractive index issue was sketched in Fig. 2-8. Second, by scanning the sample surfaces using atomic force microscopy (AFM) (see Fig. 2-2), the root-mean square (RMS) surface roughness is increased from 4.6nm of the conventional device to 8.8nm of the nanoparticle coated one. And the average

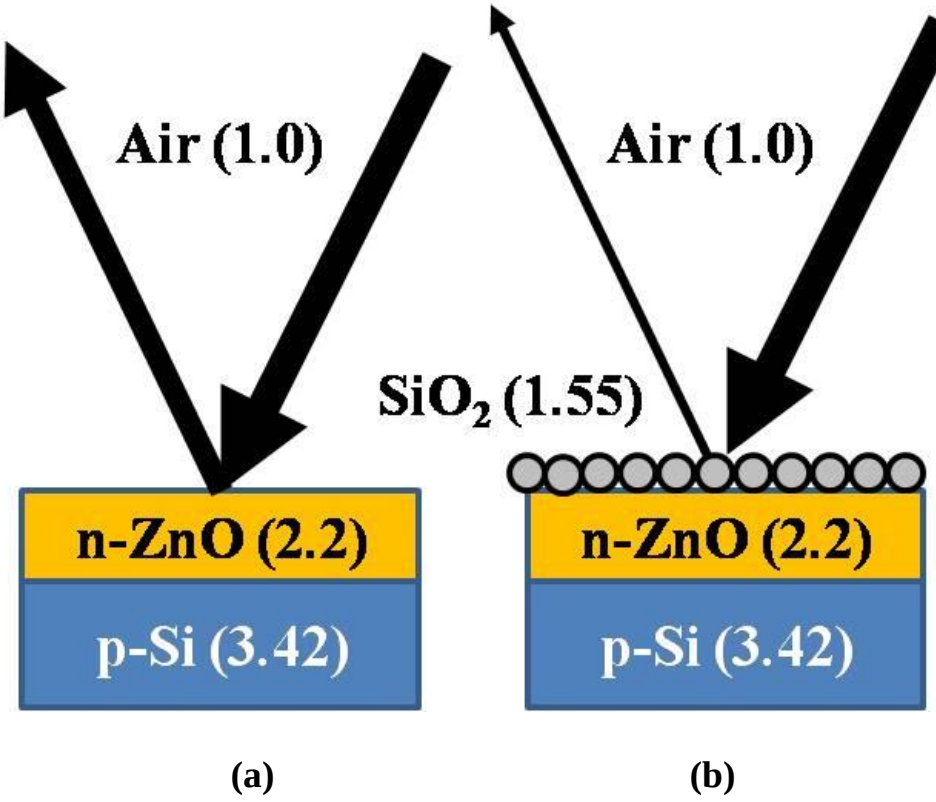

Fig. 2-8: The sketched diagram of refractive index issue between n-GZO/p-Si photodiode with (a) and without (b) SiO_2 nanoparticle coated photodiodes at the wavelength of 600nm.

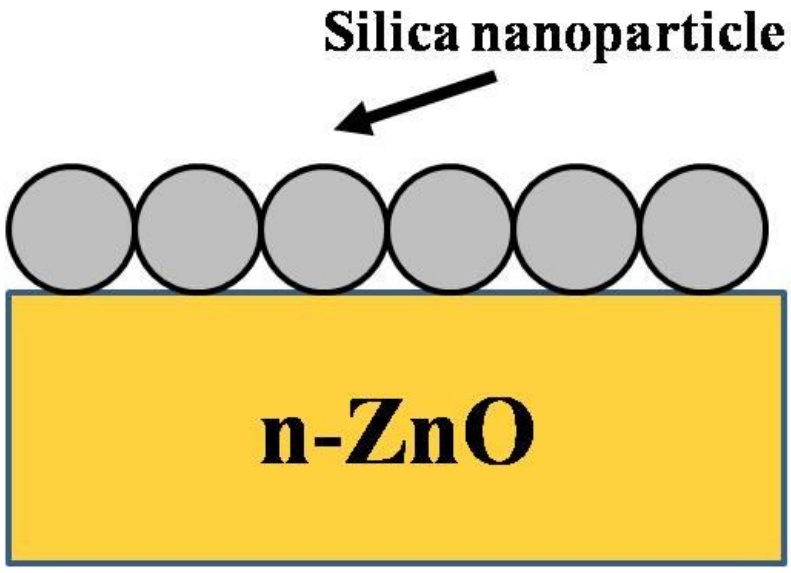

Fig. 2-9: The sketched diagram of light trapping in the interface of SiO_2 nanoparticle and air.

peak-to-peak variation of surface profile is 31.6nm and 62.4nm for a conventional and a nanoparticle coated device, respectively. As a result, photons that reach the silica nanoparticle/air interface have more chances to be trapped in the device and then converted to photocurrents and the sketched diagram was shown in Fig. 2-9. On the other hand, at a longer wavelength (>650nm) where p-Si absorption becomes more efficient, light scattering through silica nanoparticles forces the trapping of light in the n-GZO layer for a longer time, which implies light absorption in the nanoparticle coated diode is less efficient than the conventional one.

C. Wide acceptance angle

The coating of nanoparticles on the sample surface leads us to explore the possibility of increasing the acceptance angle through the application of nanoparticle. The angle-dependent photoresponsivity measurement was performed by illuminating the samples with a uniform and constant optical density at various wavelengths using the setup in Fig. 2-6. In this experiment, uniform light intensity is illuminated at a distance 50mm away from the sample. For ease of comparisons at different wavelengths, photocurrents are normalized to that of the conventional photodiode at the vertical direction (0^o). In Fig. 2-10, the normalized photocurrents of both conventional and nanoparticle coated photodiodes are plotted under different incident angles at the

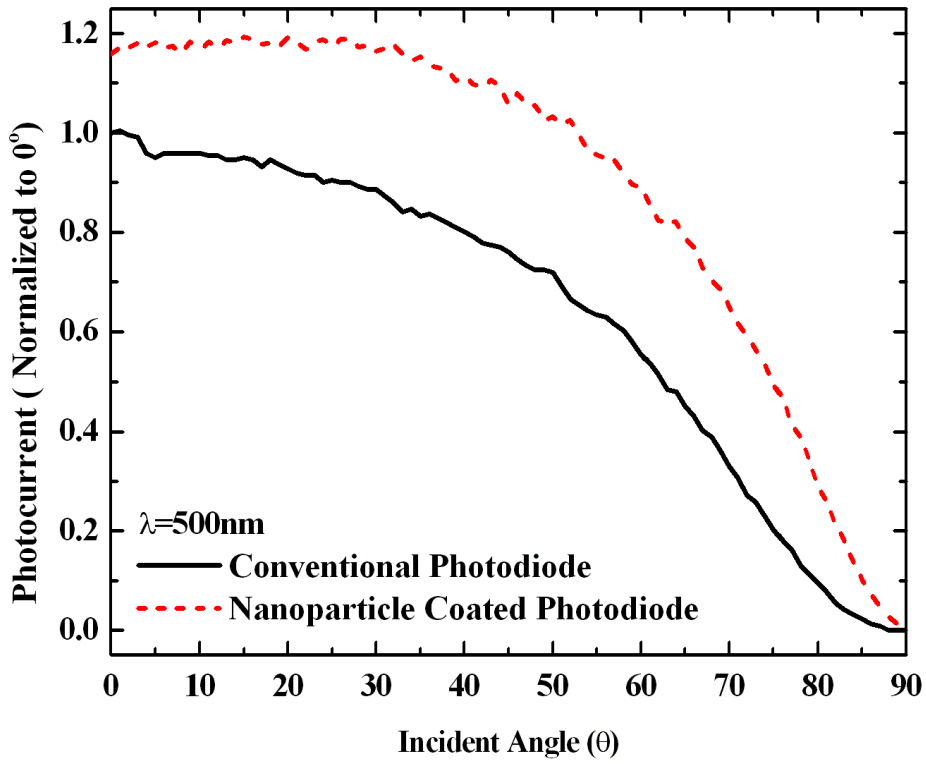

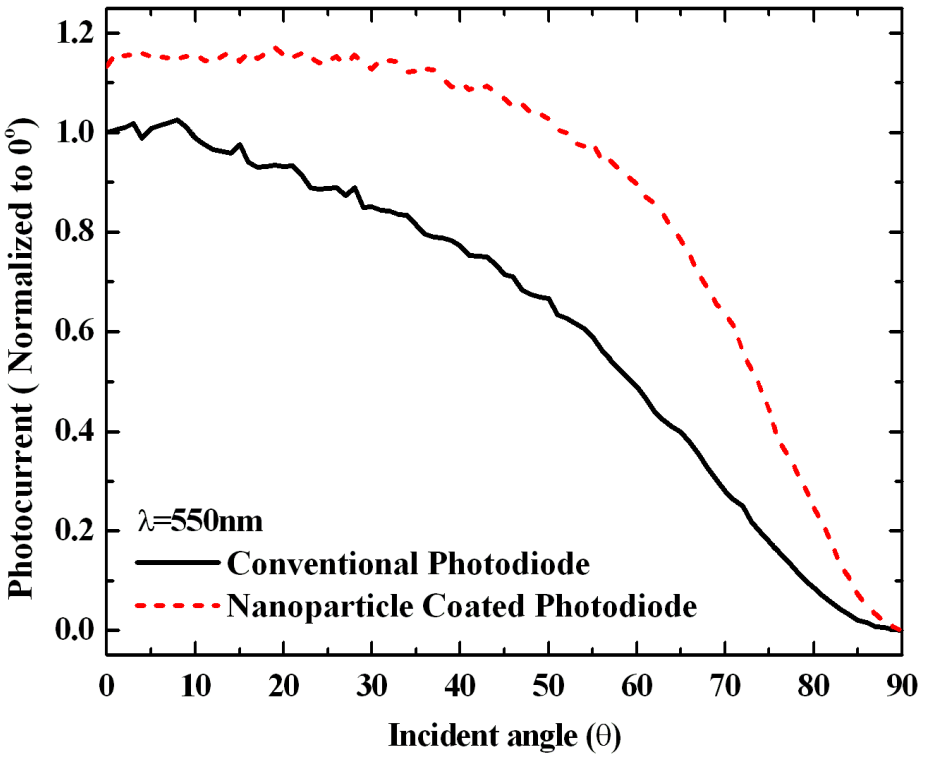

Fig. 2-10: Normalized photocurrents of both conventional and nanoparticle coated photodiodes under different incident angles at the wavelength of 500nm(a), 550nm(b). The photocurrents are normalized to the photocurrent of the conventional photodiode at 0^{o}.

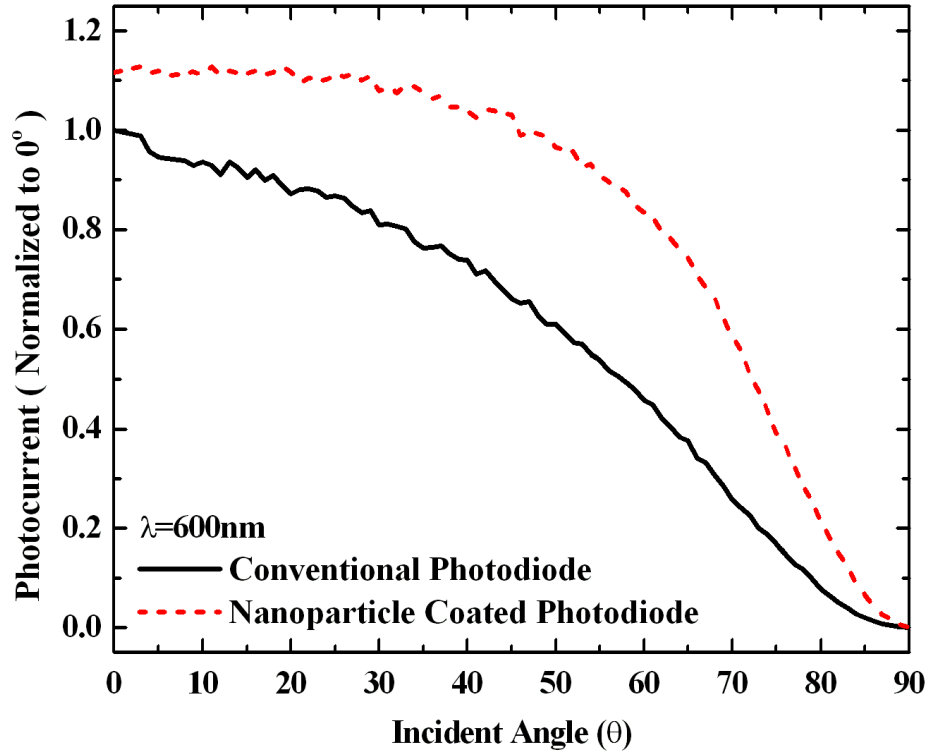

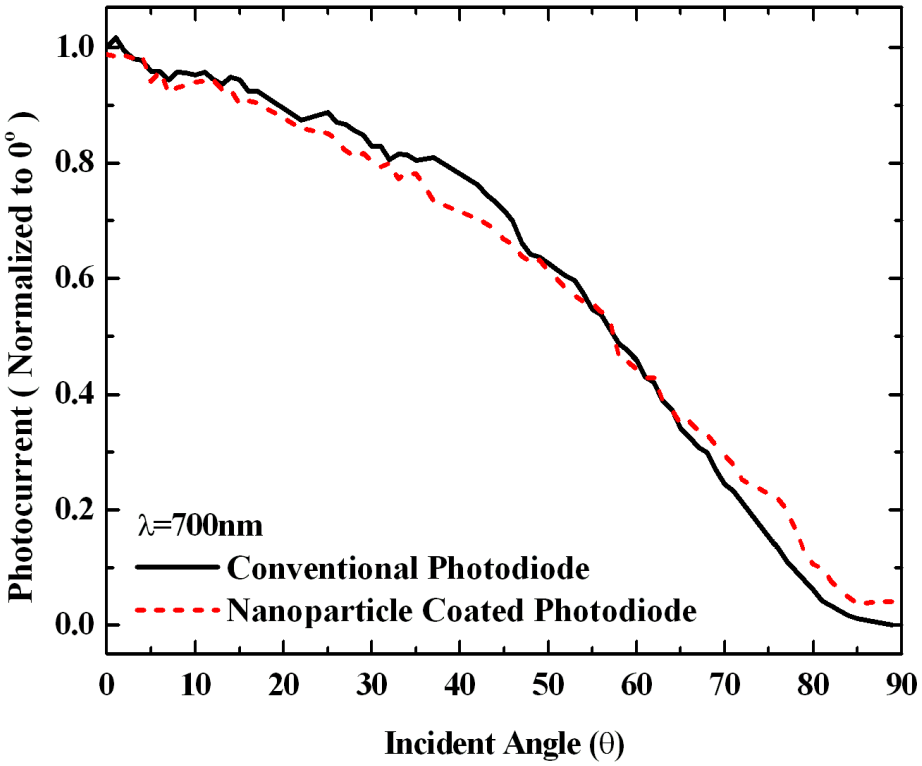

Fig. 2-10: Normalized photocurrents of both conventional and nanoparticle coated photodiodes under different incident angles at the wavelength of 600nm(c) and 700nm(d). The photocurrents are normalized to the photocurrent of the conventional photodiode at 0^{o}.

wavelength 500nm, 550nm, 600nm and 700nm. Basically, for the conventional device, photoresponsivity decays continuously as the incident angle is tilted since the effective radiative energy received by the device becomes smaller. However, for the nanoparticle coated devices, photocurrents are improved at all angles at the wavelength 500, 550 and 600nm. The acceptance angle, defined as the incident angle at 90% of the maximum light absorption, increases from 27^o to 46^o, 23^o to 50^o, and 26^o to 47^o for nanoparticle coated devices at the wavelength 500nm, 550nm and 600nm, respectively, as compared with the conventional device. However, no significant change of acceptance angle is observed at the wavelength 700nm.

D. Theoretical calculations using diffraction theory - Littrow configuration

To explain the increase of acceptance angle, the difference of normalized photo-currents between the nanoaprticle coated device and the conventional one is plotted. As demonstrated in Fig. 2-11, the enhancement reaches it maximum at the incident angle 52^o, 62^o and 63^o for the wavelength 500nm, 550nm and 600nm, respectively. If the light injection on the nanoparticles is regarded as the interaction of light with periodic arrangement (though not perfectly) of nanoparticles (see the SEM photo in Fig. 2-1(c)), the effect of Bragg diffraction can be considered to figure out light transmission to the device structure. Here, we introduce the Littrow configuration as the reference model

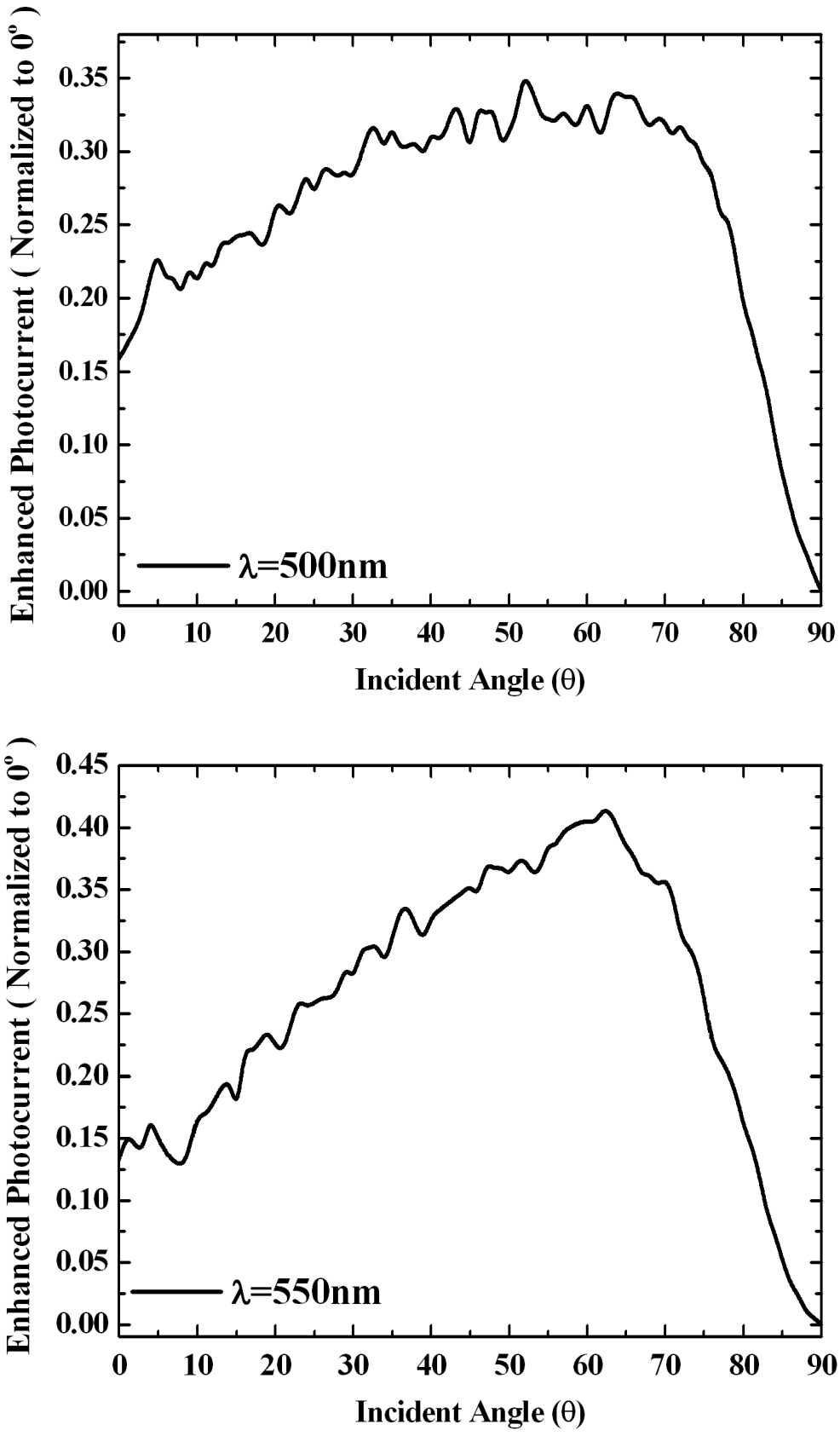

Fig. 2-11: Difference of normalized photocurrents between the nanoparticle coated and conventional photodiodes at the wavelength 500nm(a), 550nm(b).

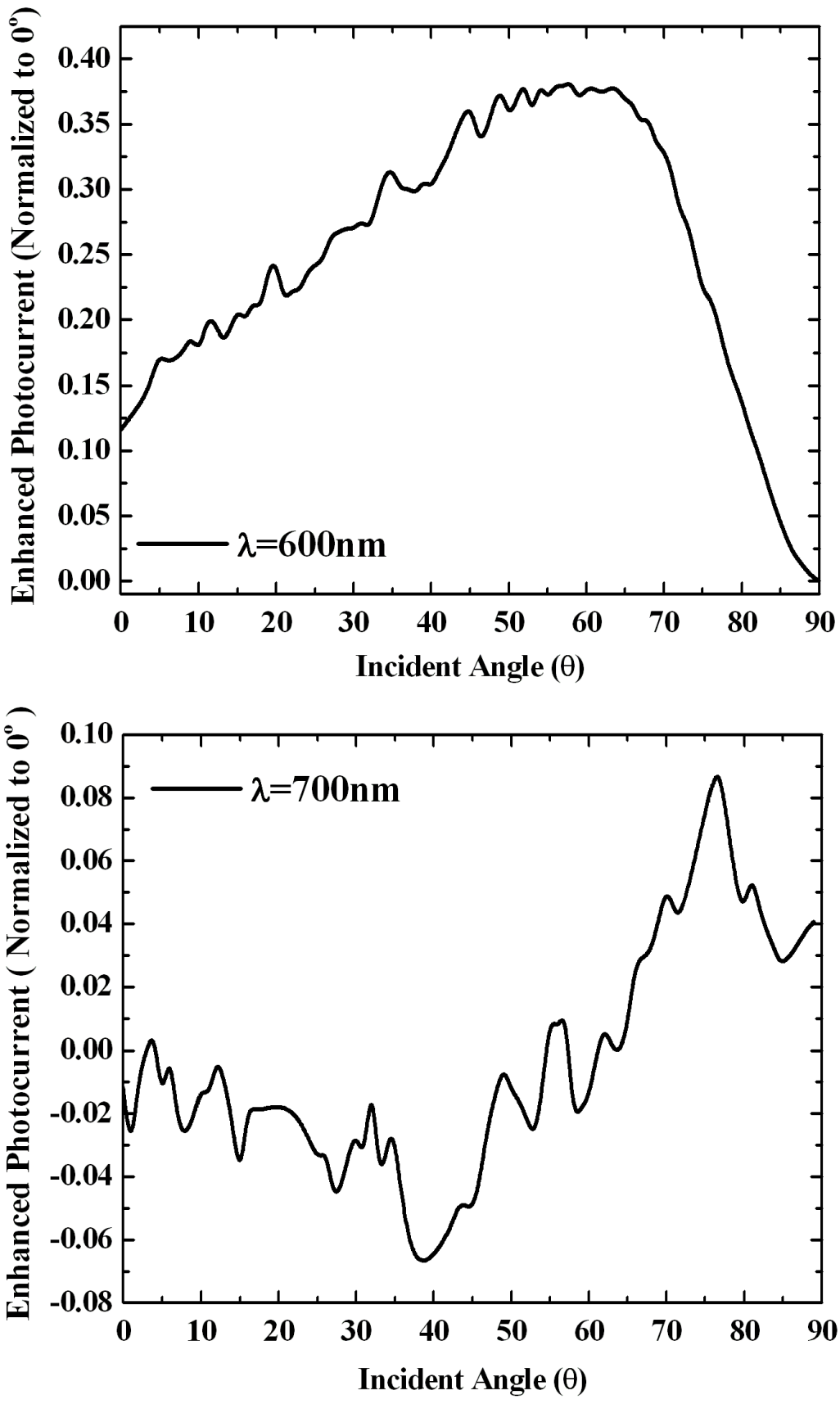

Fig. 2-11: Difference of normalized photocurrents between the nanoparticle coated and conventional photodiodes at the wavelength 600nm(c) and 700nm(d).

for our monolayer silica nanoparticels. Typically, other than the fundamental mode, we are hoping the higher order transmission mode propagates horizontally along the sample surface so as to increase the absorption length of light traveling in the photodiodes. The incident angle of maximum enhancement is obtained by considering the destructive interference of the reflected light from the silica nanoparticle grating. For such a 2-dimensional (2-D) grating composed by nanoparticles, the refraction minimum can be obtained by considering the interaction of incident wave vector with the 2-D lattice vector in ($\vec{i}$) and ($\vec{j}$) directions. However, since the projection of the incident light (at various angles) on the sample is in a 1-dimensional (1-D) path, the 2-dimensional grating is further simplified to a 1-dimensional (1-D) case following the equation

$$2\sin\theta = [2m+1)/2D_G]\lambda/n_{eff}$$

(where D_G is the effective grating period, θ is the incident angle, m is the order of diffraction, λ is the wavelength in the air, n_{eff} is the effective refractive index of the nanoparticle grating). The effective nanoparticle period D_N is obtained by considering the filling factor (F) of the monolayer silica nanoparticles. In our case, F is 0.68 and D_N is 116nm. If both the square and hexagonal nanoparticle arrangements are considered (see Fig. 2-12), the possible effective grating period D_G is D_N (for the fundamental grating period of both square and hexagonal arrangements), $\sqrt{2}D_N$ (for the second order grating period of the square arrangement) and $\sqrt{3}D_N$ (for the second order

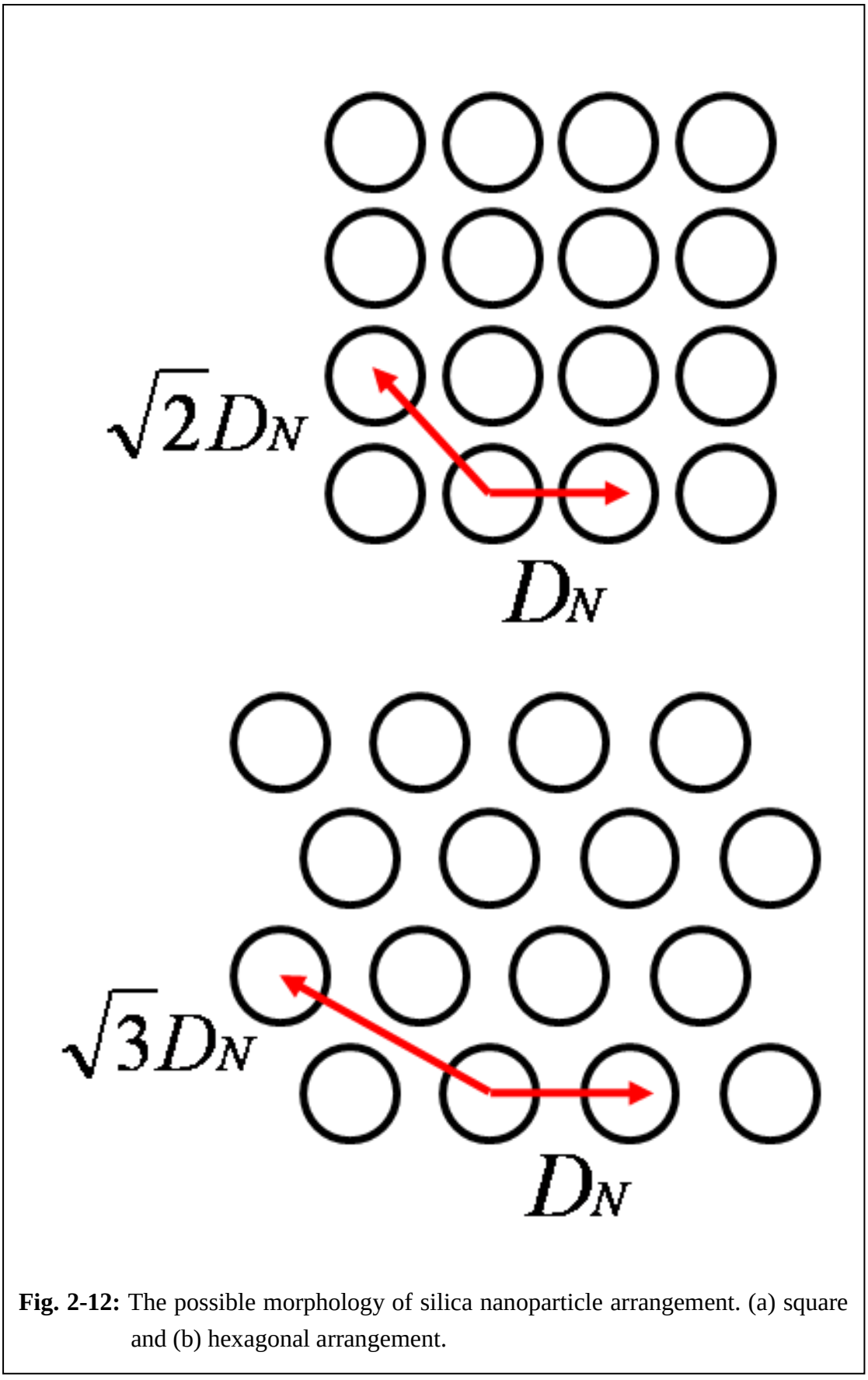

Fig. 2-12: The possible morphology of silica nanoparticle arrangement. (a) square and (b) hexagonal arrangement.

grating period of the hexagonal structure). Using the equation above, the estimated θ of the fundamental mode (DG=DN) are 48^o, 54^o and 62^o for the wavelength 500nm, 550nm and 600nm, respectively, which is comparable to the acceptance angle obtained from the experiment. The difference between the calculated and the experimental of maximum photocurrent enhancement is associated with the imperfect arrangement of nanoparticles on the sample surface. On the other hand, for the wavelength 700nm, since the light absorption is more efficient in the p-Si than in n-GZO layer, the grating induced enhancement of photoresponse and acceptance angle cannot be applied to the wavelength longer than 650nm.

2-4 Conclusions

In summary, n-GZO/p-Si heterojunction photodiodes were fabricated and characterized to explore the potential application to solar cells. With the coating of monolayer silica nanoparticles on the surface of n-GZO/p-Si photodiode, the photoresponsivity at the wavelength between 400 and 650nm is enhanced by an average of 17.6%. Furthermore, the periodic arrangement of silica nanoparticles has the advantage of increasing the acceptance angle of light illumination. The acceptance angle increases from 27^o to 46^o, 23^o to 50^o, and 26^o to 47^o for nanoparticle coated devices at the wavelength 500nm, 550nm and 600nm, respectively, as compared with the

conventional device. However, for the wavelength 700nm, since the light absorption is more efficient in the p-Si than in n-GZO layer, the grating induced enhancement of photoresponsivity and acceptance angle cannot be applied to the wavelength longer than 650nm. Our results indicate that silica nanoparticle coated n-GZO/p-Si heterojunction photodiodes have the potential of solar cell applications.

Chapter 3

Investigations of light absorption properties and acceptance angles of nanopatterned n-GZO/a-Si(i)/p^+-Si photodiodes

In chapter 2, we successfully fabricated the n-GZO/p-Si heterostructure photodiodes with the technique of silica nanoparticles spraying on the surface of photodiodes. By using this technique, the photoresponsivity and acceptance angle could be improved in nanopatterned photodiodes compared to those in conventional photodiodes. Nanostructure photodiodes have several advantages such as lower surface reflectance and shorter effective transit paths for carrier transportation compared to planar photodiodes. From this concept, we utilized the technique of silica nanoparticles spraying to fabricate nanostructure photodiodes. Furthermore, the combinations of n-GZO and p-Si showed the flat and broad band absorption spectrum. The concept of broad band absorption could be realized in the combinations of high and low band gap materials, such as tandem structure solar cells and graded band gap solar cells. From above considerations, we try to combine materials of n-GZO, a-Si (i) and p^+-Si to fabricate the broad band absorption photodiodes for the application of solar cells. However, nanostructure devices also were fabricated by using the nanosphere lithography for comparisons on photoresponsivity and acceptance angle. The

enhancement of photoresponsivity could achieve 36.2%. And, the acceptance angle is also improved at all wavelength. Finally, we try to investigate the relationships between photoresponsivity, relaxation time and device structure to realize the advantages of nanostructure not just only reducing the reflectance of device but also reducing the transit time for carrier transporting to contact electrodes.

3-1 Motivations

In this work, we fabricated n-GZO(ZnO doped with Ga) /a(amophous)-Si(i) (i:intrinsic)/p^+-Si photodiodes. By employing a natural lithography technology, either the a-Si(i) or p^+-Si was textured with a period in the range around 100-200nm. We compare the photoresponsivity of 4 samples with and without the a-Si(i) layer and surface texturing. In order to understand the effect of sub-wavelength texturing on the acceptance angle, the light absorption at different incident angles was also conducted.

3-2 Device fabrications

3-2-1 Fabrications of nanopatterned structure

A. Etching morphology on different nanosphere concentrations

Silica nanosphere lithography was used to fabricate the nanopatterned structure of device. The detail process of nanosphere spraying was described in chapter 2. By modifying the optimum parameter of spraying nanosphere, the arrangement of SiO_2 nanosphere was uniform on the top of p^+-Si substrate. Fig. 3-1 showed the uniform and large area SEM diagram for p^+-Si substrate with spraying the 100nm diameter SiO_2 nanosphere on the surface. After the optimum condition of spraying nanosphere, reactive ion etching (RIE) was used to fabricate the nanopatterns of p^+-Si. In Fig. 3-2 and Fig. 3-3, the plane-view SEM photos showed two kinds of arrangements for the

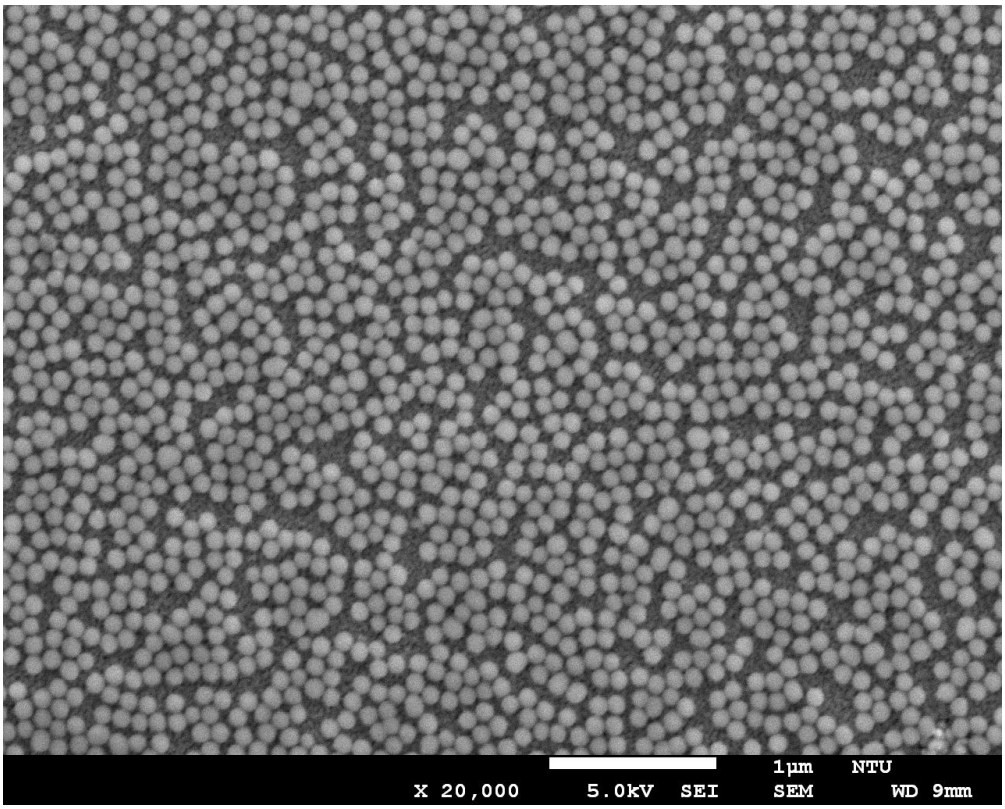

Fig. 3-1: The plane-view SEM diagram of silica nanosphere with 100nm diameter spraying on the p^+-Si substrate.

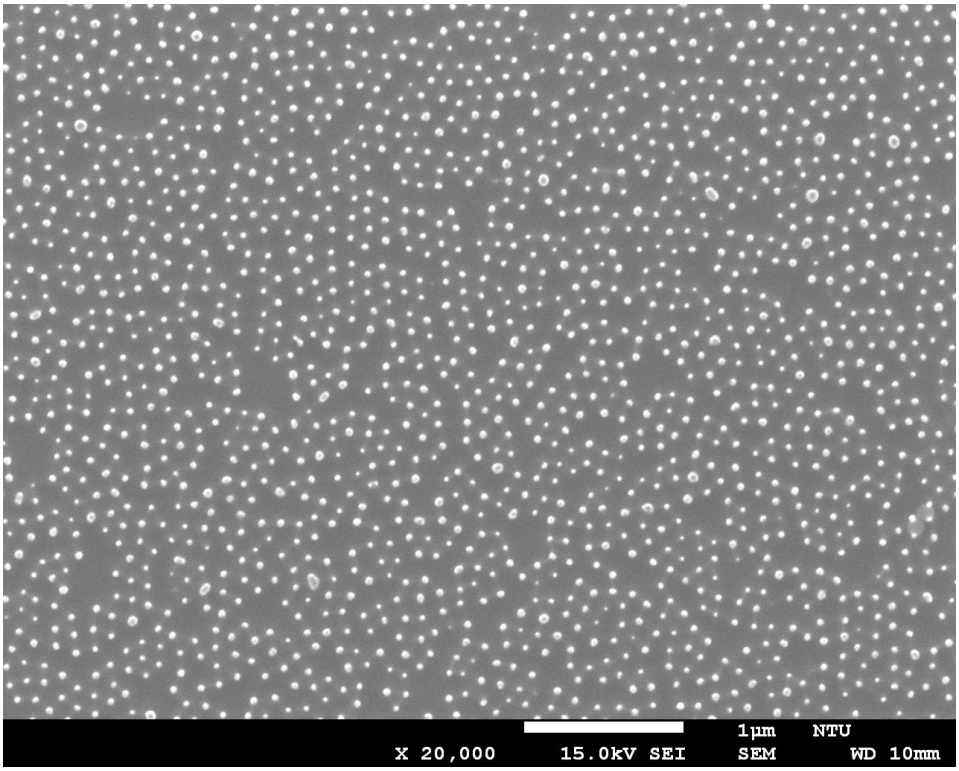

Fig. 3-2: The plane-view SEM images (20,000X) showed the dense arrangement of surface morphology on the p^+-Si substrate after RIE dry etching.

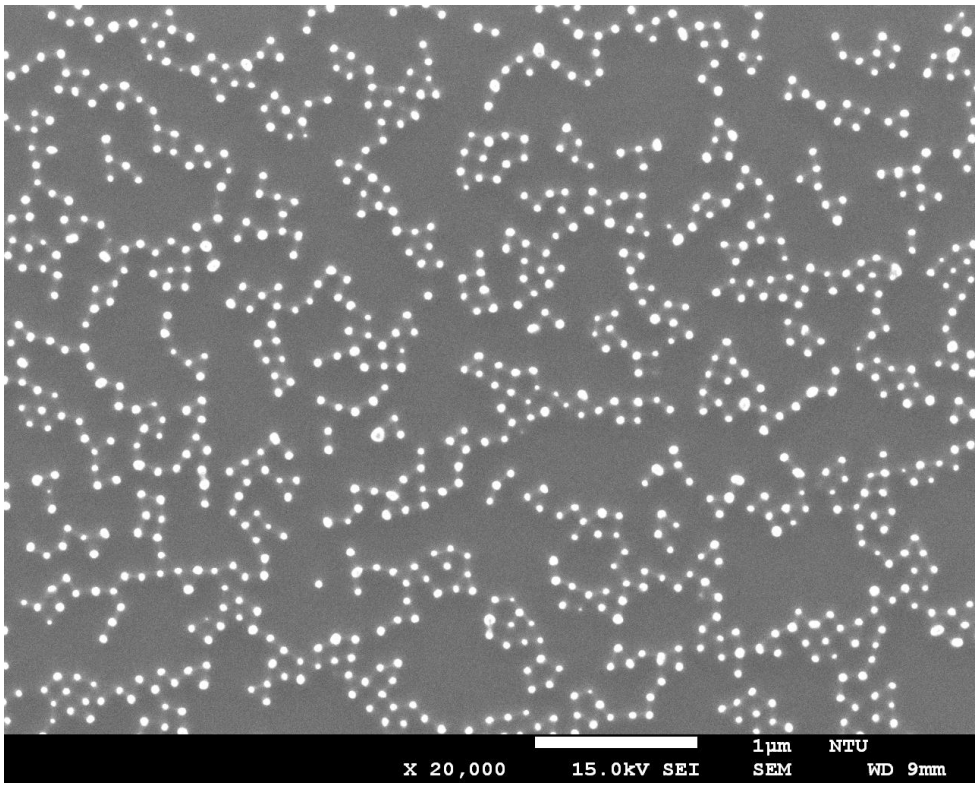

Fig. 3-3: The plane-view SEM images (20,000X) showed the sparse arrangement of surface morphology on the p^+-Si substrate after RIE dry etching.

Table of Reactive Ion Etching (RIE) Dry Etching Parameter

Codes	SF6	CHF3	CF4	O2	Pressure	Power	Etching Rate
A	25ccm	0	0	0	1.3pa	120W	60nm/mins
B	0	0	16ccm	6ccm	4pa	50W	25nm/mins

Table 3-1: The table listed the detail information of RIE dry etching receipt for nanopatterned fabrication on devices.

etching test of nanopatterned p^+-Si, dense and sparse conditions, after RIE dry etching. For the purpose of fabricating the nanostructure p-i-n photodiodes, we choose the dense-arranged nanostructure as our requirement.

B. Etching morphology on different etching receipts of nanopatterned structure

We used two kinds of etching receipts to fabricate nanopatterned p^+-Si. The detail etching parameters were listed in Table 3-1. In the receipt A, we observed the pyramid structure p^+-Si, in Fig. 3-4, with 80nm height after RIE dry etching. Following, we used the receipt B to etch p^+-Si substrate covering nanosphere. The SEM photo, in Fig. 3-5, showed the nanorod structure of p^+-Si with 50nm diameter and 70nm height after the RIE dry etching. Two kinds of etching receipts result in the different morphology of nanopatterned p^+-Si as pyramid and nanorod. It indicated that receipt B possessing the better ability of anisotropic etching for p^+-Si. The nanorod structure could resulted in the much lower reflectivity compared to planar structure. This characteristic could result in the enhancement of light absorption.

C. Morphology of nanopatterned p^+-Si before and after a-Si(i) deposition

In Fig. 3-6, the plane-view SEM photo showed the diameter of p^+-Si nanorod around 60nm after RIE dry etching. Following, we deposited a thin intrinsic a-Si layer

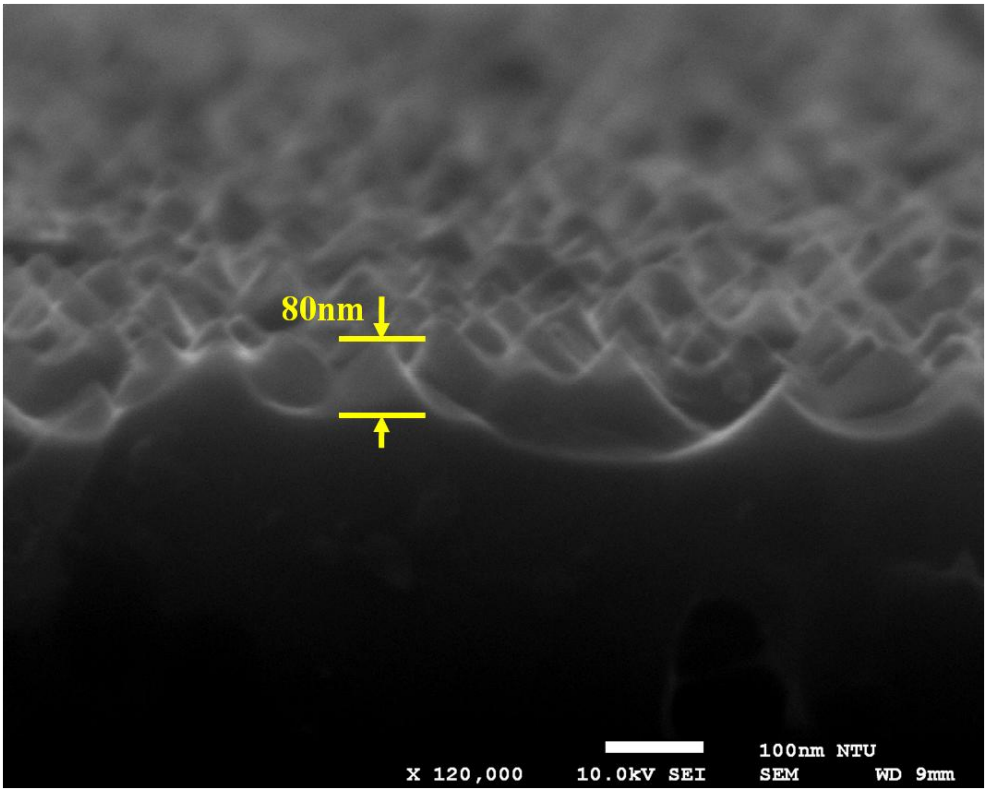

Fig. 3-4: The cross-section SEM diagram showed the nano-pyramid surface morphology under the receipt A in Table 3-1 for RIE dry etching.

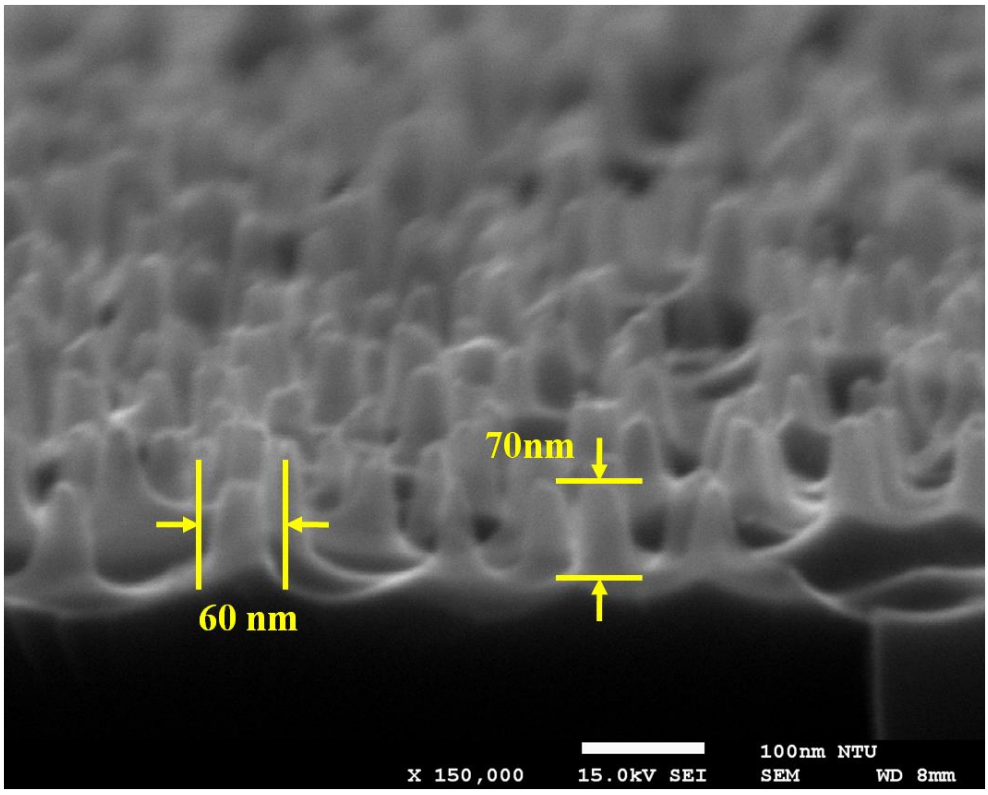

Fig. 3-5: The cross-section SEM diagram showed the nanorod surface morphology under the receipt B in Table 3-1 for RIE dry etching.

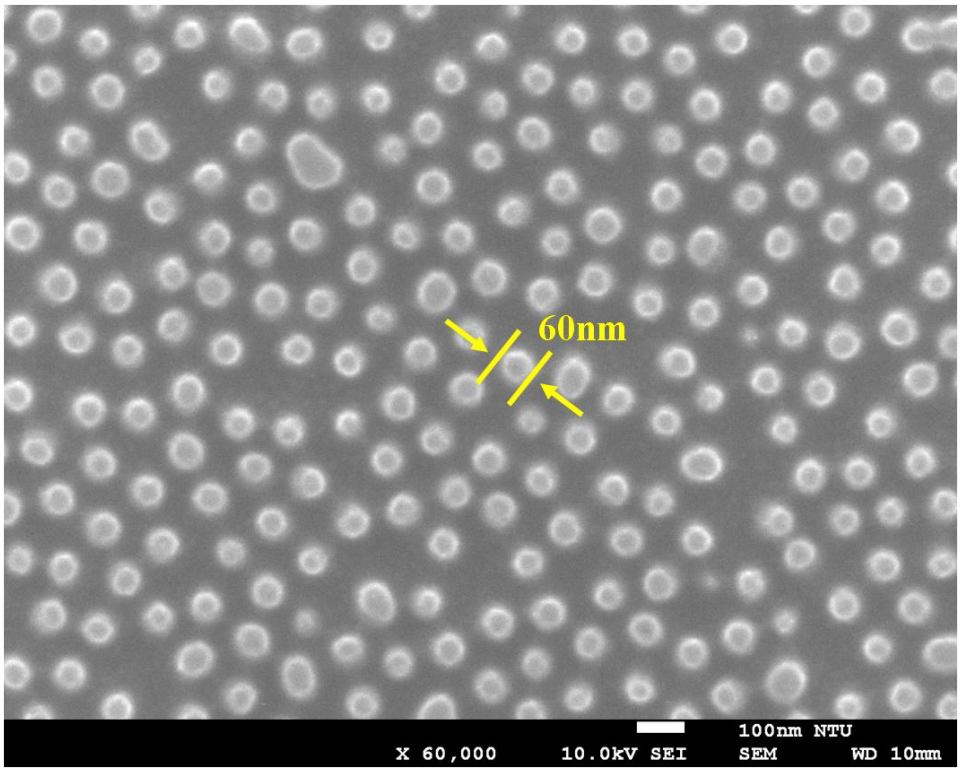

Fig. 3-6: The plane-view SEM images (60,000X) showed the surface morphology of nanopatterned p^+-Si substrate before a-Si(i) thin film deposition on nanopatterned p^+-Si substrate.

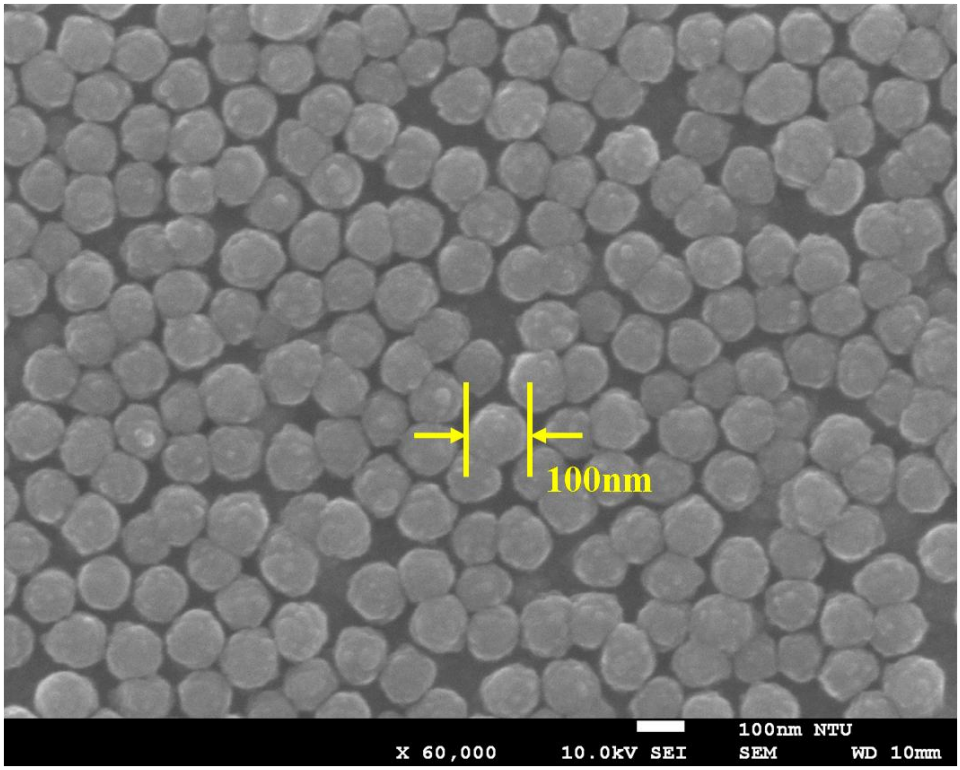

Fig. 3-7: The plane-view SEM images (60,000X) showed the surface morphology of nanopatterned p^+-Si substrate after a-Si(i) thin film deposition on nanopatterned p^+-Si substrate.

on the nanopatterned p^+-Si. The size of nanorod was enlarged to 100nm in diameter which is due to the uniform deposition of intrinsic a-Si thin layer by high density plasma chemical vapor deposition (HDP-CVD). The SEM photo was shown in Fig. 3-7. In order to investigate the surface morphology, we take the cross-section SEM diagrams. From the Fig. 3-8, the cross-section diagram of SEM showed the nanocorn morphology after we deposited the intrinsic a-Si layer on the nanopatterned p^+-Si. The nanocorn structure could play an important role in the absorption of wide incident angle. It will be one important factor in the fabrication of nanostructure photodiodes.

D. Morphology of nanopatterned a-Si before and after RIE dry etching

We applied the same receipt of RIE dry etching on the intrinsic a-Si due to the similar material, Si. However, we still observe the different etching morphology between p^+-Si and intrinsic a-Si. In Fig. 3-9, The size of nanopatterned a-Si is around 80nm which is larger than the nanopatterned p^+-Si. This difference could be originated from the inaccuracy of RIE dry etching. We could observe the nanopatterned a-Si with the 80nm in diameter, 50nm height and around 80nm periodicity. In Fig. 3-10, we didn't etch the a-Si layer to p^+-Si substrate and keep around 70nm thickness intrinsic a-Si to keep the ability of visible band absorption. From the above process of nanosphere lithography, the nanostructure n-GZO/a-Si(i)/p^+-Si photodiodes could be fabricated.

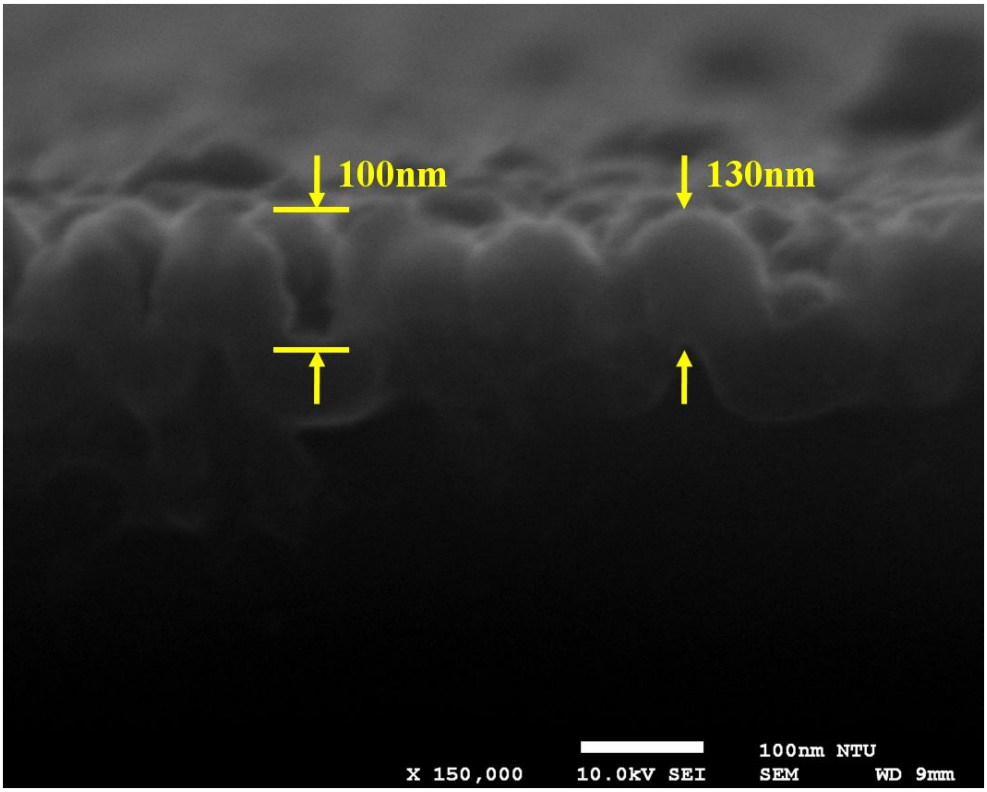

Fig. 3-8: The cross-section diagram of SEM showed the nanocone morphology in the nanopatterned p^+-Si after the a-Si(i) deposition by HDP-CVD. The a-Si(i) thin film showed the uniform surface morphology.

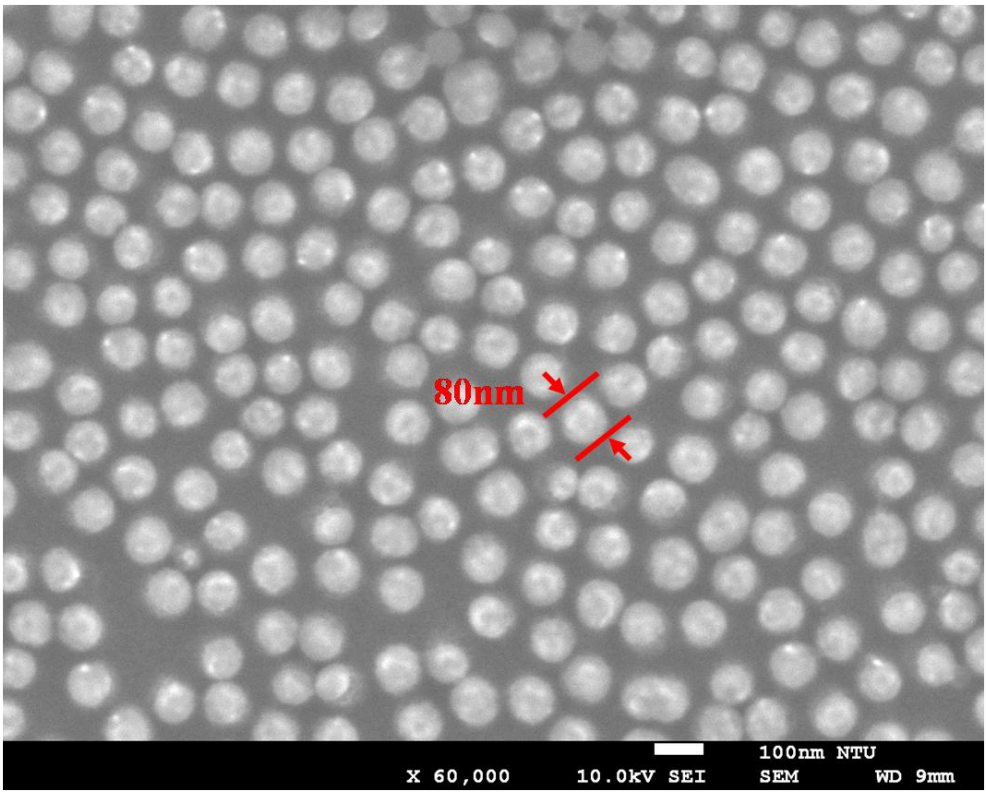

Fig. 3-9: The plane-view diagram of SEM showed the uniform arrangement of nanopatterned a-Si(i) with 100nm diameter after RIE dry etching.

Finally, we listed the Table 3-2 for the obvious record in our nanosphere lithography.

3-2-2 Fabrication process

A. Process flows

The n-GZO/p^+-Si photodiodes were mainly realized by stacking n-type GZO on the top of the p^+-type Si substrate. To investigate the effect of texturing on light absorption either the intrinsic a-Si or the p^+-Si substrate were patterned in the nanoscale. The comparisons of device structure in this work are sketched in Fig. 3-11. Devices A, B, C and D represent the planar n-GZO/p^+-Si, planar n-GZO/a-Si(i)/p^+-Si, n-GZO/nanopatterned a-Si(i)/p^+-Si and n-GZO/a-Si(i)/nanopatterned p^+-Si, respectively. For devices B, C and D, the 130 nm thick a-Si(i) layers were deposited on the p^+-Si by HDP-CVD (High Density Plasma Chemical Vapor Deposition). And the n-GZO layers for all four samples were deposited by RF magnetron sputtering using a ZnO target doped with 3wt% Ga. The n-GZO layer is 200 nm in thickness with a doping density 2×10^{20} cm^{-3} after annealing at 400^oC for 30 minutes. For devices C and D, the nanopatterns were realized by using the nanosphere lithography. We first spin-coated a monolayer silica nanoparticles, which are resolved in the IPA (isopropyl alcohol) solvent, on the sample and followed by RIE (reactive ion etching) to define the nanopatterns. The silica nanoparticles with a diameter 100 nm±10 nm act as a hard

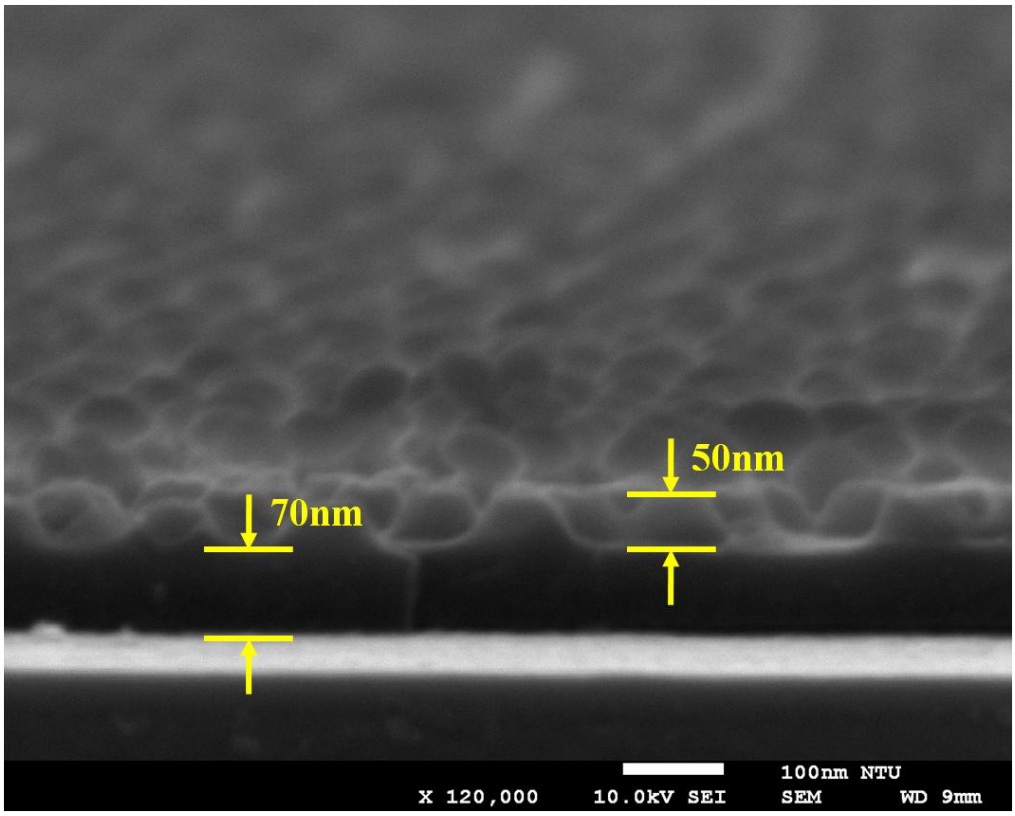

Fig. 3-10: The cross-section SEM diagram of nanorod a-Si(i) with 50nm height. The thickness of un-etching a-Si thin film is around 70nm.

The Parameter Lists of Nanosphere Lithography

	RIE		HDP-CVD	
	On p^+-Si	On a-Si(i)	On p^+-Si	On a-Si(i)
Height	**70nm**	**50nm**	**100nm**	**X**
Diameter	**60nm**	**80nm**	**100nm**	**X**
Periodicity	**140nm**	**80nm**	**140nm**	**X**

Table 3-2: The nanopatterned size of p^+-Si and a-Si(i) after reactive ion etching (RIE) dry etching and the a-Si(i) thin film deposited by High Density Plasma Chemical Vapor Deposition (HDP-CVD) The RIE process was performed by Samco RIE-10NR.

mask during the pattern definition. And the etching depth is around 70 nm.

B. SEM photos of nanopatterned p+-Si before and after deposition of a-Si layer

In the section of 3-2-1, we have clearly discussed the process flow of nanostructure. The corresponding SEM (scanning electron microscopic) images of the nanopatterns on the p^+-Si and a-Si(i) thin film on nanopatterned p^+-Si substrate are demonstrated in Fig. 3-12(a) and (b), respectively. The space between two nano-structure was calculated from the top view of the SEM photos, is around 100 nm~200 nm, with an average 144.55 nm by assuming a triangular arrangement of nanoparticles.

C. Characterizations of metal contact

The characteristic of contact electrodes played an important role on the electron and hole transportation in the interface between metal and semiconductor. For the purposes of lower loss in the interface of contact electrode and semiconductor, Contact tests were performed under different annealing temperature and time. Table 3-4 showed the detail records on annealing tests. In Fig. 3-13(a), the schottky behavior was observed under 350^{o}C annealing temperature at the annealing time of 1, 3 and 5mins. It indicated the schottky barrier existed between Al and p^+-Si and it will cause the serious energy loss. The better contact characteristic was observed in Fig. 3-13(b). We choose the condition

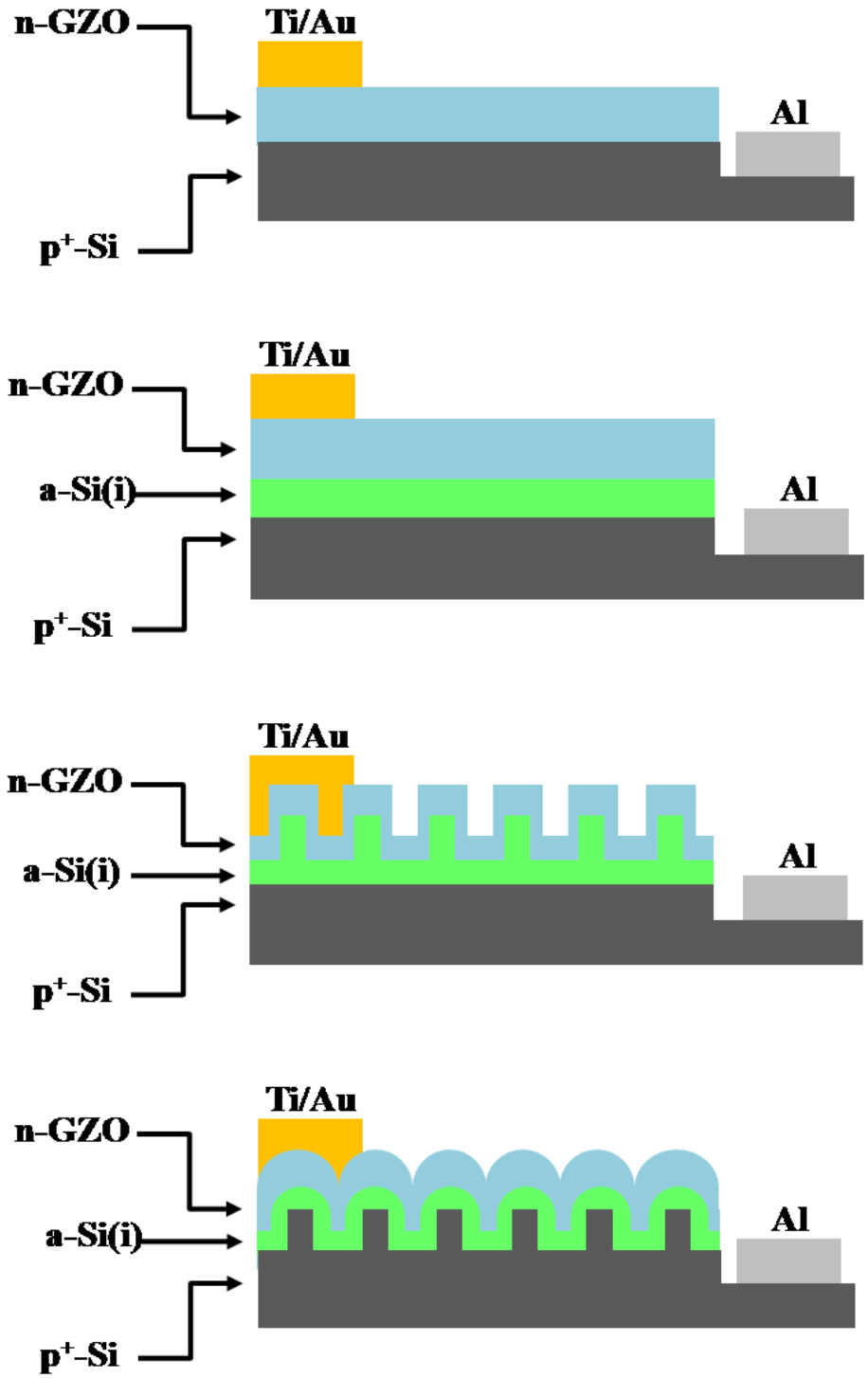

Fig. 3-11: Device structures of (a) planar n-GZO/p^+-Si (device A), (b) planar n-GZO/a-Si(i)/p^+-Si (device B), (c) n-GZO/nanopatterned a-Si(i)/p^+-Si (device C) and (d) n-GZO/a-Si(i)/nanopatterned p^+-Si (device D).

Device Name	Device Structure
A	n-GZO/p^+-Si
B	n-GZO/a-Si(i)/p^+-Si
C	n-GZO/nanopatterned a-Si(i)/p^+-Si
D	n-GZO/a-Si(i)/nanopatterned p^+-Si

Table 3-3: The name lists of heterojunction photodiodes A, B, C and D

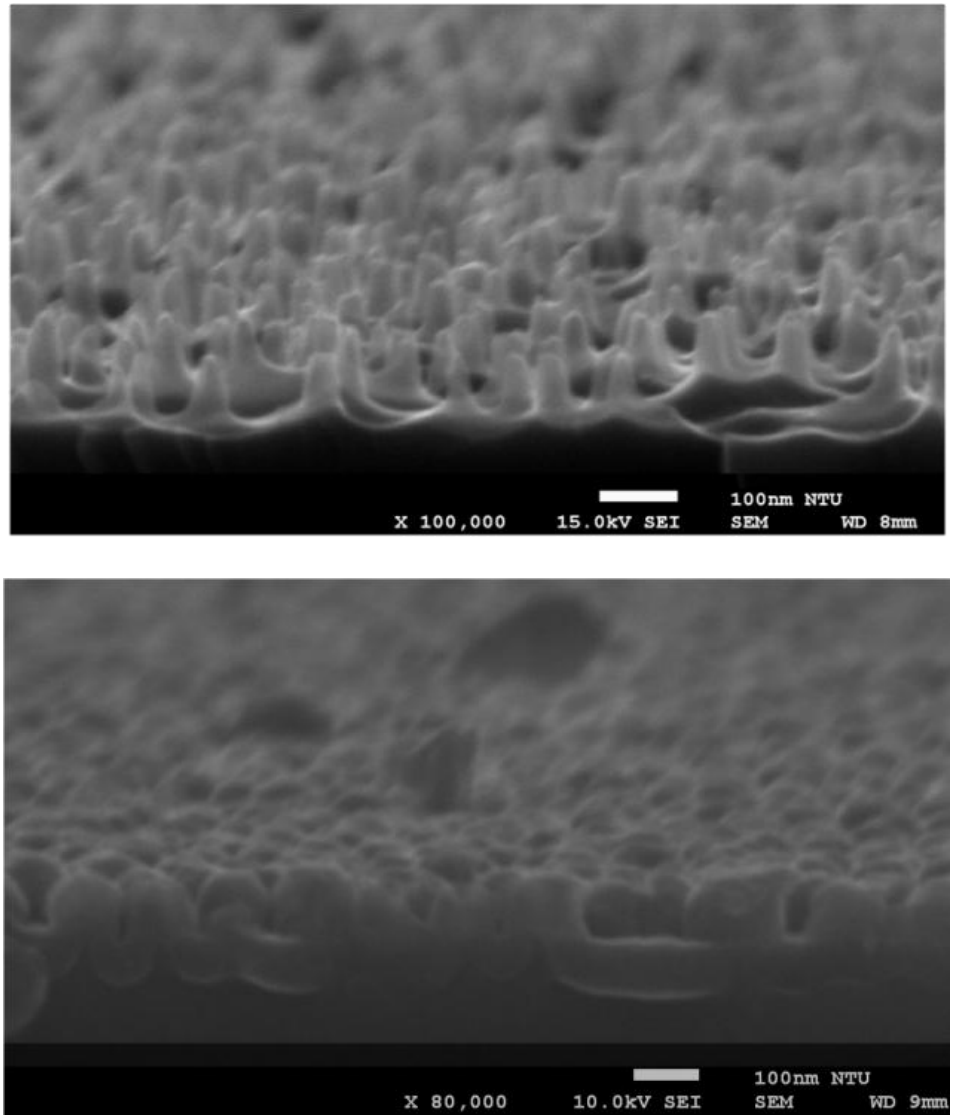

Fig. 3-12: The cross-section view of SEM diagrams of a nanopatterned p^+-Si substrate (a) and a-Si(i) thin film on nanopatterned p^+-Si substrate (b).

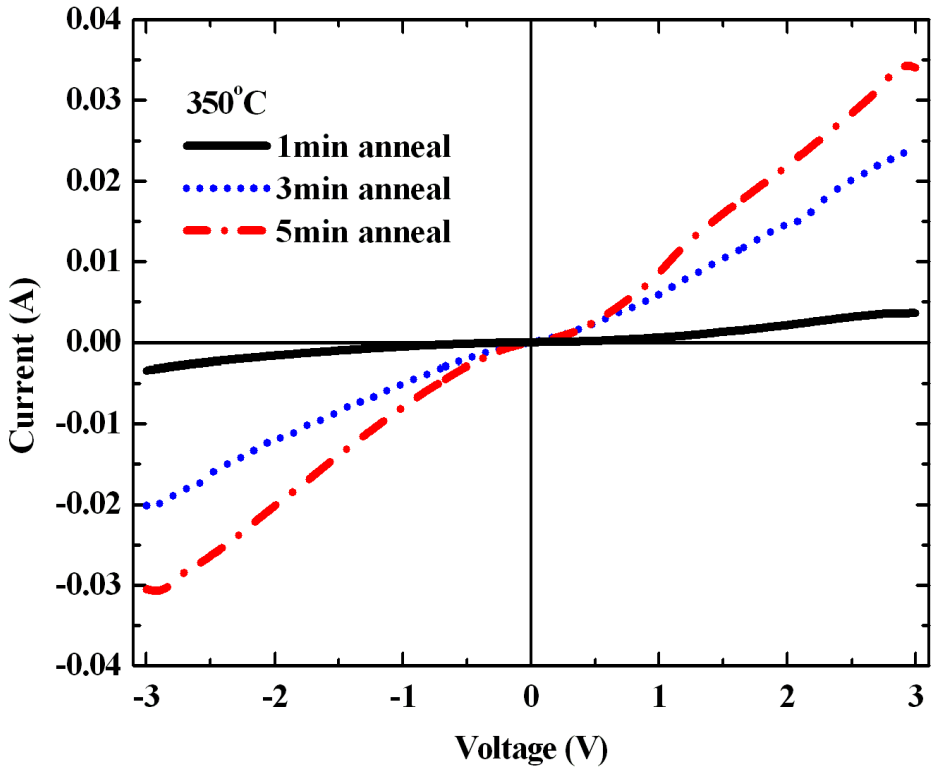

(a)

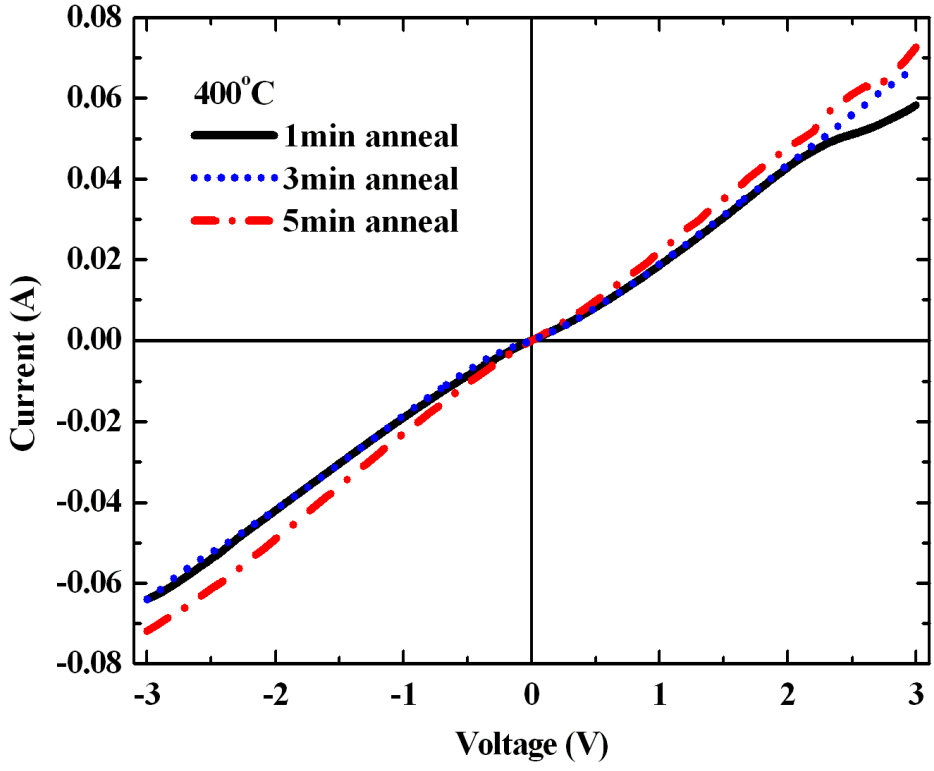

(b)

Fig. 3-13: The current-voltage curve showed the contact characteristics of Al/p^+-Si under 350°C post annealing temperature for 1, 3 and 5 mins (a) and 400°C post annealing temperature for 1, 3 and 5mins (b), respectively.

of 400^{o}C annealing temperature and 5mins annealing time for Al on p^{+}-Si.

We would like to perform metal annealing in one step. It will cause less thermal damages on semiconductor during the second annealing process. In order to keep the characteristic of a-Si(i) thin layer, the high temperature process couldn't be considered in our fabrication process. The annealing temperature of 400^{o}C was performed under different activation temperature of n-GZO and annealing time. The I-V curve of Ti/Au and n-GZO in Fig. 3-14 indicated the better ohmic-like behavior observed in the process condition of 400^{o}C n-GZO activation temperature. From the observation of contact tests, we could successfully perform the metal thermal annealing in one step process. The detail annealing tests were listed in Table 3-4.

Finally, the Al (200 nm) and Ti/Au (12 nm/200 nm) were evaporated as the p-type and n-type contact electrodes, respectively. They were separately alloyed to achieve optimum contact conditions. For all the samples investigated, the mesa area is 300×300μm^{2}.

3-3 Characterizations of photodiodes

3-3-1 Electrical properties

The electrical properties were characterized using an Agilent HP-4155C semiconductor parameter analyzer. As shown in the inset of Fig. 3-15, the I-V curves

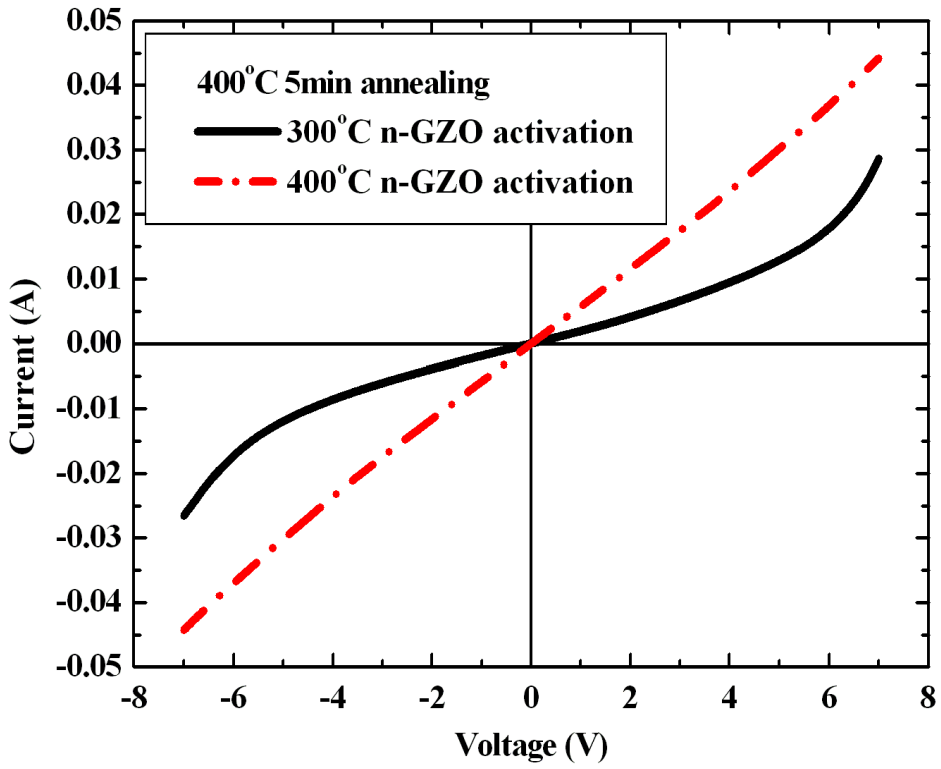

(a)

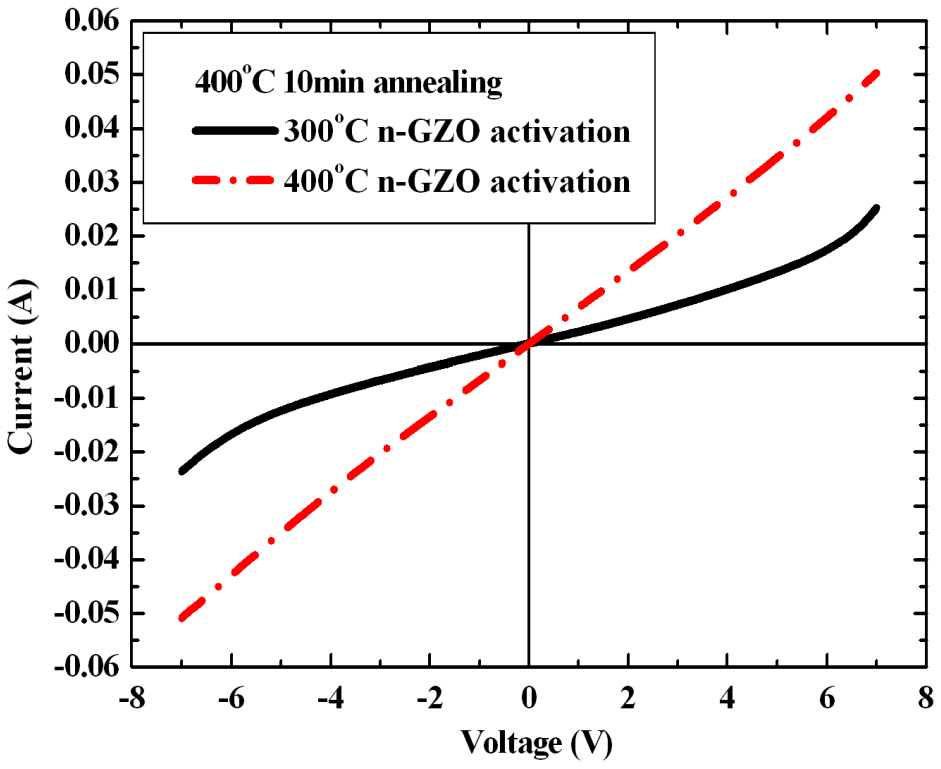

(b)

Fig. 3-14: The current-voltage curves of Ti/Au on n-GZO under different activation condition (300°C and 400°C) annealing time, 5min (a) and 10min (b), under 400°C annealing temperature.

are linear for Ti/Au contacts on the planar n-GZO (right) and Al on the planar p^+-Si (left), respectively, indicating the formation of ohmic contacts on both n- and p- pads. And from Fig. 3-15, the dark current-voltage (I-V) curves suggest a nonlinear rectifying behavior for all devices. The leakage currents are 99.2 nA, 67.6 nA, 355.2 nA and 108.3 nA for device A, B, C and D, respectively, at a bias voltage of -2.5 V. From the diagram we also can observe an increase of forward voltage for devices B, C and D, which is attributed to the insertion of the intrinsic a-Si layer.

3-3-2 Optical characterizations of n-GZO/a-Si(i)/p^+-Si heterojunction photodiodes

A. Photoresponsivity

The optical response was measured by illuminating the samples with monochromatic light from a Xenon lamp (SP CM110 1/8 Mononchromater) on the n-GZO side. As demonstrated in Fig. 3-16, the photoresponsivity of device A is basically composed of near band edge absorption of p^+-Si at the wavelength range between 600~800 nm, along with near the n-GZO band edge and n-GZO/p^+-Si heterojunction absorptions at the wavelength around 350 nm~600 nm. The average photoresponsivity at the wavelength between 350 nm and 800 nm is 0.13 A/W for device A. As for device B, a peak wavelength at 530 nm with an average responsivity 0.08 A/W was demonstrated. The main peak at the green band is attributed to the

Table of Metal Contact Test

Ohmic Contact Test	350°C Annealing			400°C Annealing			300°C Activation		400°C Activation	
	1m	3m	5m	1m	3m	5m	5m	10m	5m	10m
Al/p^+-Si	X	X	X	X	○	○	400°C Annealing Temperature			
Au/Ti/n-GZO							X	X	○	○

Table 3-4: The lists of metal contact test were recorded in this table. From the above table, we could perform the one step annealing process of metal contact to prevent from the second thermal annealing damages.

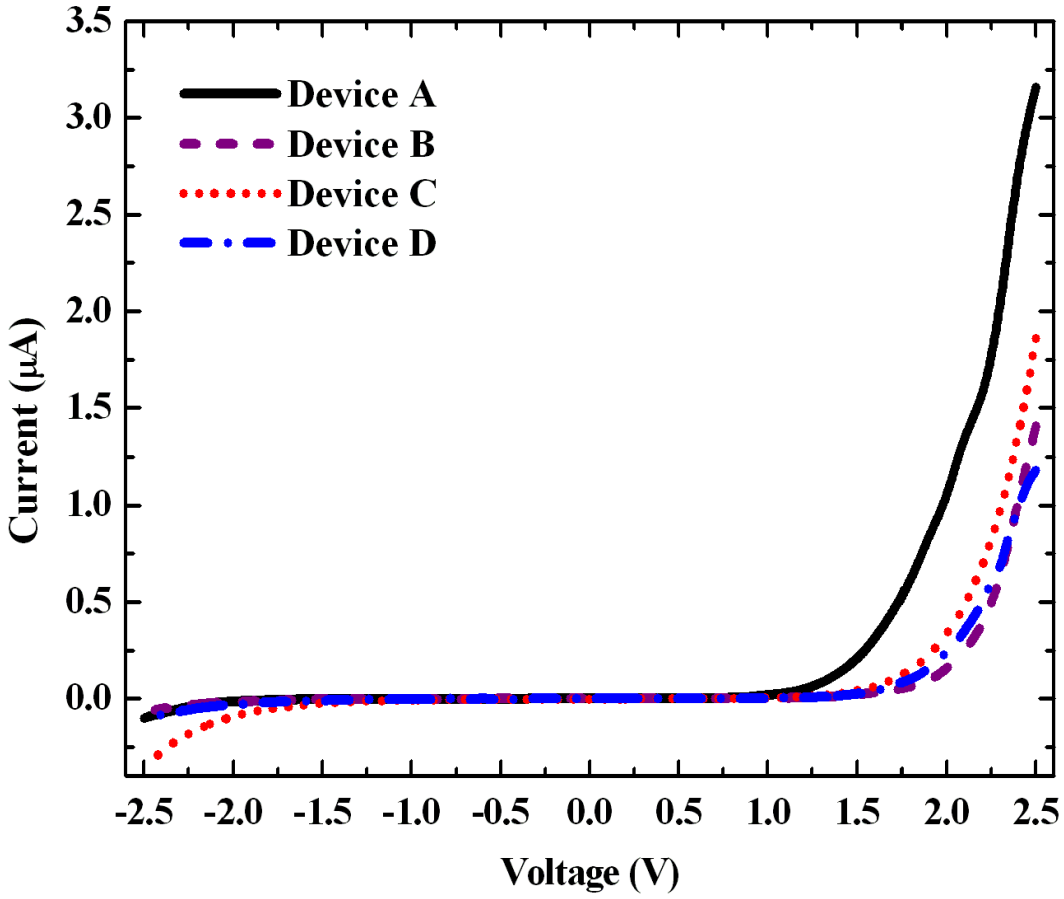

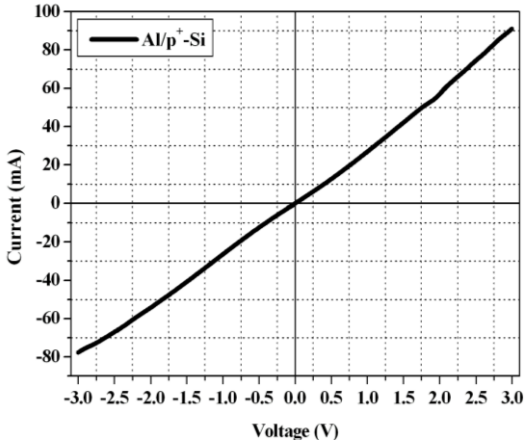

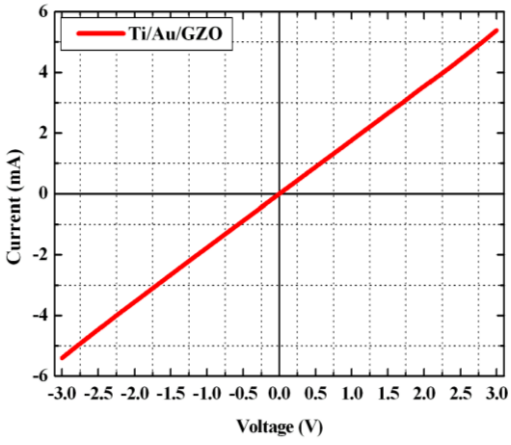

Fig. 3-15: I-V curves of the photodiodes under comparison (Bottom : (left) The I-V curve of the Al contact on p^+-Si; (right) The I-V curve of the Au/Ti contact on n-ZnO. Both curves show good ohmic contact.

dominant absorption in the intrinsic a-Si layer. Also, the decrease of photoresponsivity for device B, as compared with device A, can be ascribed to the potential increase of defects at both a-Si(i)/p^+-Si and n-GZO/a-Si(i) heterojunctions as both a-Si(i) and n-GZO layers were grown at different chambers. In contrast, the device A possesses only one heterojunction (only one interface for defects). On the other hand, device C and D show 32 % and 36.2 % enhancement of photoresponsivity over that of the device A. Also, the responsivity curves of device C and D possessed peaks wavelength near green absorption band. For those two devices, it implies that despite the existence of two heterojunctions (two interfaces of potential pick-up of defects), the nanopatterned a-Si(i) and p^+-Si surfaces can significantly decrease the reflectivity as compared to the planar structure.

B. Reflectance of nanostructure

To understand the effects of nanopatternned photodiodes on the photocurrents, the optical reflectivity was extracted on several material surfaces. For the nanostructure devices, reflectance was originated from two regions which are specular and diffuse reflectivity as below equation.

$$R_{Total} = R_{Specular} + R_{Diffusion}$$

In order to completely observe the reflected characteristic from the nanostructure,

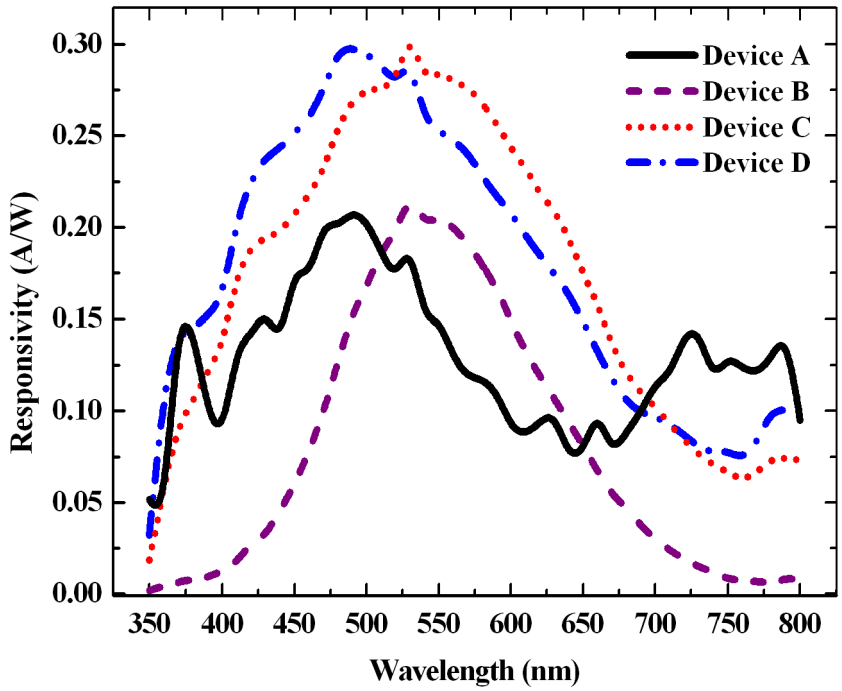

Fig. 3-16: Photoresponsivity curves of the device A, B, C, and D.

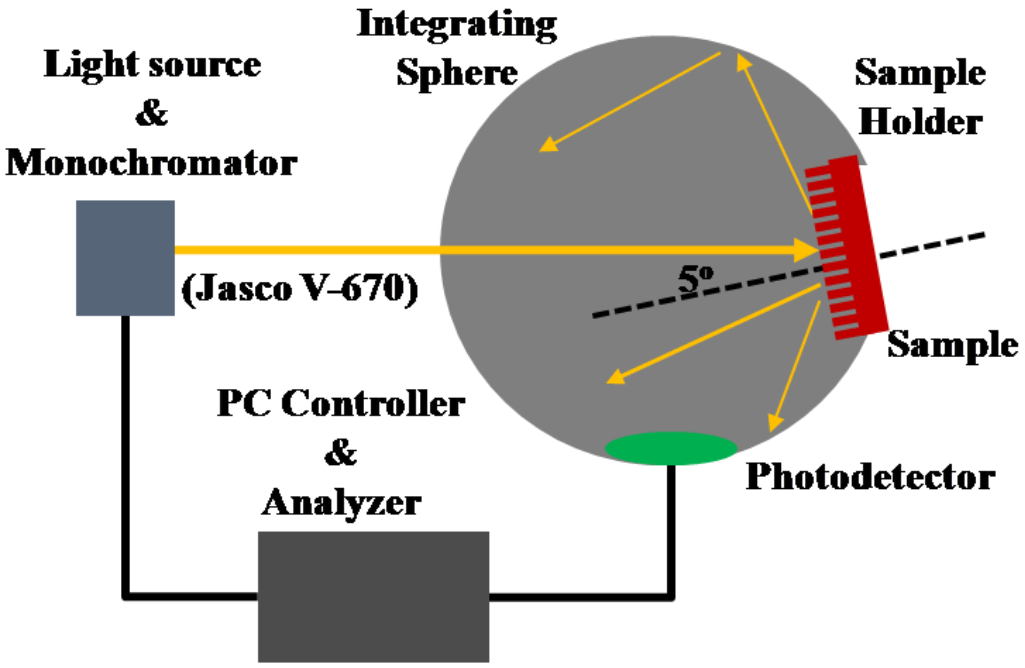

Fig. 3-17: The schematic diagram of reflectance measuring instrument. The measured sample was tiled 5^{o} angle embedded into the integrating sphere. The detector could measure the total reflectance (specular and diffused reflectance). The light source was combined of deuterium and halogen lamp with wavelength 300nm to 800nm.

we use the integrating sphere and spectrometer to measure the reflectivity of samples. The optical reflecting measurements were measured for nearly normalized light incidence (5° offset) covering the spectral regions from 300 nm to 800 nm with a standard UV-VIS spectrometer (JASCO ARN-733) and an integrating sphere. In this measurement, the noise level is ~0.002 %. The schematic diagram of measurement instrument was shown in Fig. 3-17. As shown in Fig. 3-18, the reflectivity of nanopatterned p^+-Si surface is significantly reduced as compared to that of flat p^+-Si surface.

We also observed an even more significant decrease of reflectivity at the shorter wavelength. At the wavelength 443 nm, the reflectivity of nanopatterned p^+-Si is 26.21 % smaller than that of the flat p^+-Si surface, as compared to 7.86 % smaller at 800 nm, which is attributed to a more effective interaction between the nanostructure and the incident light at short wavelength as both sizes are comparable. However, the decreased reflectivity was also observed in the case of nanopatterned a-Si(i)/p^+-Si compared to the planar a-Si(i)/p^+-Si. It could be attributed to the same mechanism with nanopatterned p^+-Si.

C. Discussions on peak shift of photoresponsivity

In addition, the reflectivity comparisons between planar a-Si(i) and nanopatterned

a-Si(i) on the planar p^+-Si substrate also demonstrates a similar trend. However, both the reflectivity of the planar surface and the percentage decrease between flat and nanostructure a-Si (i) are smaller than the case in Fig. 3-18. Since the a-Si (i) layer is grown by HDP-CVD(High Density Plasma Chemical Vapor Deposition), the surface morphology on the "flat" a-Si(i) surface is already rougher than that on flat p^+-Si substrate. Therefore, the percentage reduction of reflectivity in Fig. 3-19 at the short wavelength isn't as significant as that in Fig. 3-18.

The observation of the lower reflectivity at the shorter wavelength indicates the responsivity peaks of devices C and D, in Fig. 3-16, are blue shifted from that of device B. And the further blue shift that device D exhibits is attributed to a lower reflectivity in nanopatterned p^+-Si surface at the shorter wavelength (around 443 nm), by comparing the optical properties with device C. Another explanation of the further blue shift of device D is related to the photocurrents induced at the short wavelength. As pointed out above, the responsivity at the 300nm~600nm wavelength range is mainly contributed by the absorption in the n-GZO layer and the n-GZO/a-Si(i) heterojunction. Since the nanopatterns on device C are realized by dry etching of a-Si(i), the n-GZO/a-Si(i) interface suffers from etching damages and more defects are picked up in the interface. Therefore, the photocurrents at the blue-UV wavelength range of device C are lower than that of device D. Likewise, the etching damages on

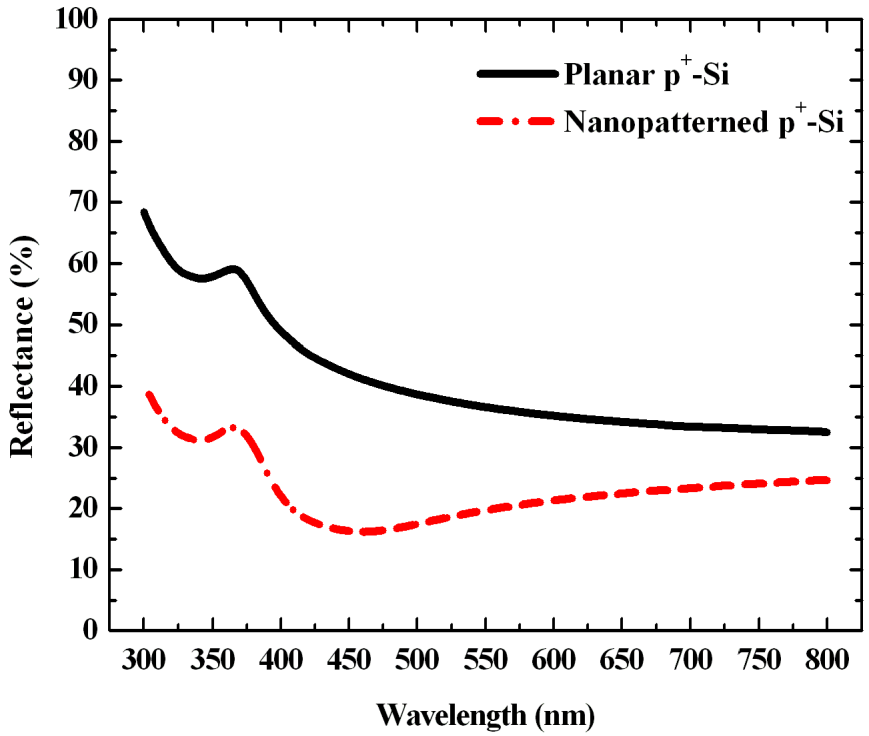

Fig. 3-18: The comparisons of the reflectivity between planar and nanopatterned p^+-Si surfaces. Black solid and red dashed line indicated the reflectivity of planar p^+-Si and nanopatterned p^+-Si substrate, respectively.

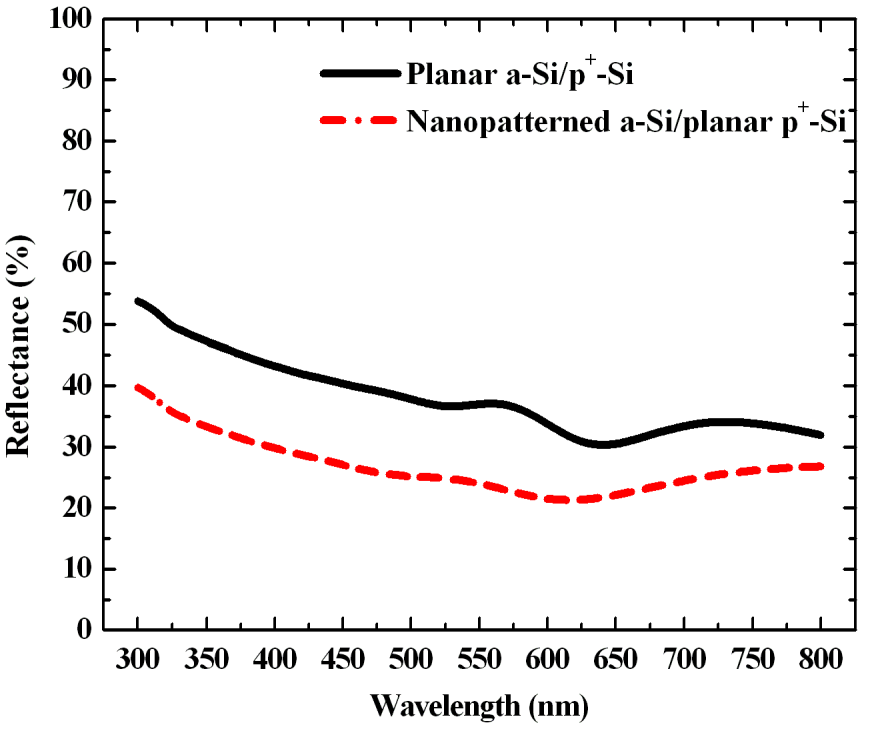

Fig. 3-19: The reflectivity between planar a-Si and nanopatterned a-Si layers on planar p^+-Si substrates. Black solid and red dashed lines indicated the planar a-Si (i) thin film/p+-Si and nanopatterened a-Si (i)/p^+-Si devices, respectively.

p^+-Si of device D result in more defects in the a-Si(i)/p^+-Si junction and less photo-currents in accordance.

D. Wide acceptance angle

We next investigate the effects of nanopatterned surface on the acceptance angle of the photodiodes with a-Si(i) layer, i.e. devices B, C and D. The angle dependent photoresponsivity measurement was performed by illuminating the samples with a uniform and constant optical density of light source at various wavelengths using the setup described in the previous research [24]. In this experiment, the samples were illuminated at a distance 50mm away from the light source. For ease of comparison, at different wavelengths, photocurrents of devices C and D are normalized to that of the device B in the vertical direction (0◦). In Fig. 3-20 to Fig. 3-21, the normalized photocurrents of devices B, C and D are plotted under different incident angles at the major visible wavelengths 450, 550, 650, and 750 nm. Basically, for the device B, photocurrent decays continuously as the incident angle is tilted since the effective radiative energy received by the device becomes smaller. The acceptance angle of device B, defined as the incident angle at 90% of the maximum light absorption, is 20^o, 17^o, 18^o and 18^o at the wavelength 450 nm, 550 nm, 650 nm and 750 nm, respectively. In comparison, the acceptance angles of devices C and D demonstrate an increase.

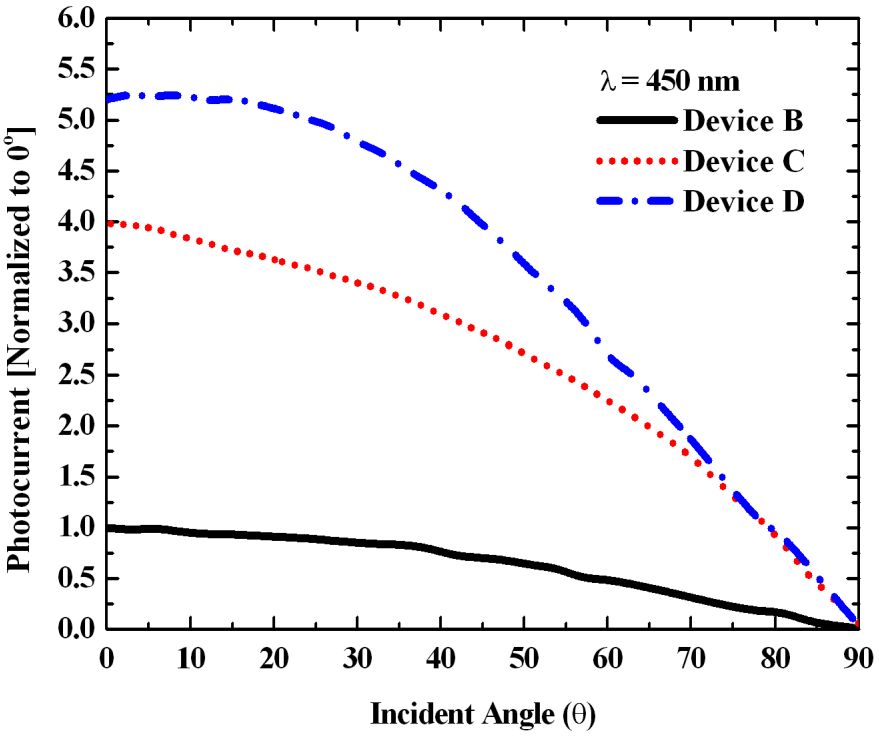

Fig. 3-20: Comparisons of the acceptance angles of device B, C, and D at the wavelength 450nm. The photocurrents are normalized to the photocurrent of the conventional photodiode at 0^{o}.

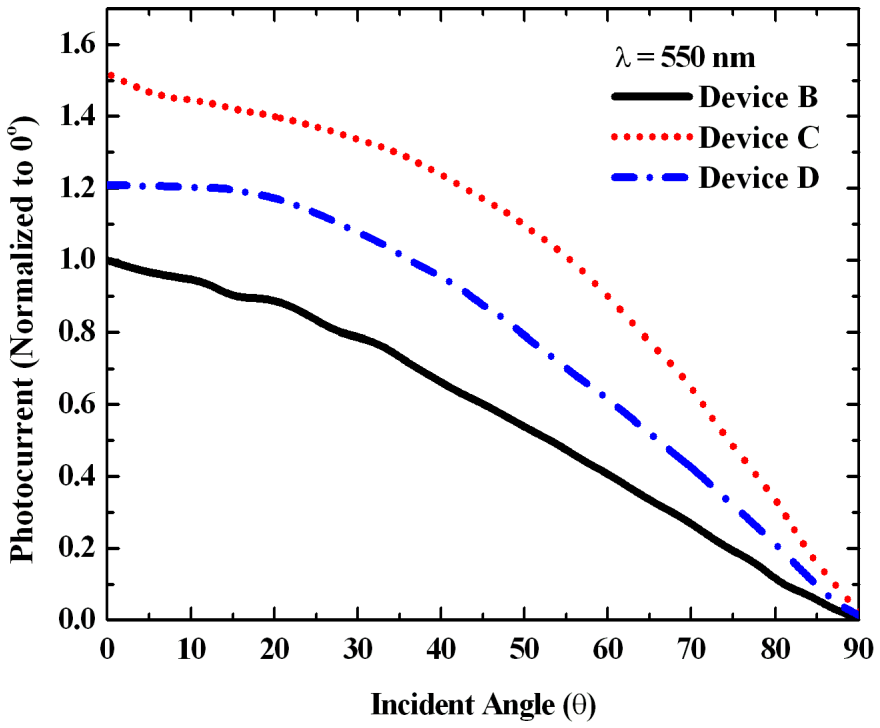

Fig. 3-21: Comparisons of the acceptance angles of device B, C, and D at the wavelength 550nm(b). The photocurrents are normalized to the photocurrent of the conventional photodiode at 0^{o}.

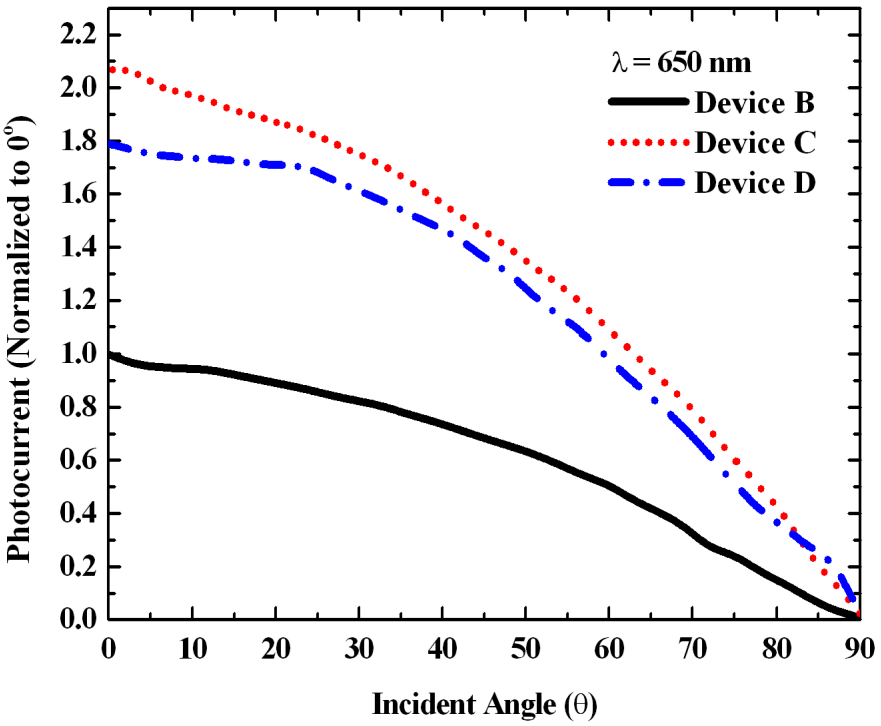

Fig. 3-22: Comparisons of the acceptance angles of device B, C, and D at the wavelength of 650nm. The photocurrents are normalized to the photocurrent of the conventional photodiode at 0^{o}.

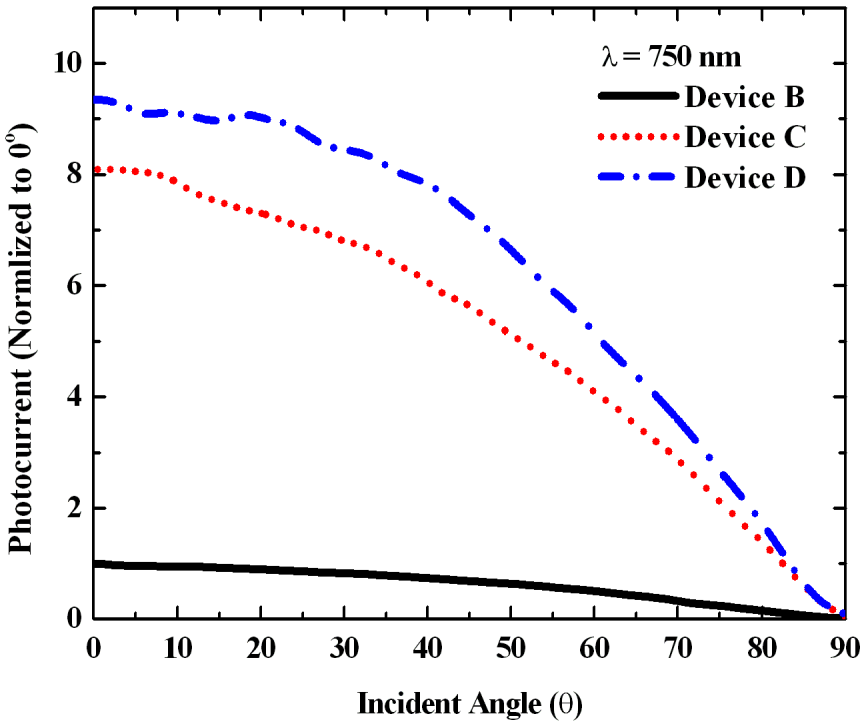

Fig. 3-23: Comparisons of the acceptance angles of device B, C, and D at the wavelength of 650nm(c) and 750nm (d). The photocurrents are normalized to the photocurrent of the conventional photodiode at 0^{o}.

They becomes 22^o, 25^o, 22^o and 21^o for device C and 34^o, 29^o, 31^o and 31^o for device D at the wavelength 450 nm, 550 nm, 650 nm and 750 nm, respectively.

E. The mechanism of improved acceptance angle

The increase of acceptance angle is mainly attributed to the nanopatterned surface as indicated in previous reports [3, 107-108] that surface morphology plays an important role on the wide incident angle of absorbance. Moreover, we also notice larger acceptance angles of device D than those of device C at all the wavelength measured. From the SEM photos in Fig. 3 along with the schematic plots in Fig. 3-11, device C shows a nanorod structure while device D possesses nanocone morphology due to the coverage of both a-Si(i) and n-GZO layers. Zhu et al. indicated the nanocone structure have the wider incident angle of absorbance than the nanorod structure [3, 107-108], the nanostructure was fabricated by the nanosphere lithography. When the incident light is tilted, photons have more chance to fall within the angle of internal reflection for the nanocone structure and thus the acceptance angle is increased.

3-3-3 Investigations on transit time of nanostructure photodiodes

A. Experimental setup

The experimental setup of transit time was shown in Fig. 3-24. We used the LEDs

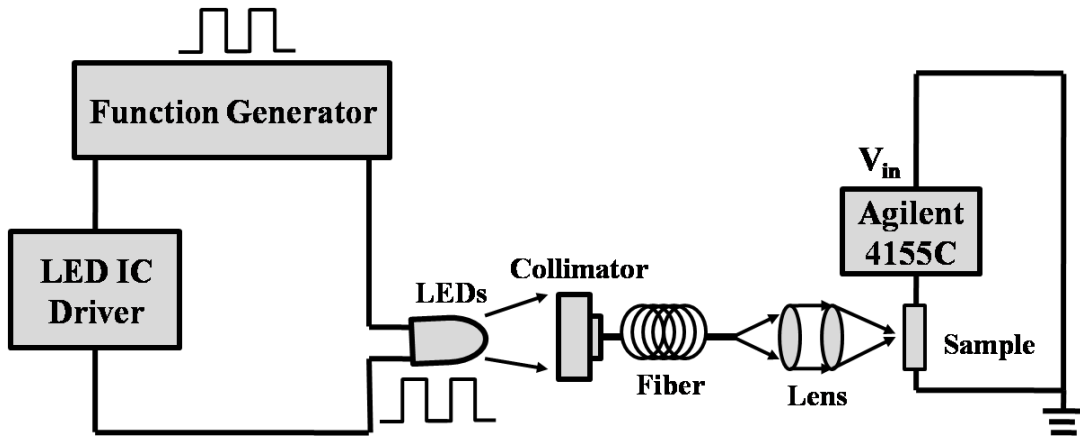

Fig. 3-24: Experimental setup for transit time measurement of heterojunction photodiodes.

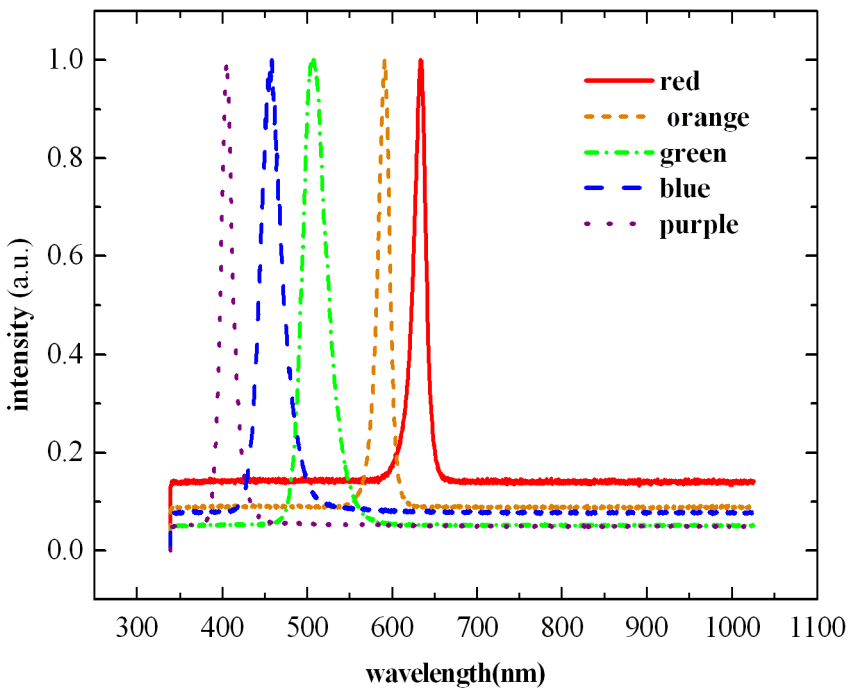

Fig. 3-25: EL (Electroluminescence) spectra of different wavelength LEDs.

as light source and were illuminate on the surface of photodiodes. The incident light possessed the period of 100ms with 50% duty cycle. We listed the normalized EL spectra of LEDs with different wavelength peak, 404.8nm, 458.8nm, 516.9nm, 591.4nm and 633.3nm, respectively, to confirm the FWHM of LEDs. The FWHM of LEDs which we choose is ranged between 10nm to 35nm, shown in Fig. 3-25. The detail specifications were listed in Table 3-5. Following, we modulate the periods of LEDs emission and measure the photocurrents by using an Agilent 4155C semiconductor parameter analyzer. The light intensity of LEDs was measured by photometer. We designed two experiments, constant incident light intensity and constant photocurrents, to investigate the mechanism of carrier transition for the comparisons between device B, C and D. Unfortunately, the responsivity of photodiodes at 404.8nm is too small to analyze.

B. Results and discussions on transit time

B-1 Constant incident light intensity

B-1-1 Comparisons on different devices

In Fig. 3-26, we could observe the transit time of device B, C and D under constant incident light intensity with 633.3nm wavelength. In Fig. 3-26, the photocurrents of device B, C and D are different and follow the trends of photoresponsivity at 633.3nm

The Speculations of LEDs

	Wavelength	FWHM
Red LED	633.3nm	16nm
Orange LED	591.4nm	15.85nm
Green LED	516.9nm	34.95nm
Blue LED	458.8nm	24.87nm
Purple LED	404.8	15.25nm

Table 3-5: The speculations of LED emission peak wavelength and FWHM (Full Width Half Maximum).

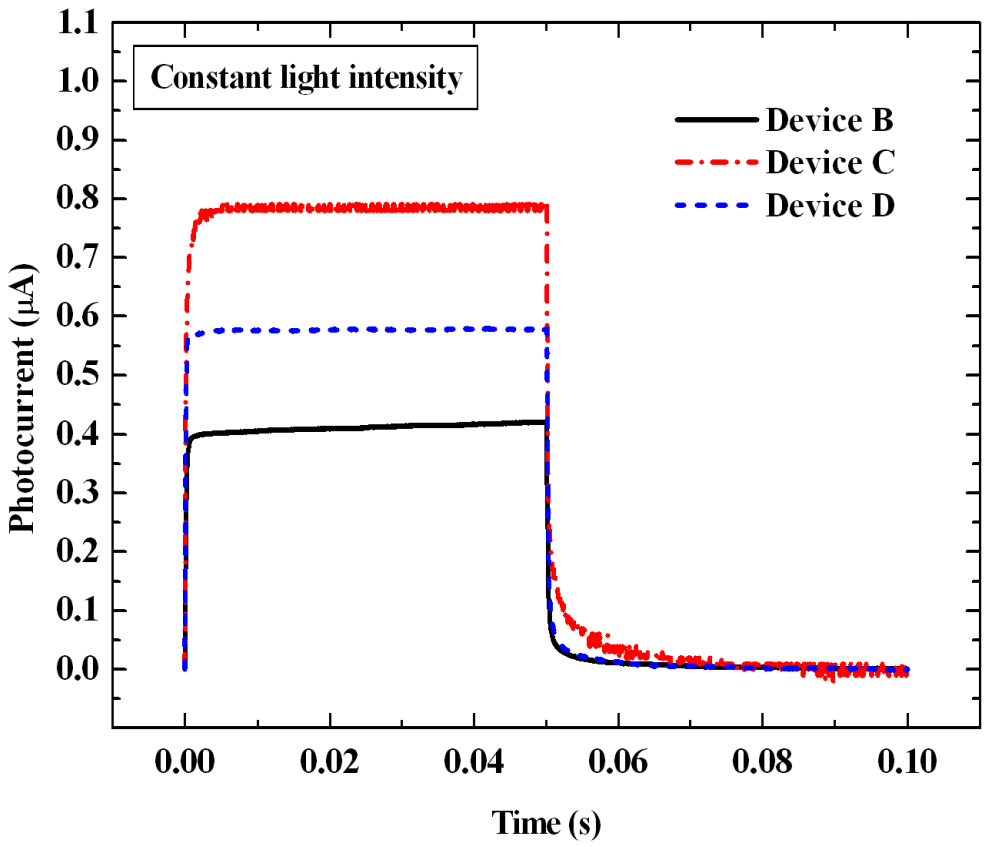

Fig. 3-26: The curve of transit time under constant incident light intensity on device B, C and D at the wavelength of 633.3nm.

wavelength which is shown in Fig.3-16. Following, we measured the transit time of device B, C and D under different wavelength with constant incident light intensity of 3.5μW. The measured data were listed in Table 3-6. The relations between rise time and LED wavelength were shown in Fig. 3-27. In device B, less photocurrent were generated and it is possible due to the higher reflectivity compared to other devices, shown in Fig. 3-19. However, more photocurrents in device will be possible to cause the high probability of collision and result in the longer transit time. Therefore, photocurrents generated in device B were much less than in the device C and shorter transit time will be possessed. Therefore, the transit time of device C is longer than device B which is probably attributed to the existence of planar interface between a-Si(i) and p^+-Si and more photocurrents were generated in device C. Finally, we observed the longer transit time in device C than it in device D. However, we discovered the photocurrents in device D more than in device C. Nanostructure could be one critical factor on the behavior of transit time. The sketched diagram of carrier transportation in devices was shown in Fig. 3-29. Nanostructure devices could provide the shorter transit paths for carrier transporting to contact electrodes as showed in Fig. 3-29 (a) and (b) which will decrease the probability of carrier recombination during the transporting process in devices and result in the shorter transit time.

Table of Transit Time under Constant Incident Light Intensity

Constant Light Intensity	Device C		Device D		Device E	
	Rise time	Fall time	Rise time	Fall time	Rise time	Fall time
633.3nm	0.39ms	1.34ms	0.76ms	3.67ms	0.29ms	1.19ms
591.4nm	0.29ms	1.2ms	0.33ms	2.6ms	0.23ms	0.84ms
516.9nm	0.36ms	1.03ms	0.6ms	2.54ms	0.27ms	0.74ms
458.8nm	0.79ms	3.21ms	0.91ms	3.2ms	0.39ms	0.86ms

Table 3-6: The transit time of device B, C and D under constant incident light intensity with different wavelength.

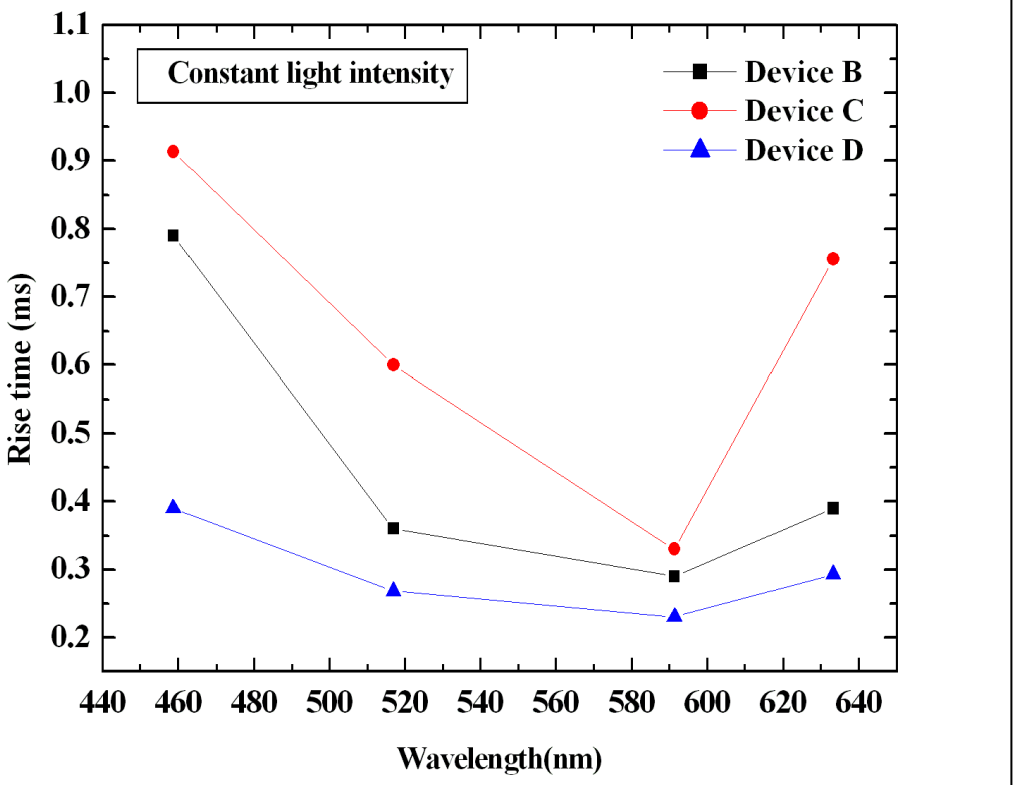

Fig. 3-27: The rising time of device B, C and D under constant incident light intensity.

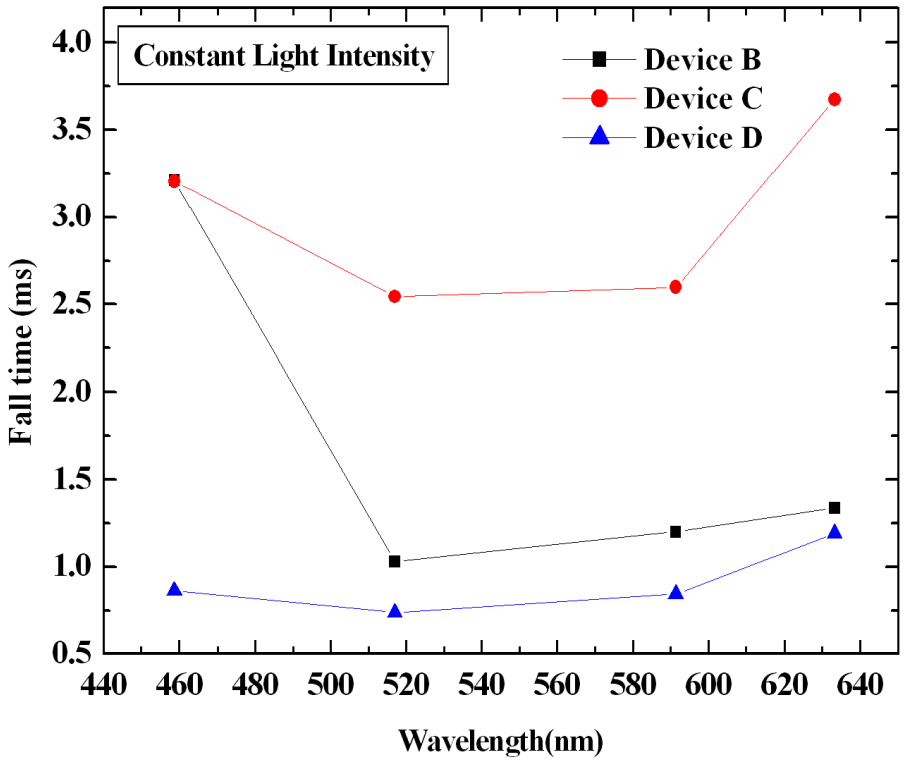

Fig. 3-28: The falling time of device B, C and D under constant incident light intensity.

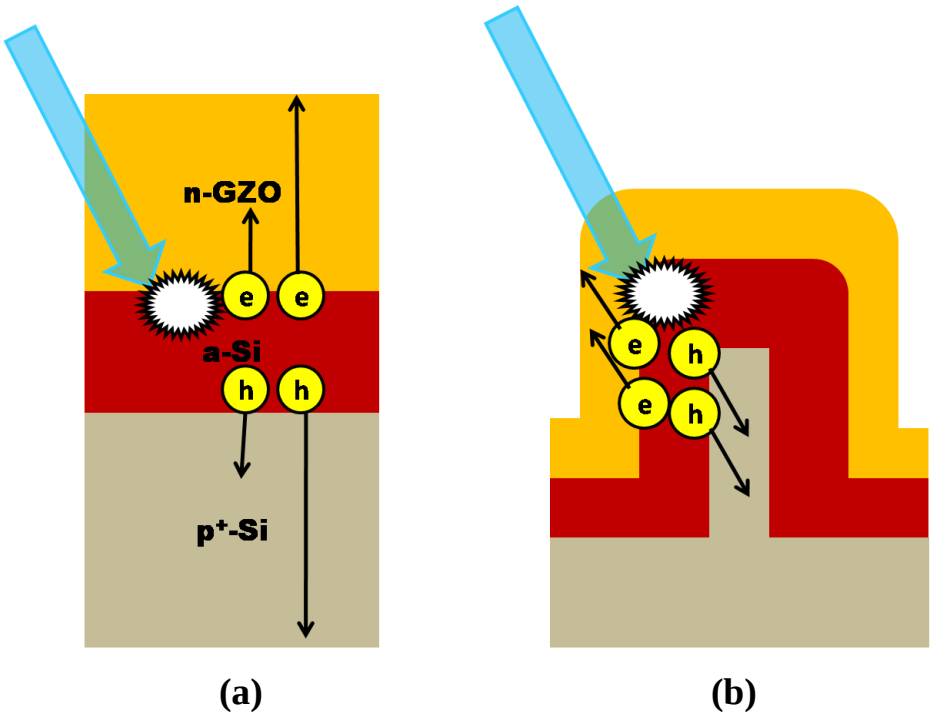

Fig. 3-29: The sketched diagram showed the mechanism of carrier transportation between planar and nanopatterend photodiodes. The nanostructure could offer the shorter transit paths in the device.

B-1-2 Relations between wavelength and transit time

We further discussed the mechanism of transit time under different LED wavelength at the constant incident light intensity. The similar tendency was observed in device B, C and D. In Fig. 3-16, device B, C and D possessed the low responsivity at 633.3nm than at 516.9nm. However, the reflectivity showed the contrary behavior in Fig. 3-19. We observed the longer transit time at 633.3nm. It indicated that lower transit time could help carrier effectively transporting to contact electrodes and could reduce the carrier recombination in devices. However, high reflectivity and long transit time resulted in the small photoresponsivity which could be observed at 458.5nm wavelength. However, there are two mechanisms to affect the transit time, quantity of photocurrent and device structure. Furthermore, we compared the tendency of rise and fall time under constant incident light intensity which was shown in Fig. 3-27 and Fig. 3-28. The reflectivity in Fig. 3-19 indicated the similar value between 633.3nm and 591.4nm. However, shorter transit time was observed at 591.4nm for device B, C and D compared to it at 633.3nm. When we illuminate the constant incident light intensity on devices, the responsivity could be probably related with reflectivity, carrier transit time and the location of carrier generated. The drastic decreasing relaxation time at 591.4nm is hard to explain from the condition of constant incident light intensity. However, we try to analyze the behavior of transit time in nanostructure photodiodes as another

experimental condition, constant photocurrents. And, the detail discussion will be given in next section.

B-2 Constant photocurrents

B-2-1 Comparisons on different devices

From the above discussions of transit time under constant incident light intensity, the quantity of photocurrent will probably affect the behavior of transit time which was discussed in previous section. In order to realize the behaviors of transit time on different nanostructure, we modified the photocurrents of device to the same quantity. Under this condition, the considerations of photocurrent quantity could be neglected and the advantage of nanostructure on transit time analysis could be realized much easily. The curve of transit time under constant photocurrents, 750nA, at different LED wavelength was shown in Fig. 3-30. The detail transit times of device B, C and D were listed in Table 3-7 for reference. The similar tendency of transit time could be observed in Fig. 3-31 and 3-32 and it indicated that device D possessed the shorter transit time compared to device B and C which is probably due to the more transit paths in device D as sketched in Fig. 3-33. Under the light illumination, photocurrents were generated and transport to contact electrodes through the shortest path. Without considering the issue of defects and traps in device, nanostructure devices could offer more transit paths for

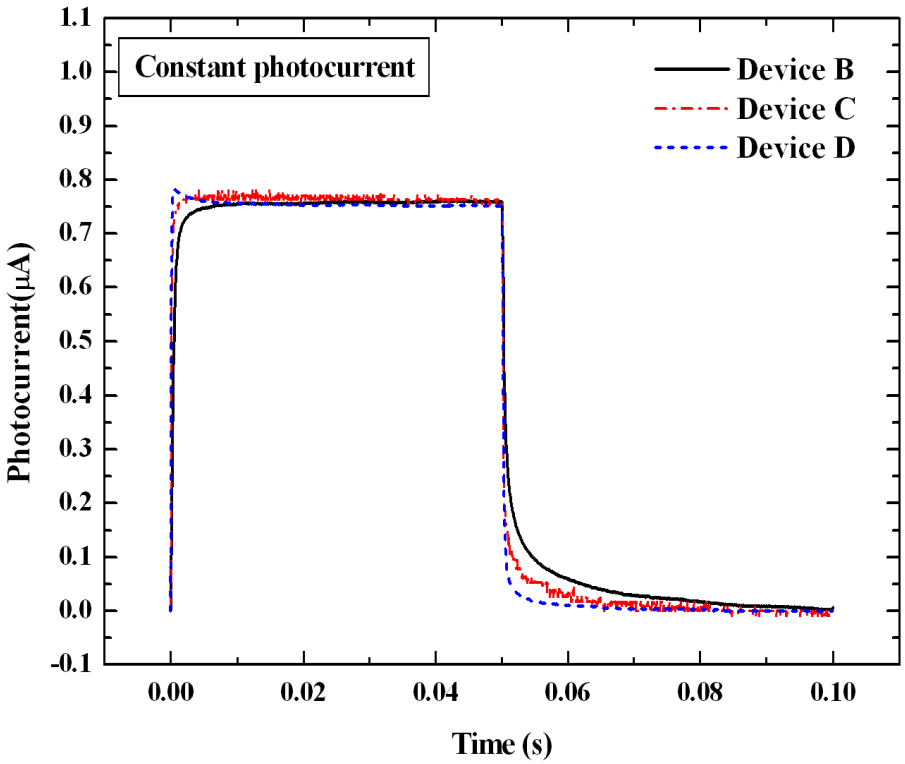

Fig. 3-30: The curve of transit time under constant photocurrents for device B, C and D at the wavelength of 591.4nm.

Table of Transit Time under Constant Photocurrents

Constant Photo-current	Device B		Device C		Device D	
	Rise time	Fall time	Rise time	Fall time	Rise time	Fall time
633.3nm	0.78ms	4.17ms	0.63ms	2.96ms	0.25ms	0.92ms
591.4nm	1.06ms	5.27ms	0.38ms	2.75ms	0.23ms	0.81ms
516.9nm	1.03ms	5.77ms	0.45ms	2.66ms	0.25ms	0.78ms
458.8nm	1.55ms	5.72ms	0.86ms	3.19ms	0.51ms	0.96ms

Table 3-7: The transit time of device B, C and D under constant photocurrents.

carrier to decrease the probability of carrier collisions and could result in the shorter transit time.

B-2-2 Relations between wavelength and transit time

The wavelength dependent behavior was observed in Fig. 3-31 and 3-32. The transit time in device B becomes shorter at the longer light wavelength. The possible mechanism resulted in the longer transit time is due to the slower hole mobility than electron. The hole will transport to the p-type contact electrode after applying the reverse bias. The photocurrent was generated near the p^+-Si substrate at the illuminating light with 633.3nm and the shorter transit path will probably result in the shorter transit time. Due to this mechanism, the wavelength-dependent transit time could be realized in device B, planar n-GZO/a-Si(i)/p^+-Si heterojunction photodiodes. However, nanostructure could offer the advantage of shorter transit time at all wavelength and had been discussed in section B-2-1. The much shorter transit time was observed at 516.9nm and 591.4nm for device C which is due to the nanostructure of device. Nanopatterns were fabricated in the interface of n-GZO and a-Si(i) thin layer which would offer the shorter transit paths for carriers throughout the interface of n-GZO and a-Si(i) thin layer and could result in the shorter transit time in device C and D compared to device B. Furthermore, device D possessed the shorter transit time form 516.9nm to 633.3nm

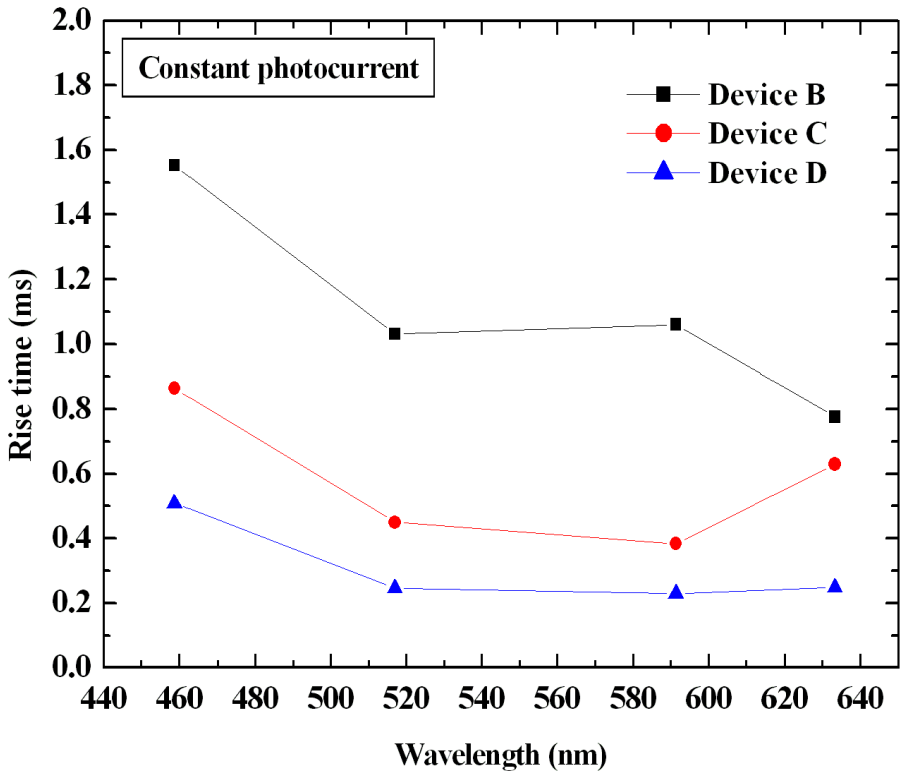

Fig. 3-31: The rising time of device B, C and D under constant photocurrents.

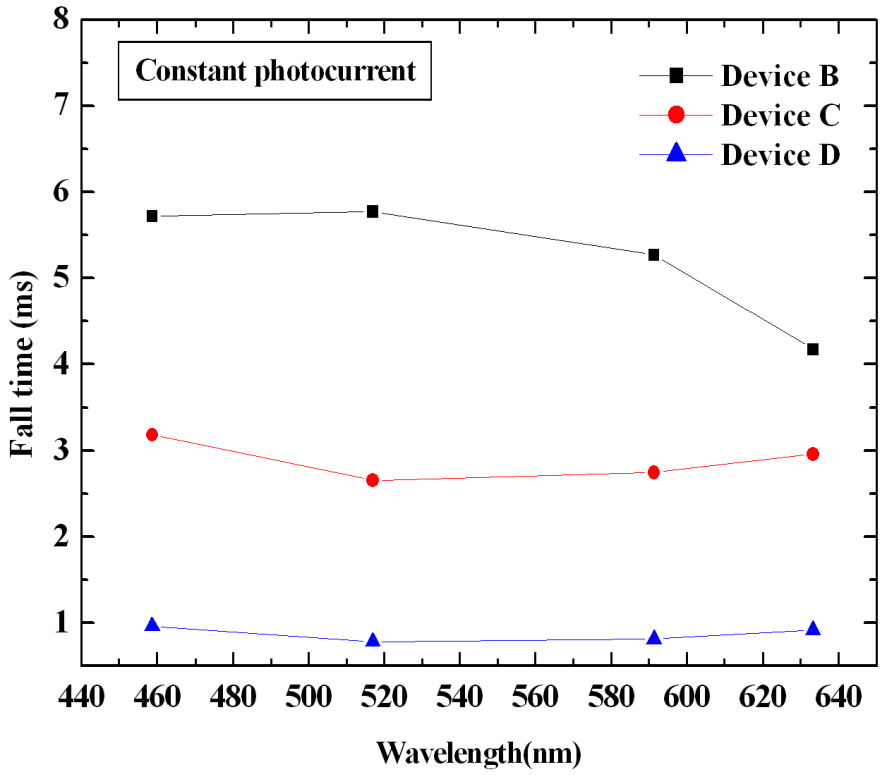

Fig. 3-32: The falling time of device B, C and D under constant photocurrents.

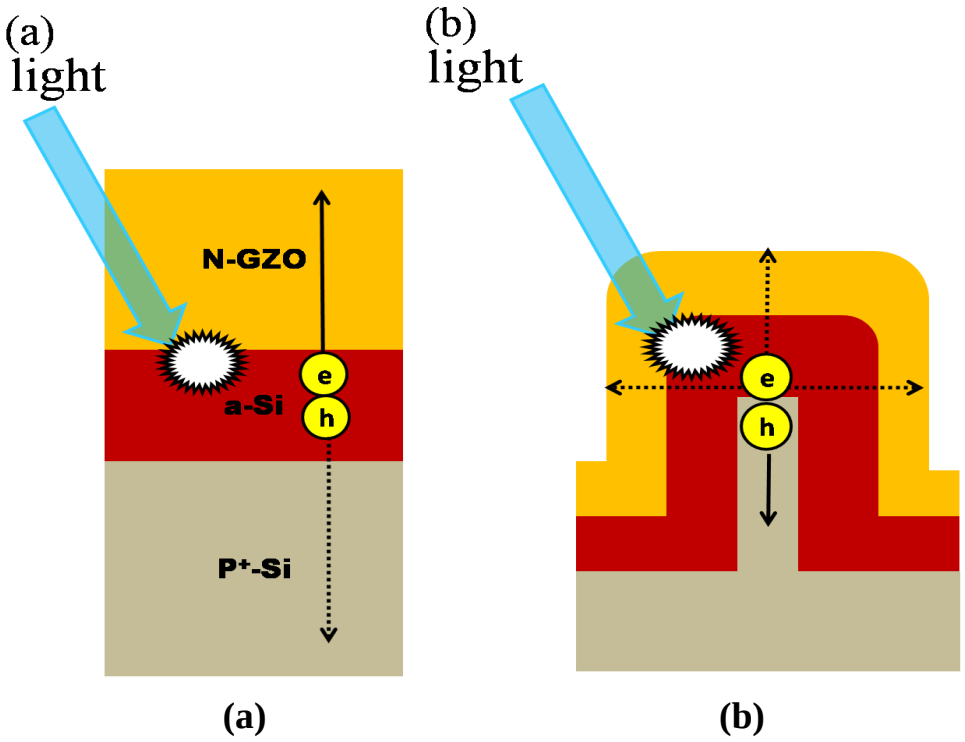

Fig. 3-33: The sketched diagram showed the mechanism of carrier transportation between planar and nanopatterned photodiodes.

which is probably due to the nanostructure fabricated in the interface of a-Si(i) and p^+-Si and lead to the shorter carrier transit time in these wavelengths. Finally, nanostructure devices which possessed the shorter transit time by offering the more transit paths could be realized in above discussions.

3-4 Conclusions

In this work, the n-GZO/a-Si(i)/p^+-Si heterojunction photodiodes were fabricated. As compared with the n-GZO/p^+-Si sample (device A), the photodiodes with nanopatterned a-Si(i) (device C) and nanopatterned p^+-Si substrate (device D) show 32% and 36.2% enhancement of photoresponsivity. And they also show main absorption peaks at the green wavelength range which is correlated to the a-Si(i) absorption. In comparisons, the multiple band absorption peak for device A correspond to n-GZO, Si and n-GZO/Si(i) junction absorptions. We also observe a blue shift of photoresponsivity spectra on nanopatterned devices as compared with that of a planar n-GZO/a-Si(i)/p^+-Si photodiode (device B), which is attributed to more obvious decreasing of reflectivity in the short wavelength range. Furthermore, the acceptance angle measurement reveals that nanostructure photodiodes have larger acceptance angles than the planar one. For example, at 550 nm, the acceptance angle increases from 17^o for device B to 25^o and 29^o for devices C and D, respectively. Our

results also show that the nanocone structure of device D has higher acceptance angle than the nanorod structure of device C. In the discussion related to transit time, we observed that devices D possessed the shorter transit time which is probably due to the effective transit path and more transit paths which were offered by nanostructure photodiodes. The carrier recombination in devices would be less when the devices possessed the short transit time. Finally, this work concluded that nanopatterned n-GZO/a-Si(i)/p^+-Si photodiodes have the infinite potential applications to solar cells.

Chapter 4

Conclusions

To summarize this dissertation, we try to propose some methods for solving the problems in solar cells by investigating the characteristic of heterojunction photodiodes under reverse bias voltage. In chapter 2, the visualization of combining n-GZO and p-Si semiconductors showed the broad band absorption spectrum on responsivity. The technique of silica nanosphere spraying was applied on the device to enhance the photoresponsivity and acceptance angle of photodiodes. The enhanced photoresponsivity between 400nm to 650nm is due to the refractive index match and light trapping by SiO_2 nanosphere. However, the wide acceptance in n-ZnO/p-Si photodiodes with SiO_2 nanoparticle coated could be explained by the effect of 2-D Bragg diffraction, Litterow configuration. The n-GZO/p-Si heterojunction photodiodes possessing the potential application to solar cells.

Furthermore, by using the novel and simple self-masked nanosphere lithography, we fabricated the nanopatterns on p^+-Si substrate and successfully manufactured the nanostructure n-GZO/a-Si(i)/p^+-Si heterojunction photodiodes. The characterisitics of high photoresponsivity, wide acceptance angle and short transit time were observed in nanostructure photodiodes. The photoresponsivity of n-GZO/a-Si(i)/nanopatterned p^+-Si

heterojunction photodiodes has 36.2% enhancement compared to it of planar n-GZO/a-Si(i)/p^+-Si heterojunction photodiodes. However, the characteristic of wide acceptance angle could be observed by spraying the silica nanosphere on the top of photodiodes surface and in nanostructure photodiodes. The wide acceptance angle in n-GZO/a-Si(i)/ nanopatterned p^+-Si photodiodes is due to the nanocone morphology which has the wide absorbance incident angle. However, n-ZnO/nanopatterned a-Si(i)/p^+-Si photodiodes has the nanorod structure and possesses the smaller acceptance angle compared n-GZO/a-Si(i)/nanopatterned p^+-Si photodiodes. Finally, the transit time of nanostructure photodiodes was investigated under constant light intensity and photocurrent. We realized that the shorter transit time in nanostructure photodiodes could provide effective and more transit paths for carrier transporting to contact electrodes compared to planar photodiodes. The nanostructure photodiodes possessed lower surface reflectivity and shorter transit time compared to the planar photodiodes. Finally, this work concluded that self-masked nanosphere lithography and nanopatterned n-GZO/a-Si(i)/p^+-Si photodiodes have potential applications to solar cells.

Appendix 1

394nm EL emission in n-ZnO/p-GaN LEDs with effective silica current blocking layer

In this chapter, we investigated the electrical and optical characteristics of ZnO based optoelectronics for the application of light emitting diodes (LEDs).From the past reports, the EL emission of n-ZnO/p-GaN light emitting diodes was dominated by the oxygen vacancy (V_o) in ZnO and Mg^+ deep level recombination without good electron confinement. It will show the green and yellow broad band emission in EL spectrum. Defects in ZnO material played a serious issue in the UV emission of n-ZnO/p-GaN heterojunction lighting emitting didoes. The emission of oxygen vacancy will compressed the emission of ZnO near band edge. From this viewpoint, we try to fabricate the n-ZnO/p-GaN photodiodes with a thin SiO_2 current blocking layer on the top of p-GaN by RF magnetic sputtering. By utilized this thin SiO_2 current blocking layer, we could well control the emission peak of n-ZnO/p-GaN heterojunction light emitting diodes (LEDs) at 394nm, which is due to the recombination between the interface of n-ZnO/SiO_2 and SiO_2/p-GaN. The detail discussions included the material analysis, device fabrication and results discussing were showed in this chapter.

A1-1 Motivations

In this work, we fabricated the SiO_2 thin film by RF magnetic sputtering between n-ZnO and p-GaN as the current blocking layer. The current blocking layer possessed the behavior of electrons blocking in the interface of n-ZnO/SiO_2. By insertion of thin SiO_2 current blocking layer, we was able to well controlled the emission peak of electroluminescence (EL) at 394nm by low cost process, RF sputtering. The EL spectrums of LEDs with and without SiO_2 current blocking layer were shown and verified the possibility of UV emission in the n-ZnO/SiO_2/p-GaN LEDs by insertion of current blocking layer.

A1-2 The material analysis of ZnO

A1-2-1 Preparation of ZnO thin film

300 nm thick Ga-doped ZnO thin film was deposited at room temperature on 500 μm thick sapphire substrate. Films were deposited by magnetron sputtering a pressed GZO target at a power of 100 W and frequency of 13.56 MHz, in a deposition chamber with base pressure 10^{-6} Torr. The sputtering gas was chosen to be ultra high purity argon. The substrates were placed in close contact with an earthed, room temperature copper backing plate over the center of the target during deposition. Post-deposition annealing of GZO samples was carried out in nitrogen for various temperature and time periods

from 350℃~550℃ for 30min and samples were cooled by placing them on a room temperature ceramic block.

A1-2-2 Photoluminescence (PL) of ZnO

ZnO has the high band gap, 3.37eV, and could be apply to fabricate the UV emission LEDs. However, the photoluminescence (PL) of ZnO will provide the initial evidence for the emission wavelength of LEDs device. In order to investigate the effects of activation temperature, we designed three conditions of temperature as 350^{o}C, 450^{o}C and 550^{o}C for the test of post annealing. The anneal environment was under the N_2 ambient with the pressure of 10^{-3} torr. We varied the annealing temperature as 350^{o}C, 450^{o}C and 500^{o}C at 30mins annealing time to observe the photoluminescence (PL) behavior. In Fig. A1-1, obvious ZnO near band edge (379nm) was observed at the condition of 550^{o}C and 30mins. The green-yellow PL emission at 503nm was compressed by the emission of ZnO near band edge. We observed the blue PL emission at 443nm due to the recombination of zinc interstitial (Zn_i) in n-ZnO. From the PL emission, we could infer the possibility of EL emission in UV wavelength. Recently, some authors have also reported the blue luminescence of ZnO [81, 109]. However, the mechanical responsible for the blue emission is still not clearly understood. Using full-potential linear muffin-tin orbital method, Xu [110] calculated the energy levels of

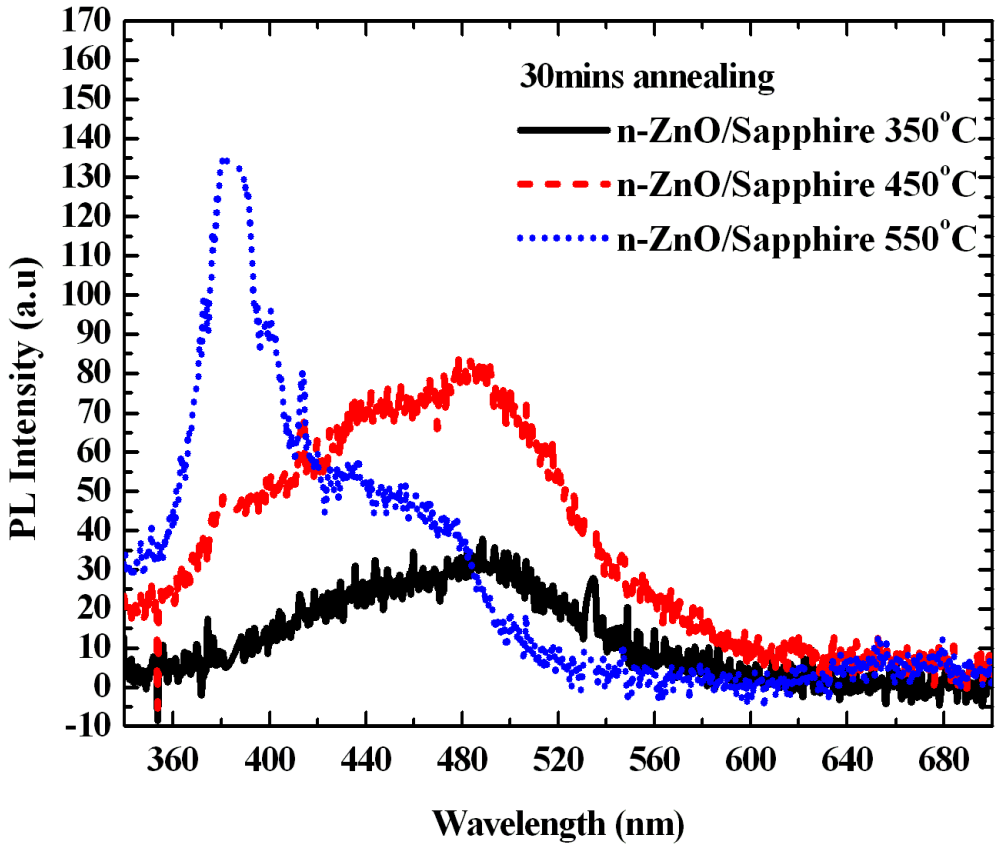

Fig. A1-1: The PL diagram of n-ZnO after post annealing. The device under 550°C 30min post annealing could possess the better photoluminescence characteristics and have the peak wavelength at 380nm.

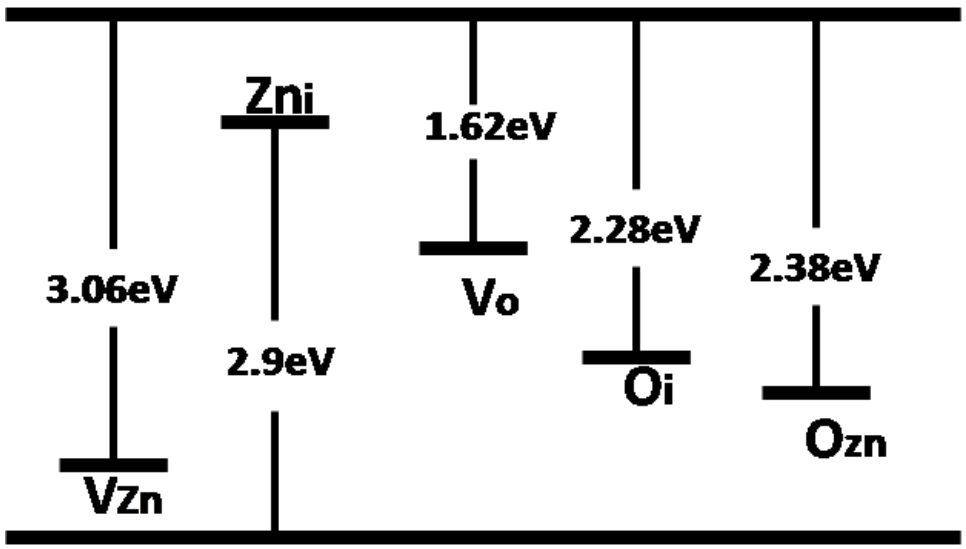

Fig. A1-2: The diagram of transition mechanism of defects in ZnO.

the intrinsic defects in undoped ZnO films, such as oxygen vacancy (V_O), zinc vacancy (V_{Zn}), interstitial oxygen (O_i), interstitial zinc (Zn_i), and anti-site oxygen (O_{Zn}). The result shows in Fig. A1-2. From the transition mechanism of defects in ZnO, 503nm emission could be attributed to anti-site oxygen (O_{Zn}). By the way, the green band emission at 503nm was eliminated by increasing the anneal temperature. This phenomenon could be explained as the material possessing the better band edge recombination by increasing the annealing temperature.

A1-2-3 X-ray diffraction (XRD) of ZnO

The material quality played an important role in the device fabrication. X-ray diffraction (XRD) provided the evidence of material quality. From the historical papers , high quality ZnO has the high c-axis orientation (0002). From this concept, we tried to confirm the device quality of n-ZnO/p-GaN by the result of X-ray diffraction (XRD). In Fig. A1-3, the strong XRD peak could be observed and located at the c-axis orientation (0002), 34.8^o. The full width half maximum (FWHM) is 0.365^o. The quality of n-ZnO material deposited by RF sputtering under optimum post annealing is suitable to be the n-type layer of n-ZnO/p-GaN LEDs.

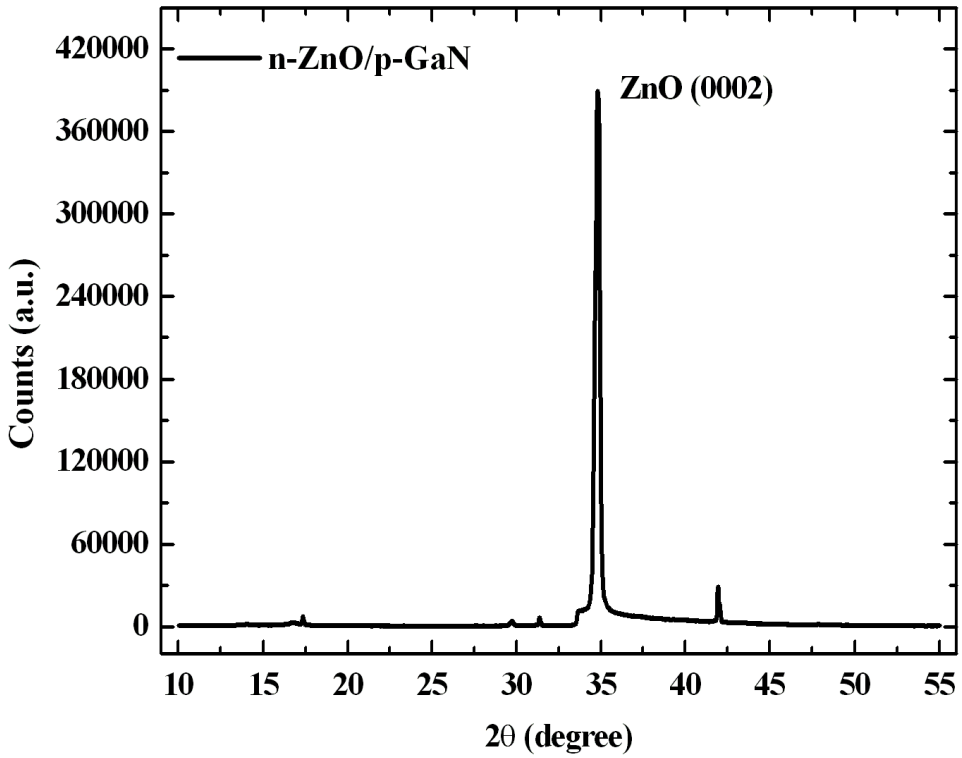

Fig. A1-3: The XRD indicated the high c-axis orientation (0002) was observed under the anneal condition, 550^{o}C and 30mins.

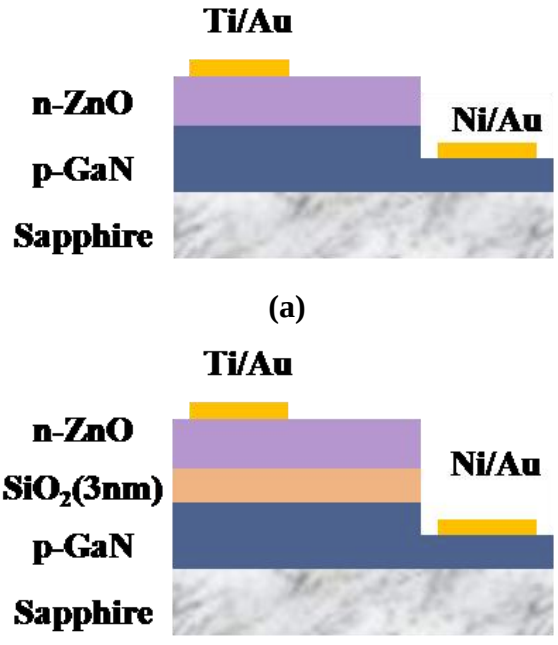

Fig. A1-4: Schematic diagram of n-ZnO/p-GaN (a) and n-ZnO/SiO_2 (3nm)/ p-GaN (b) LEDs, respectively.

A1-3 Device fabrication

The fabrication starts from preparation of a p-type GaN epi-wafer. The p-type GaN layer was grown on top of a sapphire substrate by MOCVD (Metal Organic Chemical Vapor Deposition). The effective carrier concentration in this layer is approximately $5x10^{17}cm^{-3}$ after rapid thermal annealing in N_2 ambient at 750^oC for 30 minutes. In the next step, a patterned SiO_2 layer was coated on top of the p-GaN layer at room temperature, followed by the deposition of a 300 nm heavily doped n-type ZnO at 100^oC, both by RF magnetron sputtering. The 3nm SiO_2 layer is inserted between p- and n-type layers for carrier blocking. We also prepare an LED sample without a SiO_2 layer for comparison. The sputter target of the n-type ZnO was doped with 0.5wt % Ga. And the n-ZnO layer was annealed at 550^oC for 30 minutes after deposition. Finally, Ni/Au and Ti/Au were evaporated as the p-type and n-type contact electrodes, respectively. They were alloyed for optimum contact conditions. Two kinds of samples, n-ZnO/p-GaN and n-ZnO/SiO_2/p-GaN, were listed in the Fig. A1-4 (a) and (b), respectively.

A1-4 Characteristics of n-ZnO/p-GaN LEDs

A1-4-1 Photoluminescence (PL)

We first perform room temperature PL measurement on a sputtered n-ZnO thin film as well as a p-GaN sample by a He-Cd laser operating at 325nm. As shown in Fig. A1-5, the PL spectrum of the n-ZnO shows a near-band-edge (NBE) emission at 379 nm and a wide green band at 503 nm. Green luminescence has been reported to be due to oxygen vacancy related defects in the crystallite surface [111]. Despite the fact that the intensity ratio between defect related and NBE emission is higher than other approaches like PLD (Pulse Laser Deposition) or CVD (Chemical Vapor Deposition) due to the low temperature sputtering process, the sharp excitonic peak at 379nm suggests that the material property is suitable for light emitting devices. In contrast, the PL spectrum of the p-GaN film reveals an intense deep level emission at around 430 nm, which can be attributed to the transmission from the conduction band or shallow donors to the Mg accepted doping level [112].

A1-4-2 Electrical characteristics (I-V)

Fig. A1-6 shows current-voltage (IV) curves of n-ZnO/p-GaN heterojunction LEDs with and without a SiO_2 current blocking layer. Both samples demonstrate a nonlinear rectifying behavior while an additional voltage drop across the SiO_2 layer is observed

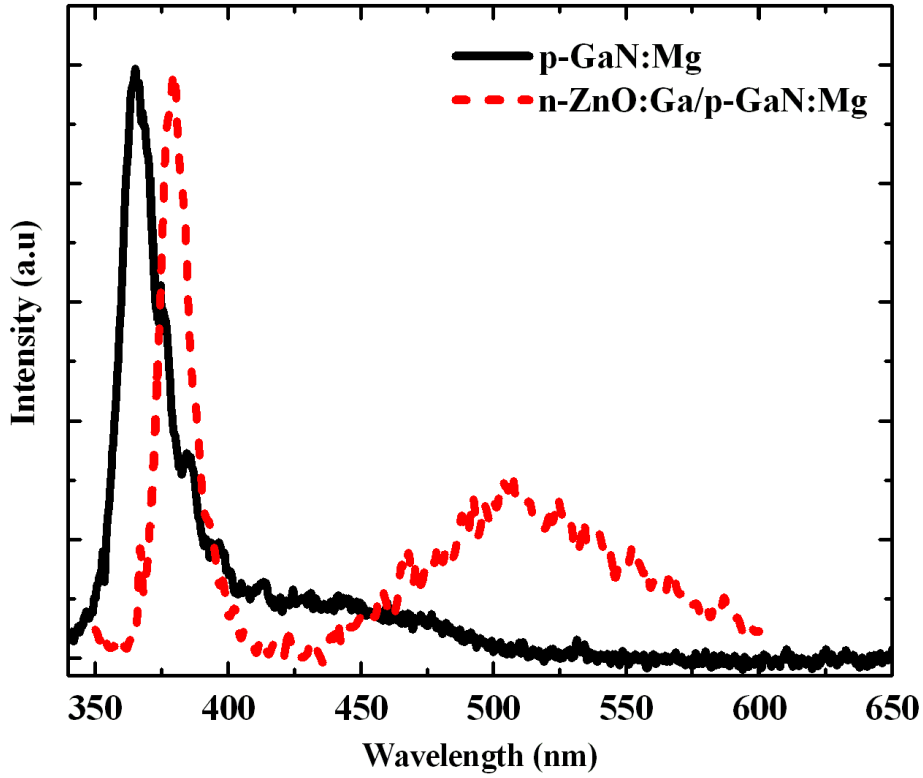

Fig. A1-5: PL spectra of RF sputtered n-ZnO (dashed line) and MOCVD grown p-GaN (solid line)

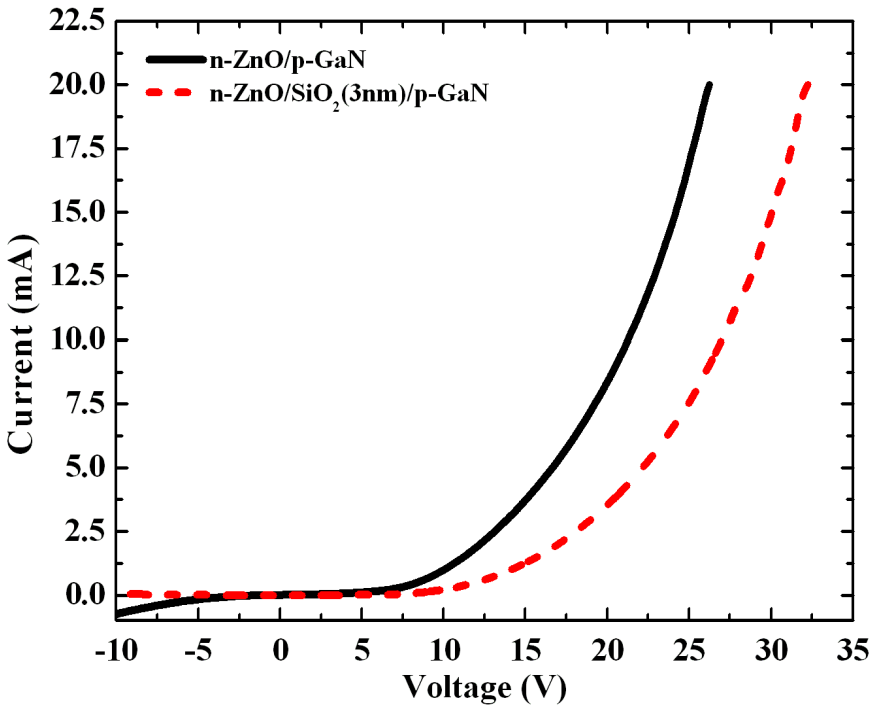

Fig. A1-6: I-V curves of a n-ZnO/p-GaN LED (solid line) and a n-ZnO/SiO_2 (3nm)/p-GaN LED (dashed line).

from the n-ZnO/SiO_2/p-GaN device. The Fig. A1-7 showed the ohmic-like characteristic for the contact between n-ZnO and Ti/Au, the contact between p-GaN and Ni/Au showed the non perfect ohmic behavior due to the non optimum annealing condition. The annealing condition of p- and n- metal pads are listed in the Table A1-1. From the Fig. A1-6, we could observe the large threshold voltage of both samples and is related to the non optimum behavior of contact between the contact electrode and the p-GaN layer.

A1-4-3 Electroluminescence (EL) of light emitting diodes (LEDs)

A. The effect of rapid temperature anneal (RTA) process for the n-ZnO/p-GaN heterojunction LEDs

In this section, we discuss the mechanism of electroluminescence with and without rapid temperature anneal (RTA) in n-ZnO/p-GaN heterojunction LEDs. In the Fig. A1-8, we proposed the EL spectrum of n-ZnO/SiO_2/p-GaN heterojunction LEDs with and without rapid temperature annealing (RTA) on Ti/Au and n-ZnO. Before the metal RTA, EL spectrum (black solid rectangular) showed the higher green band emission nearby the wavelength of 509nm. The sample without RTA process has higher green band emission and is due to the higher possibilities for the recombination of V_o in n-ZnO material. After the RAT process, contact behavior of metal pad and ZnO possessed the

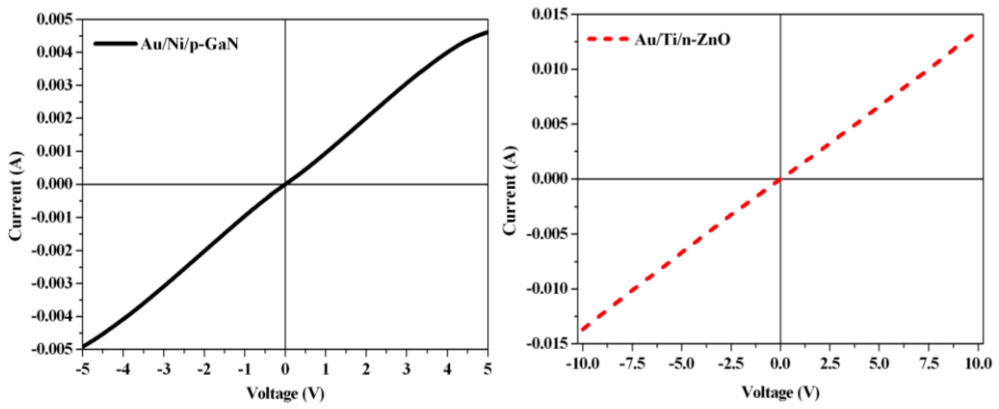

(a) **(b)**

Fig. A1-7: The current voltage curve of Ni/Au on p-GaN (a) and Ti/Au on n-ZnO (b) were indicated the ohmic-like behavior under optimum post anneal condition.

Activation Temperature	350°C	450°C	550°C
UV Emission	Low	Medium	High
Green and Yellow emission	Low	High	Medium

◆ **Annealing Conditions:**

Ni/Au on p-GaN: 500°C for 5mins under N_2 ambient condition.

Ti/Au on n-ZnO: 600°C for 30sec under N_2 ambient condition.

Table A1-1: The table showed the PL emission information under different activation temperature and annealing conditions.

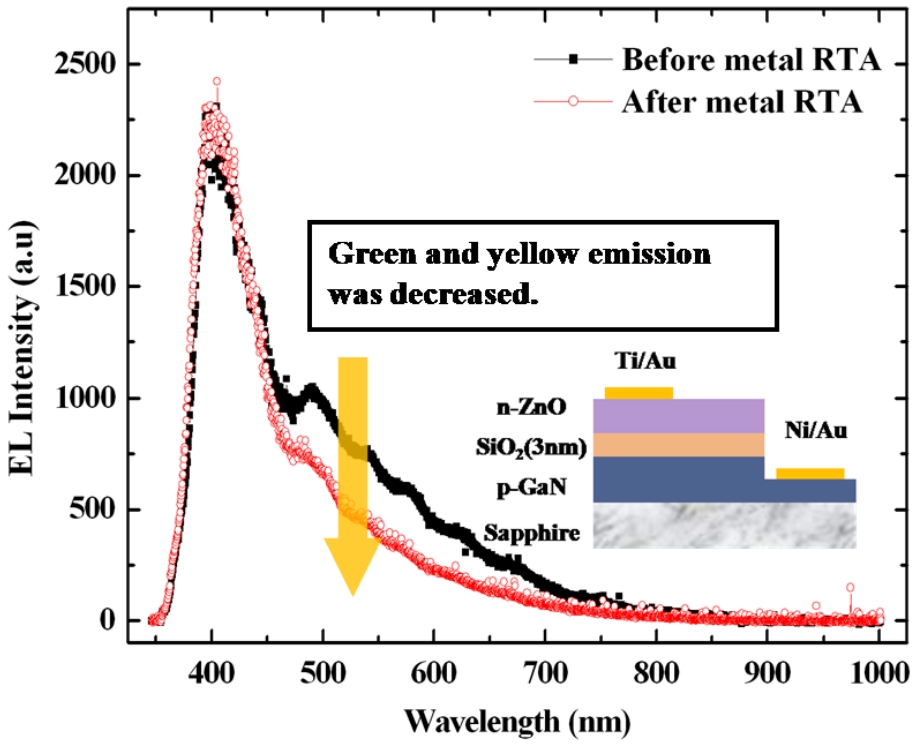

Fig. A1-8: EL spectrum of n-ZnO/SiO_2/p-GaN LEDs before (black solid rectangular) and after (red hollow circle) rapid temperature annealing (RTA).

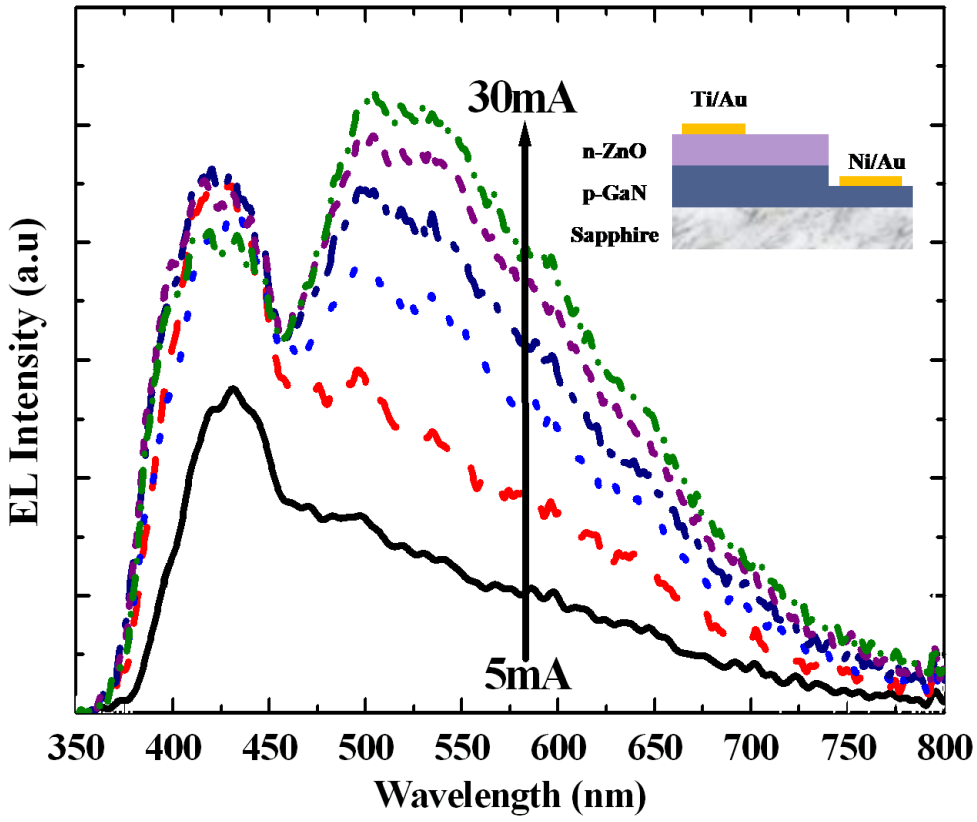

Fig. A1-9: (a) EL spectra of a n-ZnO/p-GaN LED. The bias current ranges from 5mA to 30mA at a step 5mA.

better contact quality and is contributed to the better near UV EL emission.

B. Electroluminescence (EL) of n-ZnO/p-GaN LEDs with and without SiO_2 current blocking layer

The EL spectra of LEDs devices with and without SiO_2 current blocking layers are shown in Fig. A1-9 (a) and (b), respectively. For the LED without a current blocking layer, a wide- band emission between 400 nm to 800 nm can be seen. By comparing the EL curves in Fig. A1-9(a) with PL spectra in Fig. A1-5, it is suggested that emission peaks between 421nm and 438nm result from deep level carrier recombination (Mg^{+}) in the p-GaN layer while long tails are due to oxygen vacancies (V_o) in the n-ZnO layer. As the injection current is increased, a blue shift is noted which is related to band filling in the p-GaN layer [112]. As for the EL spectra of the sample with a SiO_2 layer, the emission maximum starts from 421nm at a low injection current 5mA, which, by comparing with the spectra in Fig. A1-5 and Fig. A1-9(a), indicates that recombination occurs in the p-GaN layer. When we further raise the bias voltage to a point that enough electrons and holes accumulate in the interface of n-ZnO/SiO_2 and p-GaN/SiO_2, respectively, recombination between n-ZnO and p-GaN by carriers through the SiO_2 can be found from the EL peak at 394nm. Therefore, the emission peak shifts from 421nm at 5mA to 394nm at injection currents above 10mA. And then no significant

wavelength shift can be observed for currents beyond 10mA.

C. Discussion of band diagram on the mechanism of carrier recombination

The emission at an optical energy lower than the NBE of n-ZnO can be described from the band diagram constructed from Anderson model [89]. In the diagram of Fig. A1-10, the electron affinity χ_{ZnO}, χ_{SiO2} and χ_{GaN} are taken as 4.35 eV, 1.1 eV and 4.20 eV, respectively. The bandgap of n-ZnO, SiO_2 and GaN are 3.37 eV, 8.90 eV and 3.40 eV. The energy barrier for ΔE_C and ΔE_V in the interface of n-ZnO/SiO_2 and p-GaN /SiO_2, determined from electron affinity and bandgap, is 3.24 eV and 2.5 eV, respectively. Therefore, the EL emission peak is shifted toward a longer wavelength due to the band offset at the valence of p-GaN. The result implies that with the insertion of a current blocking layer between n and p layers, the emission wavelength can be controlled by selecting different bandgap structures in both the n-type and p-type layers.

D. Electrical luminescence of device with different thickness of SiO_2 current blocking layer

We further extend the thickness of SiO_2 layers to 6 and 9 nm. Figure A1-11 demonstrates the EL spectra of samples with 0, 3, 6, and 9 nm thickness of SiO_2 layers biased at an injection current of 20 mA. All the samples have the same layout structure

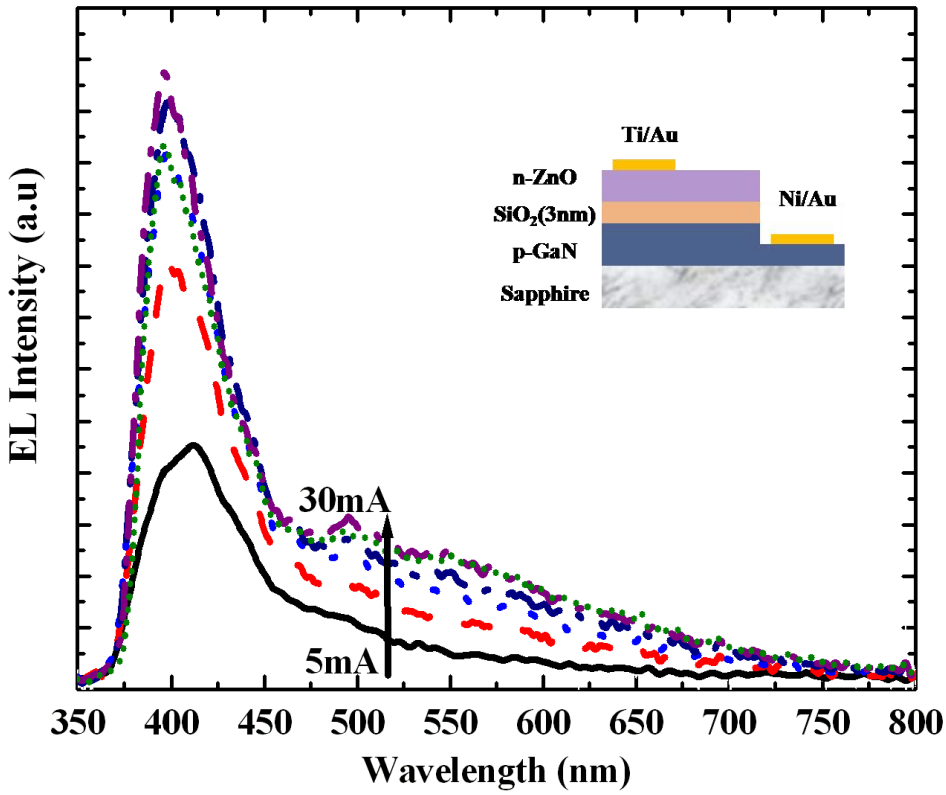

Fig. A1-9: EL spectra of and a n-ZnO/SiO_2(3nm)/p-GaN LED. The bias current ranges from 5mA to 30mA at a step 5mA.

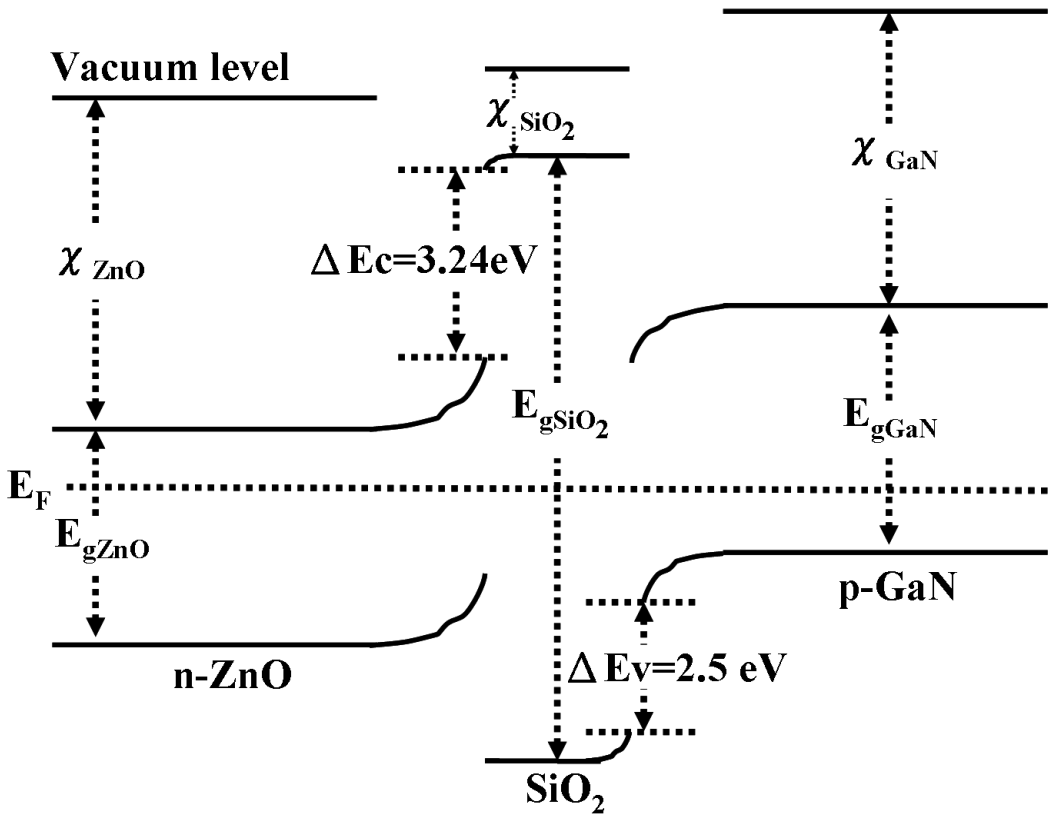

Fig. A1-10: Bandgap diagram of the n-ZnO/SiO_2/p-GaN structure.

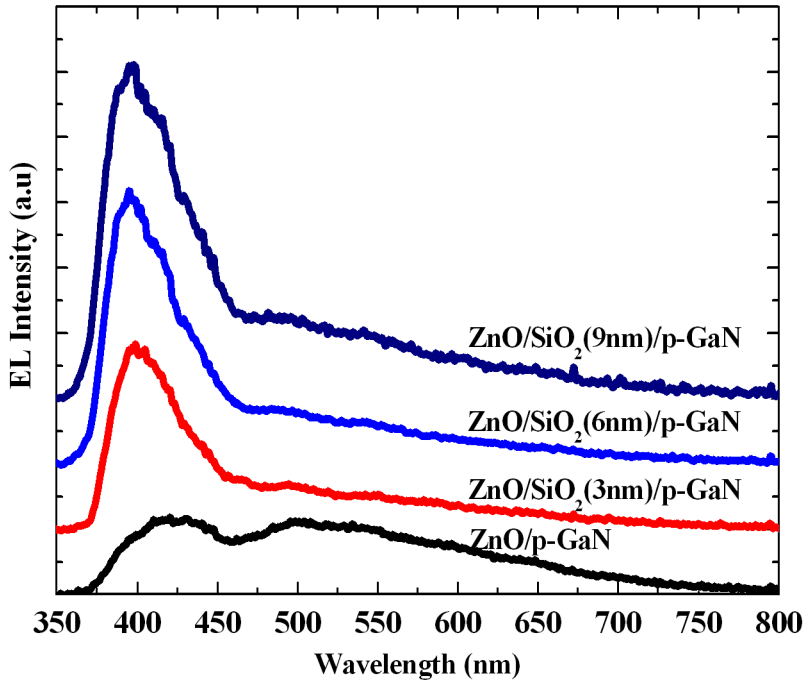

Fig. A1-11: EL spectra of n-ZnO/SiO_2/p-GaN LEDs with different SiO_2 thicknesses. The bias current is 20mA.

and *p*-type mesa area of 300×300μ m^2. It is shown that the emission maximum occurs at 394 nm for the sample with a blocking layer and at 421 nm for the *n*-ZnO/*p*-GaN sample. Also, we have noticed that the relative intensity of the *n*-ZnO/ *p*-GaN sample is much weaker than that of samples with the SiO_2 layer. The quantum efficiency, calculated from the EL spectra at 20 mA, of sample with 3, 6, and 9 nm SiO_2 is 7.6%, 24.5%, and 57.2%, respectively, higher than that of a *n*-ZnO/*p*-GaN device. It indicates that the SiO_2 layer helps confine carriers for the recombination between junctions of *n*-ZnO/SiO_2 and SiO_2 /*p*-GaN, and, thus, less carriers are consumed in the *n*-ZnO or *p*-GaN layer despite subpeaks at 421 and 503 nm can still be observed for devices with SiO_2. By comparing the EL spectra of the device without SiO2, those humps are related to carrier recombination in the *n*-ZnO and *p*-GaN layers. In this experiment, we also fabricated a sample with 12 nm SiO2 layer. But unfortunately the required bias voltage is too large to be of practical measurement.

A1-5 Conclusions

In conclusion, n-ZnO/p-GaN heterojunction light emitting diodes were successfully fabricated and emitted the near UV light at 394nm by inserting the SiO_2 current blocking layer. The n-ZnO and SiO_2 thin films were deposited by the RF sputtering at low temperature. From the material analysism PL and XRD, The quality of

n-ZnO deposited by RF sputtering is suitable for the application of light emitting diodes (LEDs). We compare samples with and without a SiO_2 current blocking layer. The I-V curve showed the large drop of bias voltage which is due to the existence of thin SiO_2 layer. However, EL spectrum shows a sharp emission peak at 394 nm with a SiO_2 thin film layer. The 394nm peak is attributed to the recombination of accumulated carriers between n-ZnO/SiO_2 and p-GaN/SiO_2 junctions. As for the sample without a SiO_2 layer, only the 400-800 nm broad band is observed, which is due to Mg^+ deep-level transition in the p-GaN and defects related recombination in the n-ZnO layers. Finally, the green-yellow broad band emission could be effectively compressed through process of high temperature annealing and this concept of the insertion of current blocking layer could be applied on the investigation of ZnO based light emitting diodes (LEDs).

Appendix 2

Photoresponse of heterojunction photodetectors by RF sputtering n-ZnO on p-GaN/sapphire

We successfully fabricated the n-ZnO/p-GaN LEDs with the SiO_2 current blocking layer and observed the 394nm emission which is due to the interface transition between n-ZnO/SiO_2 and SiO_2/p-GaN in previous chapter. The other advantage for ZnO material is the fabrication of UV detector for the application of space communications, ozone layer monitoring and flame detection. The characterizations of n-ZnO/p-GaN photodetector were investigated in this chapter. And, the combination of n-ZnO and p-GaN could result in the purified UV band absorption and possess the high UV to visible rejection ratio of photoresponsivity. In this chapter, the photoresponse of an n-ZnO/p-GaN photodiode shows a maximum responsivity 0.009A/W at 370nm and a UV (370nm) to visible (450nm) wavelength rejection ratio as high as 51.6. The absorption of the n-ZnO/p-GaN photodiode is contributed by the absorption of both n-ZnO and p-GaN thin films, the slight band offset of the n-ZnO/p-GaN heterojunction and the deep level absorption from p-GaN. Thus, the absorption band of photodiodes can be adjusted simply by adjusting the metal composition of a binary metal oxide thin film on p-GaN.

A2-1 Motivations

In this chapter, a high UV-to-visible photoresponse rejection ratio of ZnO based heterojunction p-n photodiode is demonstrated by RF sputtering an n-type ZnO layer on top of the p-type GaN. The fabrication of n-ZnO/p-GaN photodiodes will be described. And then material properties of n-ZnO are characterized by comparing the X-ray diffraction (XRD) patterns of ZnO thin films grown on either GaN or Si. Finally the photoresponse and band diagram of n-ZnO/p-GaN photodiodes will be discussed.

A2-2 Device fabrication

The fabrication started from preparation of a p-type GaN epi-wafer. The p-type GaN layer was grown on top of a sapphire substrate by metal organic chemical vapor deposition (MOCVD). The effective carrier concentration in this layer is $5\times10^{17}cm^{-3}$ after 30 minutes of p-GaN activation at 750^{o}C. In the next step, we deposited a 300nm heavily doped n-type ZnO on top of the p-GaN layer by RF magnetron sputtering at an oxygen pressure 15 mTorr. The chamber temperature was kept at 100^{o}C and during the deposition. The sputter target of the n-type ZnO was doped with 0.5wt% Ga. The effective n-type carrier concentration after 550^{o}C 30 minutes post deposition annealing is approximately $2\times10^{18}cm^{-3}$. Finally, Ni/Au(12nm/120nm) and Ti/Au (12nm/120nm) were evaporated as the p-type and n-type contact electrodes, respectively.

They were separately alloyed to achieve optimum contact conditions. The n-ZnO area for light illumination is $300\times300\mu\ m^2$.

A2-3 Characteristics of n-ZnO/p-GaN photodetectors

A. Electrical characteristics (I-V)

Dark and UV illuminated current-voltage (I-V) curves of the n-ZnO/p-GaN heterojunction diode are characterized by Agilent 4155C semiconductor parameter analyzer and are shown in Fig. A2-1(a). A nonlinear rectifying behavior can be observed with a forward/reverse current ratio 648 at ±10V. As shown in the Fig. A2-1(b) and (c), the I-V characteristic is linear for Ti/Au contacts on n-ZnO and Ni/Au on p-GaN, indicating formation of ohmic-like behavior on both p- and n- layers under the same condition of thermal annealing reported in Appendix 1. The leakage current at a bias voltage of -5V is 84.1pA ($93nA/cm^2$), which is much lower than previous reported leakage currents of n-ZnO/p-Si photodiodes [79, 85, 113]. As we illuminate the device from the ZnO side with an optical power of 3mW at wavelength 370nm, the photocurrent is significantly higher than the dark current. At the bias voltage -5V, we achieve a photocurrent around three orders of magnitude larger than the dark current in Fig. A2-1(a).

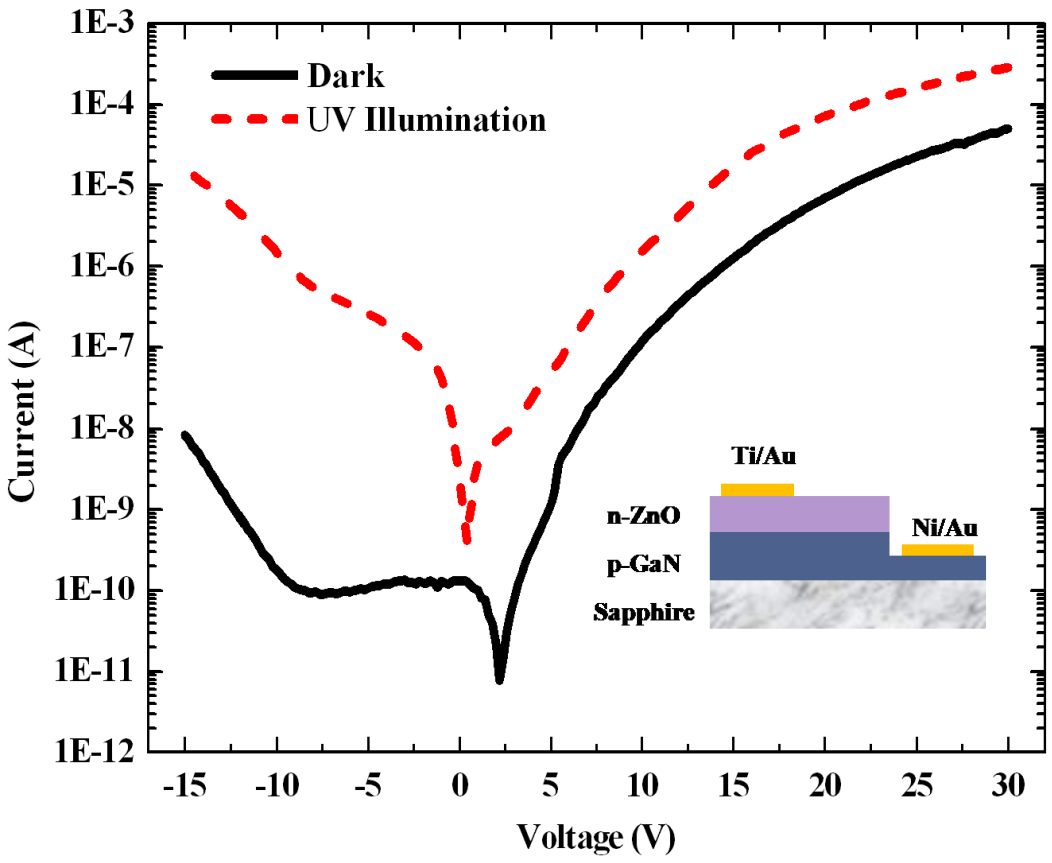

(a)

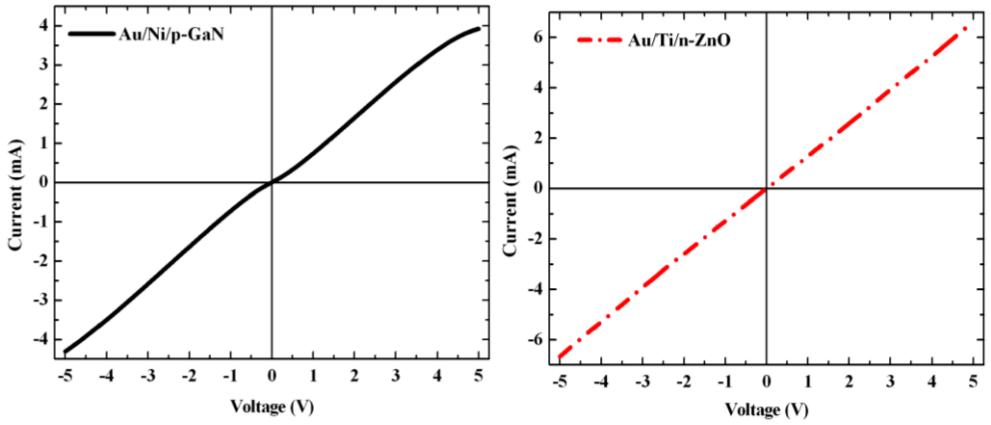

(b) (c)

Fig. A2-1: Dark (black solid line) and UV-illuminated (red dashed line) I-V curves of the n-ZnO/p-GaN photodiode (a), the current voltage diagrams of Ni/Au on p-GaN (b) and Ti/Au on n-ZnO (c).

B. Analysis of X-ray diffraction (XRD)

Though the current level of our device is affected by the high resistivity of p-type GaN layer, the low leakage current is mainly related to a better ZnO crystalline quality grown on top of the p-GaN layer as both semiconductor materials are hexagonal crystal structure with 1.8% lattice mismatch in the c-plane [89]. The less lattice mismatch of our n-ZnO/p-GaN photodiode implies less junction defects in the ZnO and GaN interface. Thus the leakage current can be significantly reduced. To verify the crystal property, we examine XRD patterns of a sample with a 300nm n-type ZnO layer sputtered on top of the p-GaN (sample A) layer. We also prepare a sample with n-ZnO sputtered on p-Si substrate (sample B) for comparison purpose. In Fig. A2-2, the diffraction peak of sample A is higher than that of sample B. In addition, the full width at half maximum (FWHM) of sample A and B is 0.57^{o} and 0.76^{o}, respectively. Since both ZnO and GaN are wurzite structure while Si is diamond structure, the results suggest that the crystalline quality of ZnO sputtered on top of GaN is better than that of ZnO on Si.

C. Photocurrent under different power of incident light

From the principle of photodetector, we could understood that lower light power could cause lower photocurrent at the same device. It could be ascribed as below

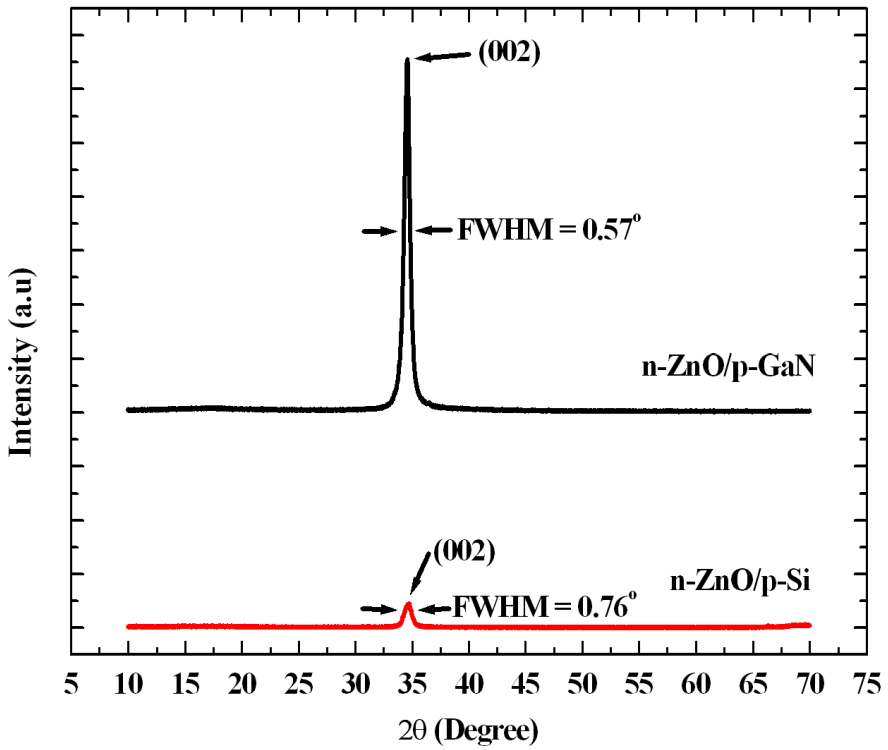

Fig. A2-2: Room temperature XRD spectra of sample A (n-ZnO on p-GaN) and sample B (n-ZnO on p-Si) under the same activated condition, 550°C for 30mins.

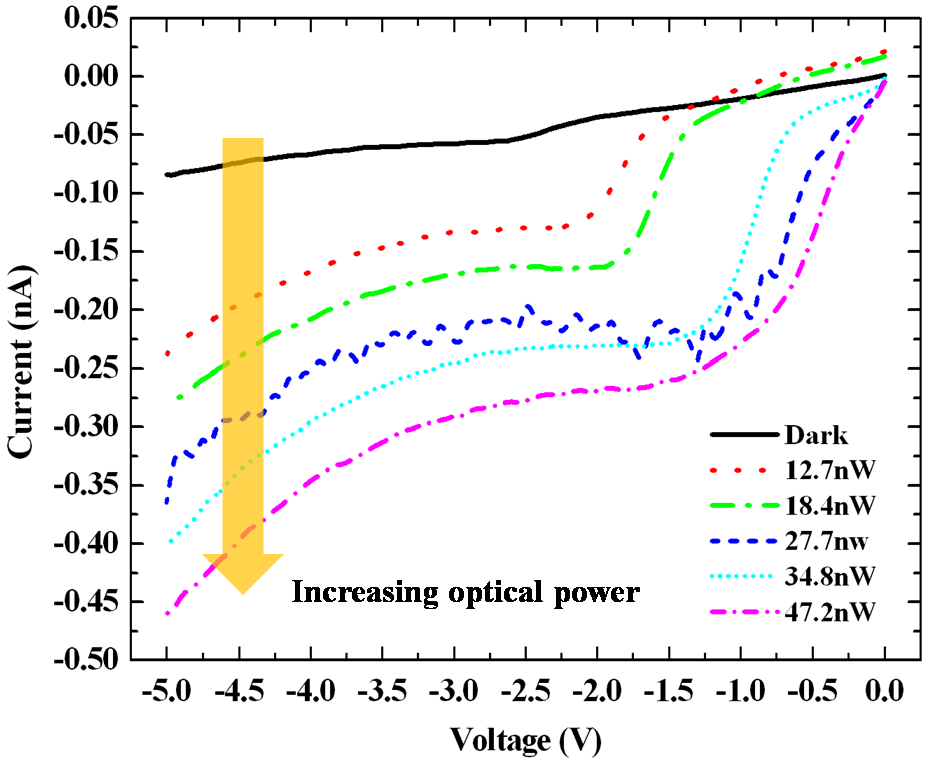

Fig. A2-3: The current-voltage curve of n-ZnO/p-GaN photodetector under different optical powers at 375nm.

equation.

$$R_S = \frac{I_O}{P_O} \text{ (A/W)}$$

We could observed the behavior of our devices, in Fig. A2-3, following the basic principle of photodetector. When we increased the power of incident light, the photocurrent was increased to larger values. However, we didn't observe the obvious short circuit current (I_{sc}) in n-ZnO/p-GaN photodetector under zero bias in Fig. A2-3. It could be attributed to the non-perfect interface quality between the metal contact of Ni/Au and p-GaN leading to the smaller short circuit current (I_{sc}).

D. The photoresponsivity of n-ZnO/p-GaN photodiodes

The measured spectral responsivity of the n-ZnO/p-GaN photodetector is shown in Fig. A2-4. The device is biased at a voltage of -5V and is illuminated from the ZnO side. It is found that the maximum responsivity 0.009A/W is obtained at the UV band 370nm. The rejection ratio is around 51.6 by comparing the responsivities at wavelength 370nm and 450nm. Again, the high UV to visible wavelength rejection ratio of the n-ZnO/p-GaN diodes as compared with other ZnO based heterojunction devices is attributed to the low leakage current of the device, which is related to less lattice mismatch between ZnO and GaN. For most Schottky or MSM ZnO photodiodes, the sharp cutoff wavelength at around 370nm is attributed to the

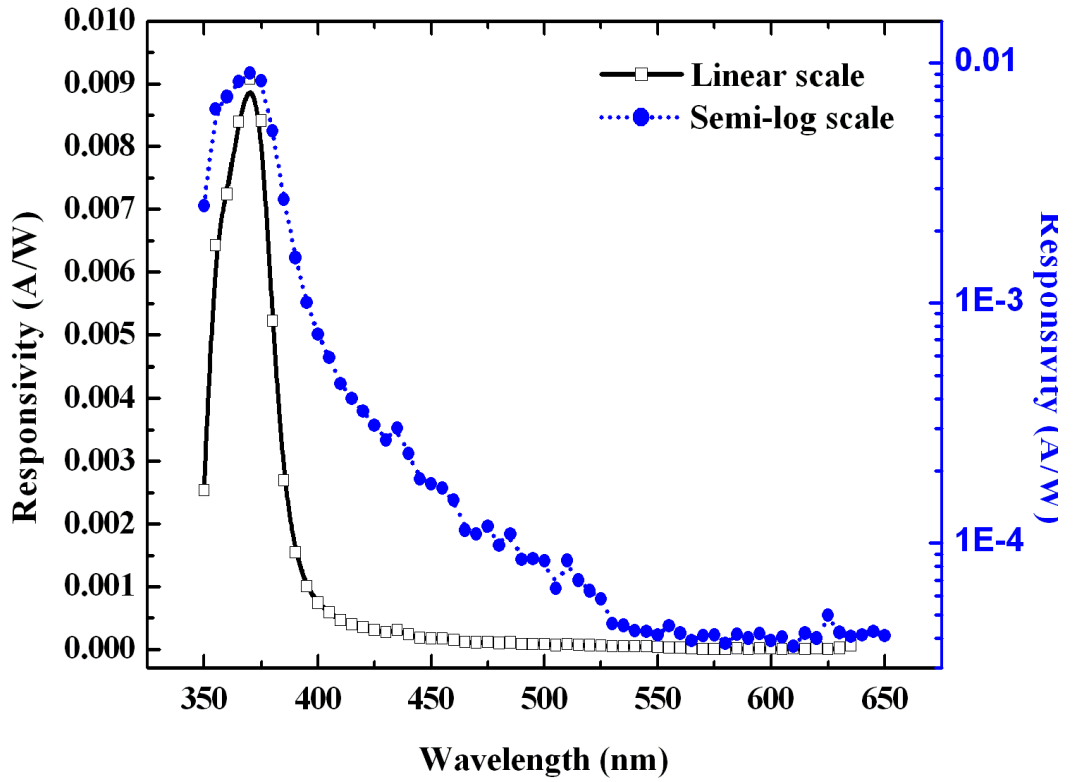

Fig. A2-4: Measured spectral responsivity of n-ZnO/p-GaN photodiodes. The device is biased at -5V.

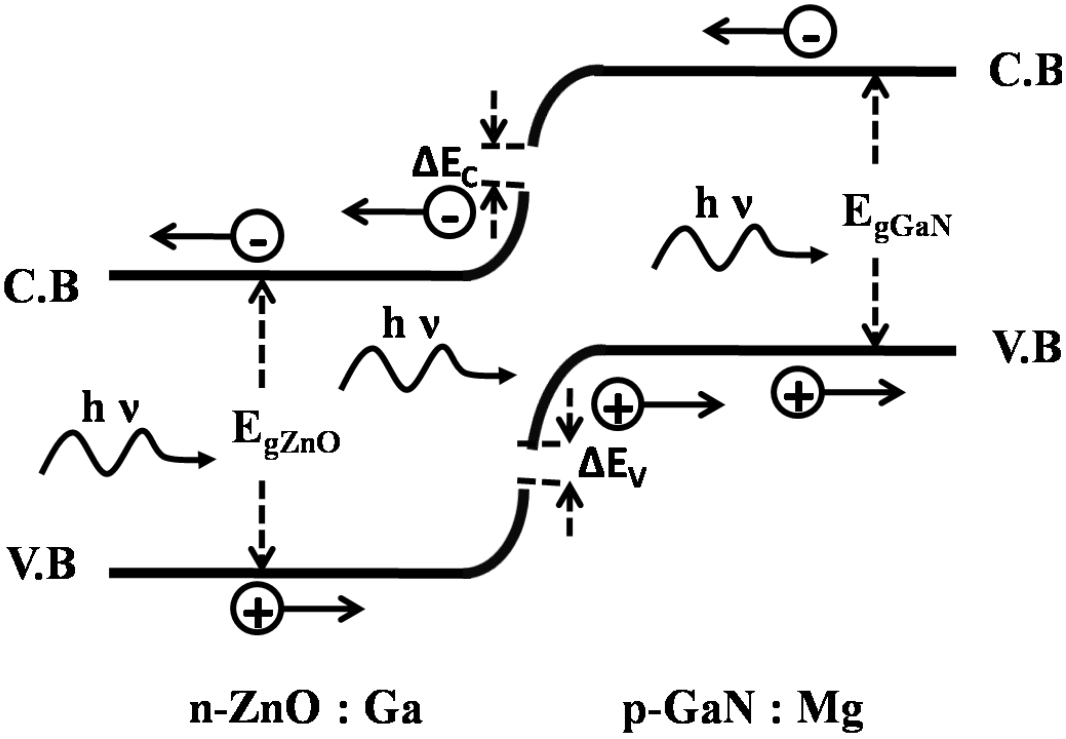

Fig. A2-5: Bandgap diagram of the n-ZnO/p-GaN heterostructure.

absorption band edge of ZnO [90, 114]. However, the drop of the spectral responsivity curve from UV to visible wavelength of our p-n heterojunction device is ascribed to the absorption of both ZnO (E_g=3.37eV) and GaN (E_g=3.40eV) as well as the slight band offset of the ZnO/GaN heterojunction.

E. Discussion on the band diagram of n-ZnO/p-GaN photodiodes

To understand the photoresponse behavior of the n-ZnO/p-GaN photodetector, we draw the energy band diagram of the n-ZnO/p-GaN heterostructure using the Anderson model [89]. As illustrated in Fig. A2-5, the energy barrier ΔE_C and ΔE_V in the interface of n-ZnO/p-GaN, determined from the electron affinity and the band gap, is 0.15eV and 0.12eV, respectively [89]. Therefore, UV photons with energy slightly lower than the band edge of n-ZnO and p-GaN can still be absorbed in the n-ZnO/ p-GaN interface. The responsivity curve in Fig. A2-4 is composed of the following absorption mechanisms. First, the maximum of the responsivity between 350nm and 380nm is contributed by the absorption band edges of both n-ZnO and p-GaN. And the tail that extends from 380nm to 400nm is related to the band offset in the interface of the n-ZnO and p-GaN. Also, for p-GaN semiconductor, the intense deep level absorption centered at around 430nm can be observed from the responsivity curve due to the transmission from the conduction band or shallow donors to the Mg acceptor

doping level [109]. The electron-hole pair generations are illustrated in Fig. A2-5. Furthermore, from the analysis of the absorption band, one of the advantages of our device structure is that the absorption band of photodiodes can be adjusted simply by adjusting the metal composition of a binary metal oxide, such as InZnO or AlZnO, thin film on GaN.

A2-4 Conclusions

The ZnO based heterojunction p-n photodiode is demonstrated by RF sputtering an n-type ZnO layer on top of the p-type GaN layer. The device shows a low leakage current which mainly results from a better ZnO crystalline quality grown on the p-GaN layer as both n-ZnO and p-GaN semiconductor materials are hexagonal crystal structure with 1.8% lattice mismatch in the c-plane. The photoresponse of an n-ZnO/p-GaN photodiode shows a maximum responsivity 0.009A/W at 370nm and a UV (370nm) to visible (450nm) wavelength rejection ratio as high as 51.6. The absorption of the n-ZnO/p-GaN photodiode is contributed by the absorption of both n-ZnO and p-GaN thin films, the slight band offset of the n-ZnO/p-GaN heterojunction and the deep level absorption from p-GaN. Thus, the absorption band of photodiodes can be adjusted simply by adjusting the metal composition of a binary metal oxide thin film on p-GaN.

Reference

1. Green, M.A., *The path to 25% silicon solar cell efficiency: history of silicon cell evolution.* Progress in Photovoltaics, 2009. **17**(3): p. 183-189.
2. Bauhuis, G.J., et al., *Thin film GaAs solar cells with increased quantum efficiency due to light reflection.* Solar Energy Materials and Solar Cells, 2004. **83**(1): p. 81-90.
3. Zhu, J., et al., *Optical absorption enhancement in amorphous silicon nanowire and nanocone arrays.* Nano Letters, 2009. **9**(1): p. 279-282.
4. Green, M.A., et al., *Solar cell efficiency tables (version 33).* Progress in Photovoltaics, 2009. **17**(1): p. 85-94.
5. Takamoto, T., et al., *Over 30% efficient InGaP/GaAs tandem solar cells.* Applied Physics Letters, 1997. **70**(3): p. 381-383.
6. Meier, J., et al., *Potential of amorphous and microcrystalline silicon solar cells.* Thin Solid Films, 2004. **451-52**: p. 518-524.
7. Bucher, K., J. Bruns, and H.G. Wagemann, *Absorption-coefficient of silicon - an assessment of measurements and the simulation of temperature-variation.* Journal of Applied Physics, 1994. **75**(2): p. 1127-1132.
8. Yoshida, N., et al., *A study of absorption coefficient spectra in a-Si : H films near the transition from amorphous to crystalline phase measured by resonant photothermal bending spectroscopy.* Journal of Non-Crystalline Solids, 2008. **354**(19-25): p. 2164-2166.
9. Hadipour, A., B. de Boer, and P.W.M. Blom, *Organic tandem and multi-junction solar cells.* Advanced Functional Materials, 2008. **18**(2): p. 169-181.
10. Dennler, G., et al., *Design rules for donors in bulk-heterojunction tandem solar*

cells-towards 15 % energy-conversion efficiency. Advanced Materials, 2008. **20**(3): p. 579-583.

11. Amano, C., et al., *20.2-percent efficiency $Al_{0.4}Ga_{0.6}As$ GaAs tandem solar-cells grown by molecular-beam epitaxy.* Applied Physics Letters, 1987. **51**(24): p. 1998-2000.
12. Bertness, K.A., et al., *29.5-percent-efficient GaInP/GaAs tandem solar-cells.* Applied Physics Letters, 1994. **65**(8): p. 989-991.
13. Ganguly, G., D.E. Carlson, and R.R. Arya, *Amorphous germanium recombination junctions in amorphous-silicon-based tandem solar cells.* Applied Physics Letters, 2003. **83**(20): p. 4256-4258.
14. Andreev, V.M., et al., *Tandem solar cells based on AlGaAs/GaAs and GaSb structures.* Compound Semiconductors 1996, 1997(155): p. 425-428.
15. Takamoto, T., et al., *26.9% efficient and radiation resistant InGaP/GaAs tandem solar cells.* Compound Semiconductors 1998, 1999(162): p. 853-856.
16. Dimroth, F., U. Schubert, and A.W. Bett, *25.5% efficient $Ga_{0.35}In_{0.65}P$/ $Ga_{0.83}In_{0.17}$ as tandem solar cells grown on GaAs substrates.* IEEE Electron Device Letters, 2000. **21**(5): p. 209-211.
17. Nattestad, A., et al., *Highly efficient photocathodes for dye-sensitized tandem solar cells.* Nature Materials, 2010. **9**(1): p. 31-35.
18. Kim, J.Y., et al., *Efficient tandem polymer solar cells fabricated by all-solution processing.* Science, 2007. **317**(5835): p. 222-225.
19. Yamaguchi, M., *Physics and technologies of superhigh-efficiency tandem solar cells.* Semiconductors, 1999. **33**(9): p. 961-964.
20. Beaumont, B., et al., *$Ga_{0.47}$ $In_{0.53}$ as Photovoltaic Booster Cells for Tandem Solar-Energy Conversion.* Solar Cells, 1989. **26**(4): p. 313-321.

21. Dharmadasa, I.M., *Third generation multi-layer tandem solar cells for achieving high conversion efficiencies.* Solar Energy Materials and Solar Cells, 2004. **85**(2): p. 293-300.

22. Hein, M., et al., *Characterization of a 300X photovoltaic concentrator system with one-axis tracking.* Solar Energy Materials and Solar Cells, 2003. **75**(1-2): p. 277-283.

23. Zhu et al, *Nanodome solar cells with efficient light management and self-cleaning.* Nano Lett., 2009. **http://www.stanford.edu/group/cui_group/papers/nl9034237.pdf**.

24. Chen, C.P., et al., *Nanoparticle-coated n-ZnO/p-Si photodiodes with improved photoresponsivities and acceptance angles for potential solar cell applications.* Nanotechnology, 2009. **20**(24): p.245204-1 -245204-6.

25. Matsui, H., et al., *Correlation between micro-roughness, surface chemistry, and performance of crystalline Si/amorphous Si : H : Cl hetero-junction solar cells.* Journal of Non-Crystalline Solids, 2008. **354**(19-25): p. 2483-2487.

26. Krc, J., et al., *Effect of surface roughness of ZnO : Al films on light scattering in hydrogenated amorphous silicon solar cells.* Thin Solid Films, 2003. **426**(1-2): p. 296-304.

27. Campbell, P.R. and M.A. Green, *On intensity enhancement in textured optical sheets for solar-cells.* IEEE Transactions on Electron Devices, 1986. **33**(11): p. 1834-1835.

28. Derrick, G.H., R.C. Mcphedran, and D.R. Mckenzie, *Theoretical-studies of textured amorphous-silicon solar-cells.* Applied Optics, 1986. **25**(20): p. 3690-3696.

29. Campbell, P., *Light trapping in textured solar-cells.* Solar Energy Materials,

1990. **21**(2-3): p. 165-172.

30. Takato, H., et al., *Effects of optical confinement in textured antireflection coating using ZnO films for solar-cells*. Japanese Journal of Applied Physics Part 2-Letters, 1992. **31**(12A): p. L1665-L1667.

31. Zhao, J.H., et al., *19.8% efficient "honeycomb" textured multicrystalline and 24.4% monocrystalline silicon solar cells.* Applied Physics Letters, 1998. **73**(14): p. 1991-1993.

32. Spiegel, M., et al., *Industrially attractive front contact formation methods for mechanically V-textured multicrystalline silicon solar cells.* Solar Energy Materials and Solar Cells, 2002. **74**(1-4): p. 175-182.

33. Springer, J., et al., *Light trapping and optical losses in microcrystalline silicon pin solar cells deposited on surface-textured glass/ZnO substrates.* Solar Energy Materials and Solar Cells, 2005. **85**(1): p. 1-11.

34. Hupkes, J., et al., *Surface textured MF-sputtered ZnO films for microcrystalline silicon-based thin-film solar cells.* Solar Energy Materials and Solar Cells, 2006. **90**(18-19): p. 3054-3060.

35. Muhida, R., et al., *Relationship between average slope of textured substrate and poly-Si thin film solar cells performance.* Materials Research Innovations, 2009. **13**(3): p. 246-248.

36. Kumar, P., et al., *Microcrystalline single and double junction silicon based solar cells entirely prepared by HWCVD on textured zinc oxide substrate.* Journal of Non-Crystalline Solids, 2006. **352**(9-20): p. 1855-1858.

37. Mase, T., et al., *Amorphous-silicon solar-cells on textured aluminum substrate prepared by electrical etching.* Solar Cells, 1986. **17**(2-3): p. 191-200.

38. Koida, T., H. Fujiwara, and M. Kondo, *High-mobility hydrogen-doped In_2O_3*

transparent conductive oxide for a-Si:H/c-Si heterojunction solar cells. Solar Energy Materials and Solar Cells, 2009. **93**(6-7): p. 851-854.

39. Koida, T., H. Fujiwara, and M. Kondo, *Reduction of optical loss in hydrogenated amorphous silicon/crystalline silicon heterojunction solar cells by high-mobility hydrogen-doped In_2O_3 transparent conductive oxide.* Applied Physics Express, 2008. **1**(4): p. 041501-1-041501-3.

40. Kawashima, T., et al., *FTO/ITO double-layered transparent conductive oxide for dye-sensitized solar cells*. Journal of Photochemistry and Photobiology a-Chemistry, 2004. **164**(1-3): p. 199-202.

41. Alamri, S.N. and A.W. Brinkman, *The effect of the transparent conductive oxide on the performance of thin film CdS/CdTe solar cells.* Journal of Physics D-Applied Physics, 2000. **33**(1): p. L1-L4.

42. Plattner, R., W. Stetter, and P. Kohler, *Transparent conductive tin-oxide layers for thin-film solar-cells*. Siemens Forschungs-Und Entwicklungsberichte-Siemens Research and Development Reports, 1988. **17**(3): p. 138-146.

43. Gubbala, S., et al., *Surface properties of SnO_2 nanowires for enhanced performance with dye-sensitized solar cells.* Energy & Environmental Science, 2009. **2**(12): p. 1302-1309.

44. Liu, J.P., et al., *Organic/inorganic hybrid solar cells with vertically oriented ZnO nanowires.* Applied Physics Letters, 2009. **94**(17): p. 173107-1-173107-3.

45. Jeon, M. and K. Kamisako, *Synthesis and characterization of silicon nanowires using tin catalyst for solar cells application.* Materials Letters, 2009. **63**(9-10): p. 777-779.

46. Boercker, J.E., E. Enache-Pommer, and E.S. Aydil, *Growth mechanism of titanium dioxide nanowires for dye-sensitized solar cells.* Nanotechnology, 2008.

19(9): p. 095604-1-095604-10.

47. Tian, B.Z., et al., *Coaxial silicon nanowires as solar cells and nanoelectronic power sources.* Nature, 2007. **449**(7164): p. 885-U8.

48. Lok, C., *Nanowire solar cells - Building photovoltaics out of nanowires.* Technology Review, 2005. **108**(9): p. 85-86.

49. Dmitruk, N.L., A.V. Korovin, and I.B. Mamontova, *Efficiency enhancement of surface barrier solar cells due to excitation of surface plasmon polaritons.* Semiconductor Science and Technology, 2009. **24**(12): p. 125011-1-125011-7.

50. Losurdo, M., et al., *Enhanced absorption in Au nanoparticles/a-Si:H/c-Si heterojunction solar cells exploiting Au surface plasmon resonance.* Solar Energy Materials and Solar Cells, 2009. **93**(10): p. 1749-1754.

51. Akimov, Y.A., K. Ostrikov, and E.P. Li, *Surface plasmon enhancement of optical absorption in thin-film silicon solar sells.* Plasmonics, 2009. **4**(2): p. 107-113.

52. Chang, Y.C., et al., *Effects of surface plasmon resonant scattering on the power conversion efficiency of organic thin-film solar cells.* Journal of Vacuum Science & Technology B, 2007. **25**(6): p. 1899-1902.

53. Pillai, S., et al., *Surface plasmon enhanced silicon solar cells.* Journal of Applied Physics, 2007. **101**(9): p. 093105-1-093105-8.

54. Derkacs, D., et al., *Improved performance of amorphous silicon solar cells via scattering from surface plasmon polaritons in nearby metallic nanoparticles.* Applied Physics Letters, 2006. **89**(9): p. 093103-1-093103-3.

55. Ishikawa, K., et al., *The photocurrent of dye-sensitized solar cells enhanced by the surface plasmon resonance.* Journal of Chemical Engineering of Japan, 2004. **37**(5): p. 645-649.

56. Vukadinovic, M., et al., *Numerical modelling of trap-assisted tunnelling mechanism in a-Si : H and mu c-Si n/p structures and tandem solar cells.* Solar Energy Materials and Solar Cells, 2001. **66**(1-4): p. 361-367.

57. Litovchenko, V.G., et al., *Multiparticle exciton complexes in semiconductors with a large exciton binding-energy in (ZnO).* Jetp Letters, 1979. **30**(9): p. 544-548.

58. Zhang, J.Y., et al., *Electrically driven ultraviolet lasing behavior from phosphorus-doped p-ZnO nanonail array/n-Si heterojunction.* Applied Physics Letters, 2009. **95**(21): p. 211107-1-211107-3.

59. Chen, S.F., et al., *Preparation, characterization and activity evaluation of p-n junction photocatalyst p-ZnO/n-TiO2.* Applied Surface Science, 2008. **255**(5): p. 2478-2484.

60. Wei, Z.P., et al., *Fabrication of nitrogen doped p-ZnO and ZnO light-emitting diodes on sapphire.* Journal of the Korean Physical Society, 2008. **53**(5): p. 3038-3042.

61. Rogozin, I.V. and M.B. Kotlyarevsky, *Characteristics of nitrogen-doped p-ZnO thin films and ZnO/ZnSe p-n heterojunctions grown on a ZnSe substrate.* Semiconductor Science and Technology, 2008. **23**(8): p. 085008-1-085008-5.

62. Sun, J.C., et al., *Ultraviolet electroluminescence from n-ZnO : Ga/p-ZnO : N homojunction device on sapphire substrate with p-type ZnO : N layer formed by annealing in N2O plasma ambient.* Chemical Physics Letters, 2008. **460**(4-6): p. 548-551.

63. Dutta, M. and D. Basak, *p-ZnO/n-Si heterojunction: Sol-gel fabrication, photoresponse properties, and transport mechanism.* Applied Physics Letters, 2008. **92**(21): p. 212112-1-212112-3.

64. Sun, J.C., et al., *Realization of ultraviolet electroluminescence from ZnO homojunction with n-ZnO/p-ZnO : As/GaAs structure.* Applied Physics Letters, 2007. **90**(12): p. 121128-1-121128-3.

65. Chen, H.C., et al., *UV electroluminescence and structure of n-ZnO/p-GaN heterojunction LEDs grown by atomic layer deposition.* IEEE Journal of Quantum Electronics, 2010. **46**(2): p. 265-271.

66. Chen, C.H., et al., *Electroluminescence from n-ZnO nanowires/p-GaN heterostructure light-emitting diodes.* Applied Physics Letters, 2009. **95**(22): p. 223101-1-223101-3.

67. Chang, S.P., et al., *MBE n-ZnO/MOCVD p-GaN heterojunction light-emitting diode.* Thin Solid Films, 2009. **517**(17): p. 5054-5056.

68. Zhao, L., et al., *A new approach to white light emitting diodes of p-GaN/i-ZnO/ n-ZnO heterojunctions.* Applied Physics B-Lasers and Optics, 2008. **92**(2): p. 185-188.

69. Rogers, D., et al., *Materials characterization of n-ZnO/p-GaN : Mg/c-Al_2O_3 UV LEDs grown by pulsed laser deposition and metal-organic chemical vapor deposition.* Superlattices and Microstructures, 2007. **42**(1-6): p. 322-326.

70. Chen, C.P., et al., *Observation of 394 nm electroluminescence from low-temperature sputtered n-ZnO/SiO2 thin films on top of the p-GaN heterostructure.* Applied Physics Letters, 2007. **91**(9): p. 091107-1-091107-3.

71. Yang, H.S., et al., *Fabrication of hybrid n-ZnMgO/n-ZnO/p-AlGaN/p-GaN light-emitting diodes.* Japanese Journal of Applied Physics Part 1-Regular Papers Brief Communications & Review Papers, 2005. **44**(10): p. 7296-7300.

72. Qin, Q., et al., *Electroluminescence of an n-ZnO/p-GaN heterojunction under forward and reverse biases.* Chinese Physics Letters, 2005. **22**(9): p. 2298-2301.

73. Xu, H.Y., et al., *Ultraviolet electroluminescence from p-GaN/i-ZnO/n-ZnO heterojunction light-emitting diodes.* Applied Physics B-Lasers and Optics, 2005. **80**(7): p. 871-874.

74. Ataev, B.M., et al., *Fabrication and properties of an n-ZnO : Ga/p-GaN : Mg/alpha-Al_2O_3 heterojunction.* Semiconductors, 2004. **38**(6): p. 672-674.

75. Ataev, B.M., et al., *n-ZnO/p-GaN/alpha-Al_2O_3 heterojunction as a promising blue light emitting system.* Journal of Optoelectronics and Advanced Materials, 2003. **5**(4): p. 899-902.

76. El-Shaer, A., et al., *Fabrication and characterization of n-ZnO on p-SiC heterojunction diodes on 4H-SiC substrates.* Superlattices and Microstructures, 2007. **42**(1-6): p. 387-391.

77. Kandasamy, S., et al., *Electrical characterization and hydrogen gas sensing properties of a n-ZnO/p-SiC Pt-gate metal semiconductor field effect transistor.* Applied Physics Letters, 2007. **90**(6): p. 064103-1-064103-3.

78. Alivov, Y.I., et al., *Electrical and optical properties of n-ZnO/p-SiC heterojunctions.* Japanese Journal of Applied Physics Part 1-Regular Papers Brief Communications & Review Papers, 2005. **44**(10): p. 7281-7284.

79. Alivov, Y.I., et al., *Photoresponse of n-ZnO/p-SiC heterojunction diodes grown by plasma-assisted molecular-beam epitaxy.* Applied Physics Letters, 2005. **86**(24): p. 241108-1-241108-3.

80. Yuen, C., et al., *Fabrication of n-ZnO : Al/p-SiC(4H) heterojunction light-emitting diodes by filtered cathodic vacuum arc technique.* Applied Physics Letters, 2005. **86**(24): p. 182112-1-182112-3.

81. Alivov, Y.I., et al., *Fabrication and characterization of n-ZnO/p-AlGaN heterojunction light-emitting diodes on 6H-SiC substrates.* Applied Physics

Letters, 2003. **83**(23): p. 4719-4721.

82. Jeong, I.S., J.H. Kim, and S. Im, *Ultraviolet-enhanced photodiode employing n-ZnO/p-Si structure.* Applied Physics Letters, 2003. **83**(14): p. 2946-2948.

83. Park, C.H., et al., *Spectral responsivity and quantum efficiency of n-ZnO/p-Si photodiode fully isolated by ion-beam treatment.* Applied Physics Letters, 2003. **82**(22): p. 3973-3975.

84. Tan, S.T., et al., *Ultraviolet and visible electroluminescence from n-ZnO/SiO_x/(n,p)-Si heterostructured light-emitting diodes.* Applied Physics Letters, 2008. **93**(1): p. 013506-1-013506-3.

85. Mridha, S. and D. Basak, *Ultraviolet and visible photoresponse properties of n-ZnO/p-Si heterojunction.* Journal of Applied Physics, 2007. **101**(8): p. 083102-1-083102-5.

86. Ajimsha, R.S., M.K. Jayaraj, and L.M. Kukreja, *Electrical characteristics of n-ZnO/p-Si heterojunction diodes grown by pulsed laser deposition at different oxygen pressures.* Journal of Electronic Materials, 2008. **37**(5): p. 770-775.

87. Choi, Y.S., et al., *Photoresponse characteristics of n-ZnO/p-Si heterojunction photodiodes.* Journal of Vacuum Science & Technology B, 2002. **20**(6): p. 2384-2387.

88. Jeong, I.S., et al., *n-ZnO/p-Si UV photodetectors employing AlO_x films for antireflection.* Thin Solid Films, 2004. **447**: p. 111-114.

89. S. J. Jiao, Y.M.L., D. Z. Shen, Z. Z. Zhang, B. H. Li, J. Y. Zhang, B. Yao, Y. C. Liu, and X. W. Fan, *Ultraviolet electroluminescence of ZnO based heterojunction light emitting diode.* phys. stat. sol. (c), 2006. **3**: p. 972-975.

90. Lin, T.K., et al., *ZnO MSM photodetectors with Ru contact electrodes.* Journal of Crystal Growth, 2005. **281**(2-4): p. 513-517.

91. Liu, C., et al., *Fabrication and characterization of ZnO film based UV photodetector.* Journal of Materials Science-Materials in Electronics, 2009. **20**(3): p. 197-201.

92. Yadav, H.K., K. Sreenivas, and V. Gupta, *Enhanced response from metal/ZnO bilayer ultraviolet photodetector.* Applied Physics Letters, 2007. **90**(17): p. 172113-1-172113-3.

93. Purica, M., E. Budianu, and E. Rusu, *ZnO thin films on semiconductor substrate for large area photodetector applications.* Thin Solid Films, 2001. **383**(1-2): p. 284-286.

94. Chen, S.F., et al., *Preparation, characterization and activity evaluation of p-n junction photocatalyst p-NiO/n-ZnO.* Journal of Sol-Gel Science and Technology, 2009. **50**(3): p. 387-396.

95. Deng, R., et al., *X-ray photoelectron spectroscopy measurement of n-ZnO/p-NiO heterostructure valence-band offset.* Applied Physics Letters, 2009. **94**(2): p. 022108-1-022108-3.

96. Ishida, Y., et al., *Potential profiling of the nanometer-scale charge-depletion layer in n-ZnO/p-NiO junction using photoemission spectroscopy.* Applied Physics Letters, 2006. **89**(15): p. 153502-1-153502-3.

97. Ohta, H., et al., *UV-detector based on pn-heterojunction diode composed of transparent oxide semiconductors, p-NiO/n-ZnO.* Thin Solid Films, 2003. **445**(2): p. 317-321.

98. Gu, Y.F., et al., *Visible-blind ultra-violet detector based on n-ZnO/p-Si heterojunction fabricated by plasma-assisted pulsed laser deposition.* Solid State Communications, 2007. **143**(8-9): p. 421-424.

99. Harako, S., et al., *Visible and infrared electroluminescence from an Er-doped*

n-ZnO/p-Si light emitting diode. Physica Status Solidi (a) Applications and Materials Science, 2008. **205**(1): p. 19-22.

100. Kim, H.Y., et al., *Photoresponse of Si detector based on n-ZnO/p-Si and n-ZnO/ n-Si structures.* Optical Materials, 2001. **17**(1-2): p. 141-144.

101. Park, C.H., et al., *n-ZnO/p-Si photodiodes fabricated using ion-beam induced isolation technique*. Nuclear Instruments & Methods in Physics Research Section B-Beam Interactions with Materials and Atoms, 2003. **206**: p. 432-435.

102. Park, C.H., et al., *n-ZnO/p-Si photodiodes fully isolated by B^+ ion-implantation.* Nuclear Instruments & Methods in Physics Research Section B-Beam Interactions with Materials and Atoms, 2004. **216**: p. 127-130.

103. Huang, Y.-F., et al., *Improved broadband and quasi-omnidirectional anti-reflection properties with biomimetic silicon nanostructures*. Nat Nano, 2007. **2**(12): p. 770-774.

104. Krunks, M., et al., *Nanostructured solar cell based on spray pyrolysis deposited ZnO nanorod array.* Solar Energy Materials and Solar Cells, 2008. **92**(9): p. 1016-1019.

105. Tanaka, M., et al., *Development of new a-Si C-Si heterojunction solar-cells - ACJ-HIT (Artificially Constructed Junction-Heterojunction with Intrinsic Thin-Layer).* Japanese Journal of Applied Physics Part 1-Regular Papers Short Notes & Review Papers, 1992. **31**(11): p. 3518-3522.

106. Lalatonne, Y., J. Richardi, and M.P. Pileni, *Van der Waals versus dipolar forces controlling mesoscopic organizations of magnetic nanocrystals*. Nature Materials, 2004. **3**(2): p. 121-125.

107. Huang, Y.F., et al., *Improved broadband and quasi-omnidirectional anti-reflection properties with biomimetic silicon nanostructures*. Nature

Nanotechnology, 2007. **2**(12): p. 770-774.

108. Yang, Z.P., et al., *Experimental observation of an extremely dark material made by a low-density nanotube array.* Nano Letters, 2008. **8**(2): p. 446-451.

109. Alivov, Y.I., et al., *Observation of 430 nm electroluminescence from ZnO/GaN heterojunction light-emitting diodes.* Applied Physics Letters, 2003. **83**(14): p. 2943-2945.

110. Xu, P.S., et al., *Native point defect states in ZnO.* Chinese Physics Letters, 2001. **18**(9): p. 1252-1253.

111. Studenikin, S.A., N. Golego, and M. Cocivera, *Fabrication of green and orange photoluminescent, undoped ZnO films using spray pyrolysis.* Journal of Applied Physics, 1998. **84**(4): p. 2287-2294.

112. Khan, M.A., et al., *Violet-blue GaN homojunction light-emitting-diodes with rapid thermal annealed p-type layers.* Applied Physics Letters, 1995. **66**(16): p. 2046-2047.

113. Ohta, H., et al., *Fabrication and photoresponse of a pn-heterojunction diode composed of transparent oxide semiconductors, p-NiO and n-ZnO.* Applied Physics Letters, 2003. **83**(5): p. 1029-1031.

114. Liang, S., et al., *ZnO Schottky ultraviolet photodetectors.* Journal of Crystal Growth, 2001. **225**(2-4): p. 110-113.

Related Publications and Honor

2010/2/5

A. International Journal Paper

- **Cheng-Pin Chen**, Pei-Hsuan Lin, Yen-Jen Hung, Shao-Sun Hsu, Liang-Yi Chen, Yun-Wei Cheng, Min-Yung Ke, Ying-Yuan Huang, Chun-Hsiang Chang, Ching-Hua Chiu, Hao-Chung Kuo, JianJang Huang, " Investigation of Light Absorption Properties and Accpetance Angles of Nanopatterned GZO/a-Si/p^+-Si Photodiodes ", Submitted to Nanotechnology (Jan. 2010)

- **Cheng-Pin Chen**, Pei-Hsuan Lin, Liang-Yi Chen, Min-Yung Ke, Yun-Wei Cheng and JianJang Huang "N-ZnO/p-Si Photodiodes with Improved Photoresponsivities and Acceptance Angles for Solar Applications", ECS Transactions Vienna, Austria" Vol. 25," Photovoltaics forthe 21st Century 5", from the Vienna, Austria meeting. (2010)

- Min-Yung Ke, Tzu-Chun Lu, Sheng-Chieh Yang, **Cheng-Pin Chen**, Yun-Wei Cheng, Liang-Yi Chen, Cheng-Ying Chen, Jr-Hau He, and JianJang Huang, "UV light emission from GZO/ZnO/GaN heterojunction diodes with carrier confinement layers," Optics Express Vol. 17, Iss. 25, pp. 22912–22917 (2009)

- Min-Yung Ke, Cheng-Yin Wang, Liang-Yi Chen, Hung-Hsien Chen, Hung-Li Chiang, Yun-Wei Cheng, Min-Yann Hsieh, **Cheng-Pin Chen** and JianJang Huang, "Fabrication and Characterizations of Nanorod Light Emitting Diode Arrays Using Nanosphere Lithography", ECS Transactions, 25 (10), pp. 73-78 (2009)

- Y. W. Cheng, K. M. Pan, L. Y. Chen, M. Y. Ke, **C. P. Chen** and J. J. Huang, "Characterizations of Sidewall Reflected GaN-Based LEDs Using self-Aligned Nanorod Arrays as Localized Photonic Crystals," ECS Transactions, 25 (12), pp. 41-47 (2009)

- Kun-Mao Pan, Yun-Wei Cheng, Liang-Yi Chen, Ying-Yuan Huang, Min-Yung Ke, **Cheng-Pin Chen**, Yuh-Renn Wu and JianJang Huang, "Polarization dependent sidewall light diffraction of LEDs surrounded by nanorod arrays," IEEE, Photonics Technology Letters, vol. 21, pp. 1683-1685 (2009)

- Yun-Wei Cheng, Kun-Mao Pan, Liang-Yi Chen, Min-Yung Ke, **Cheng-Pin Chen**, Cheng-Yen Chen, C. C. Yang and JianJang Huang, "Characterizations of GaN -Based LEDs Encompassed with Self-Aligned Nanorod Arrays of Various Distribution Densities," IEEE Electron Device Letters, 30 (10), pp. 1060-1602 (2009)

- **Cheng-Pin Chen**, Pei-Hsuan Lin, Liang-Yi Chen, Min-Yung Ke, Yun-Wei Cheng and JianJang Huang, "Nanoparticle coated n-ZnO/p-Si photodiodes with improved photoresponsivities and acceptance angles for potential solar cell applications," Nanotechnology, 20, 245204 (2009).

- Min-Yung Ke, Cheng-Yin Wang, Liang-Yi Chen, Hung-Hsien Chen, Hung-Li Chiang, Yun-Wei Cheng, Min-Yann Hsieh, **Cheng-Pin Chen** and JianJang Huang "Application of Nanosphere Lithography to LED surface texturing and to the fabrication of nanorod LED Arrays," IEEE Journal of Selected Topics in Quantum

Electronics, vol. 15 (4), pp. 1242-1249 (2009)

- Yun-Wei Cheng, Kun-Mao Pan, Cheng-Yin Wang, Hung-Hsien Chen, Min-Yung Ke, **Cheng-Pin Chen**, Min-Yann Hsieh, Han-Ming Wu, Lung-Han Peng and JianJang Huang, "Enhanced light collection of GaN light emitting devices by redirecting the lateral emission using nanorod reflectors," Nanotechnology, vol. 20, pp. 035202, 2009 (SCI, EI)

- Yun-Wei Cheng, Hung-Hsien Chen, Min-Yung Ke, **Cheng-Pin Chen** and Jian Jang Huang "Effect of Selective Ion-Implanted P-GaN on the Junction Temperature of GaN-Based Light Emitting Diodes," Optics communications, vol 282 (5), pp. 835-838 (2009) (SCI,EI)

- Yun-Wei Cheng, Hung-Hsien Chen, Min-Yung Ke, **Cheng-Pin Chen**, JianJang Huang, "On-chip very low junction temperature GaN-based light emitting diodes by selectively ion implantation," The Eighth International Conference on Solid State Lighting, Optics and Photonics (SPIE), Proc. of SPIE, vol 7058, pp. 705805-1~9, 2008 (EI).

- Cheng-Yin Wang, Liang-Yi Chen, **Cheng-Pin Chen**, Yun-Wei Cheng, Min-Yung Ke, Min-Yann Hsieh, Han-Ming Wu, Lung-Han Peng, and JianJang Huang, "GaN nanorod light emitting diode arrays with a nearly constant electroluminescent peak wavelength," Optics Express, vol. 16 (14), pp. 10549-10556, 2008. (SCI, EI)

- Liang-Yi Chen, Cheng-Yin Wang, **Cheng-Pin Chen**, Yun-Wei Cheng, Min-Yung Ke, and JianJang Huang, "Strain Relaxed GaN/InGaN Nanorod Light Emitting

Arrays," ECS Transactions, vol. 16 (7), pp. 145-148, 2008. (EI)

- Min-Yann Hsieh, Cheng-Yin Wang, Liang-Yi Chen, Tzu-Pu Lin, Min-Yung Ke, Yun-Wei Cheng, Yi-Cheng Yu, **Cheng Pin Chen**, Dong-Ming Yeh, Chih-Feng Lu, Chi-Feng Huang, C. C. Yang, and JianJang Huang, "Improvement of External Extraction Efficiency in GaN-Based LEDs by SiO2 Nanosphere Lithography," IEEE, Electron Device Letters. Vol. 29, pp. 658-660, 2008 (SCI, EI)

- **Cheng Pin Chen**, Min Yung Ke , Chien Cheng Liu , Yuan Jen Chang , Fu Hsiang Yang, and JianJang Huang, "Observation of 394 nm Electroluminescence from Low-Temperature Sputtered n-ZnO/SiO2 Thin Films on top of the p-GaN Heterostructure," Applied Physics Letters 91, pp. 091107 (2007)

B. International Conference Paper

- **Cheng-Pin Chen**, Pei-Hsuan Lin, Yen-Jen Hung, Shao-Shun Hsu, Liang-Yi Chen , Min-Yung Ke, Yun-Wei Cheng and JianJang Huang, "Investigation of a n-ZnO/a-Si/p+-Si Solar Cell with a Nanopatterned Intrinsic a-Si Layer," White LEDs, Taiwan, Dec. 2009.

- **Cheng-Pin Chen**, Pei-Hsuan Lin, Liang-Yi Chen, Min-Yung Ke, Yun-Wei Cheng and JianJang Huang, "n-ZnO/p-Si Photodiodes with Improved Photoresponsivities and Acceptance Angles for Solar Applications," 216th Electrochemical Society (ECS) Meeting, Vienna, Austria, Oct, 2009.

- Y. W. Cheng, K. M. Pan, L. Y. Chen, M. Y. Ke, **C. P. Chen** and J. J. Huang,

"Characterizations of sidewall reflected GaN-based LEDs using self-aligned nanorod arrays as localized photonic crystals," 216th Electrochemical Society (ECS) Meeting, Vienna, Austria, Oct, 2009

- M. Y. Ke, C. Y. Wang, L. Y. Chen, H. H. Chen, H. L. Chiang, Y. W. Chen, M. Y. Hsieh, **C. P. Chen** and J. J. Huang, "Fabrication and Characteristics of Nano-array Light Emitting Diodes by Using Nanosphere Lithography," 216th Electrochemical Society (ECS) Meeting, Vienna, Austria, Oct, 2009

- Yun-Wei Cheng, Kun-Mao Pan, Liang-Yi Chen, **Cheng-Pin Chen**, Min-Yung Ke and JianJang Huang, "Redirection of Lateral Emission Using Nanorod Reflectors for Power Enhancement of GaN Light Emitting Diodes," The Conference on Lasers and Electro-Optics (CLEO), Baltimore, USA, May, 2009.

- M. Y. Ke, H. L. Chiang, Y. W. Cheng, K. M. Pan, L. Y. Chen, **C. P. Chen**, C. Y. Chen, C. C. Yang and J. J. Huang, "Improvement of LED light output efficiency in the surface vertical direction using localized photonic crystal nanorod array," Asia-Pacific Workshop on Widegap Semiconductors (APWS), May, 2009.

- Yun-Wei Cheng, Hung-Hsien Chen, Min-Yung Ke, **Cheng-Pin Chen**, JianJang Huang, "Low Junction Temperature GaN-based Light Emitting Diodes by Selectively Ion-implanted Cold Zon," International light sources workshop, Taiwan, Jan, 2009.

- Kun-Mao Pan, Yun-Wei Cheng, Liang-Yi Chen, Cheng-Yin Wang, Min-Yung Ke, **Cheng-Pin Chen**, Min-Yann Hsieh, and JianJang Huang "Using Nanorod Sidewall

Reflectors to Improve Light Extraction of GaN-based Light Emitting Devices," International Light Sources Workshop, Taiwan, Jan, 2009

- Liang-Yi Chen, Cheng-Yin Wang, **Cheng-Pin Chen**, Yun-Wei Cheng, Min-Yung Ke, and JianJang Huang, "Quantum Confine Stark Effect Suppressed Nanorod Structure Light Emitting Diode," IEEE Photonics Global at Singapore Dec, 8-11,2008

- **Cheng-Pin Chen**, Pei-Hsuan Lin, Min-Yung Ke, Hung-Li Chiang, Kuang-Chung Liu, Yun-Wei Cheng, JianJang Huang, "Enhancement of Acceptance Angle of incident Light by SiO_2 Nanoparticles on n-ZnO/p-Si Heterojunction Photodetector," International Symposium on Solar Cell Technologies (ISSCT), NCTU, Dec, (2008)

- Liang-Yi Chen, Cheng-Yin Wang, **Cheng-Pin Chen**, Yun-Wei Cheng, Min-Yung Ke, Min-Yann Hsieh, Han-Ming Wu, Lung-Han Peng and JianJang Huang, "GaN Based Nanorod Light Emitting Arrays with a Nearly Constant Electroluminescence Peak Wavelength," International work shop on Nitride semiconductors Oct, , 2008, Motreux, Switzerland

- Liang-Yi Chen, Cheng-Yin Wang, **Cheng-Pin Chen**, Yun-Wei Cheng, Min-Yung Ke, and JianJang Huang, "Strain Relaxed GaN/InGaN Nanorod Light Emitting Arrays," Honolulu, HI, Oct, 2008, 214th ECS Meeting.

- Yun-Wei Cheng, Hung-Hsien Chen, Min-Yung Ke, **Cheng-Pin Chen**, JianJang Huang, “On-chip very low junction temperature GaN-based light emitting diodes by selectively ion implantation,” The Eighth International Conference on Solid State Lighting, Optics and Photonics (SPIE), San Diego, US, Aug, 10-14, 2008.

- Min-Yung Ke, **Cheng-Pin Chen**, Yun-Wei Cheng, Yuan-Jen Chang, and JianJang Huang “Blue and Orange Light Illumination by Integrating a GaN Based LED with a SiO2 Layer,” International Nano-Optoelectronic Workshop, Beijing, China, 2007

- **Cheng Pin Chen**, Min Yung Ke , Chien Cheng Liu , Yuan Jen Chang , Fu Hsiang Yang, and JianJang Huang, "Observation of 394 nm Electroluminescence from Low-Temperature Sputtered n-ZnO/SiO_2 Thin Films on top of the p-GaN Heterostructure," White LEDs, Tokyo, Dec. 2007.

C. Honor

- **Cheng-Pin Chen**, Pei-Hsuan Lin, Yen-Jen Hung, Shao-Shun Hsu, Jian-Jang Huang, “The Potential of Solar Cell by Nanostructure Junction of n-ZnO/a-Si/p^+-Si Heterojunction Photodiode with Silica Nanosphere Technique,” **Student Paper Award**,Optics & Photonics Taiwan (OPT), Taiwan, Dec. 2009.